



Università degli Studi di Cagliari

Ph.D. Degree
Electronic and Computer Engineering
Cycle XXXIV

Modelling and Application of Battery Energy Storage
Systems in Electric Vehicle Charge

ING-IND/32

Ph.D. Student:

Daniele Battaglia

Supervisor:

Prof. Alfonso Damiano

Final Exam. Academic Year 2020-2021
Thesis defence: April 2022 Session

*Alla mia famiglia,
per tutto il vostro sostegno e per tutto il vostro amore.*

*Ai miei amici,
per la vostra presenza durante tutto questo percorso.*

*A Giorgia,
hai creduto in me e non mi hai mai fatto perdere la speranza.*

Abstract

The present PhD dissertation deals with the dynamic modelling and implementation of a molten salt battery storage system of the SMHB (Sodium Metal Halide) topology. Chapter 1 focuses on the state of the art of Battery Energy Storage System (BESS) technologies, highlighting the most widespread technologies and their relative advantages and disadvantages. In addition, different modelling techniques are presented for the description of the storage system behaviour. Next, the main fields of application for BESS are presented. Chapter 2 introduces the Sodium Metal Halide Battery. Its chemical characteristics have been deeply investigated. In particular, an equivalent circuit model of Thevenin is presented for the description of the dynamic behaviour of the battery. A comparison between two different models of iron (present in SMHB) has been investigated, showing the improvements through experimental tests. Chapter 3 concerns the development of a Dual Active Bridge (DAB) DC/DC converter to be interfaced with the SMHB battery. The converter has been developed in two configurations: the standard and the partial. The two configurations have been compared considering the efficiency of the battery-converter system. A round trip efficiency analysis has been performed, the results of which show higher efficiencies for the partial configuration. In Chapter 4, the main applications of second-life batteries (SLBs) are presented. In particular, the DCFC application has been analysed and compared with other power profiles. The application of Li-ion SLB battery packs has been considered for the DCFC application, developing different power profiles and studying the impact of degradation and replacement rate for a specific system design. Correlations between the characteristics of SLBs and the replacement rate are presented. Finally, a comparison between the lithium-ion SLB technologies and the SMHB for the application of DCFC is presented. The aging effects of SMHB highlight how this technology is a good candidate for the application of DCFC in support of SLBs.

Daniele Battaglia gratefully acknowledges Eni Corporate University S.p.A for the financial support of his PhD scholarship.



Contents

Introduction	1
1 Battery Energy Storage Systems	3
1.1 Different types of Battery Energy Storage Systems	6
1.1.1 Lead-Acid Battery	6
1.1.2 Nickel-Cadmium Battery	7
1.1.3 Lithium-ion Battery	8
1.1.4 Sodium-Sulphur and Sodium-Nickel-Chloride Batteries	9
1.1.5 Flow Batteries	9
1.2 Battery Models	11
1.2.1 Electrochemical Models	11
1.2.2 Mathematical Models	12
1.2.3 Electrical Models	13
1.3 Applications of Battery Energy Storage Systems	15
1.3.1 Time-Shift	15
1.3.2 Regulation and Reserves	16
1.3.3 Frequency Response	16
1.3.4 Power Quality and Power Reliability	17
1.3.5 Load Levelling and Peak Shaving	17
1.3.6 Electric Vehicles and Charging Stations	17
2 The Sodium Metal Halide Battery	19
2.1 SMHB's characteristics	20
2.2 Model of the SMHB	23
2.2.1 Parameter identification	28
2.2.2 Experimental result	31
2.3 Improved model	35
2.3.1 Experimental results of the improved model	42
3 SMHB and DAB-DC/DC Converter Coupling	46
3.1 Dual Active Bridge Converter	47
3.2 DAB Configuration	49
3.3 Simulation and results	53
4 Second Life Batteries	60
4.1 Power Profiles for Second Life Batteries	61

4.1.1	Definition of the Metrics	63
4.2	Battery and Aging Model for Lithium-ion	66
4.3	Application and aging correlation	71
4.4	SMHB comparison	77
	Conclusion	83

Introduction

Environmental and energy policies are driving a transformation of the electricity system by accelerating the transition to low-carbon technologies. This has led to a rapid spread of distributed generation (DG) based on renewable energy sources (RES), which are contributing to significantly changing the structure of the electricity grid from centralized to distributed form. However, the issues related to power fluctuations of RES generation as well as load variations on the distribution system, require more flexibility and intelligence in the energy management, making the Electrochemical Energy Storage Systems (E-ESS) a key component for the implementation of smart-based energy models. In fact, E-ESS due to their versatility, power scalability, efficiency, and dynamic characteristics, are able to support the power supply system in providing power, current, and voltage compensations in the presence of unexpected fluctuations. There are currently several consolidated electrochemical technologies to provide storage services in the energy and mobility sectors, such as lead-acid, lithium-ion, vanadium redox, and sodium-sulphur systems. However, their use in stationary energy storage applications is limited due to several factors. For example, lead-acid batteries suffer from a limited life cycle, lead toxicity, and low energy density, while the high energy cost and thermal management, and safety issues are the challenges associated with lithium-based technologies. Also, sodium-sulphur batteries still face several obstacles due to safety concerns and the risk of accidents. Therefore, alternative battery technologies could be considered in order to provide successful storage requirements such as high energy density, low cost, high safety, longer cycle life, and environmental compatibility. Moreover, the expected growth in demand for E-ESS requires attention to be paid to the availability of materials required for their production. As for automotive applications, E-ESSs play a key role for electric vehicles (EVs), especially in making them more competitive than ICE-based vehicles. In particular, lithium-ion batteries seem to be the best technology due to their high specific energy and specific power compared to other battery technologies. However, if on the one hand, the implementation of electric vehicles favours a reduction of CO₂ emissions, on the other hand, there is an increase in the instability of the electricity grid with the increasing increase in uncontrolled charging events. A solution in this context can be the spread of fast charging stations as support for the grid. Reducing the investment cost for charging stations can be provided by the adoption of second-life batteries (SLBs). In fact, lithium-ion batteries that have lost only

20% of their initial capacity are often withdrawn from the EV application and sent to battery recycling facilities. However, these batteries are still able to provide services for stationary applications, such as DCFC. By combining the use of new innovative batteries and second-life batteries, it is possible to create an effective solution to the growth of vehicle electric charging stations.

In this context, the present PhD dissertation deals with the dynamic modelling and implementation of a molten salt battery storage system of the SMHB (Sodium Metal Halide) topology. Chapter 1 focuses on the state of the art of Battery Energy Storage System (BESS) technologies, highlighting the most widespread technologies and their relative advantages and disadvantages. In addition, different modelling techniques are presented for the description of the storage system behaviour. Next, the main fields of application for BESS are presented. Chapter 2 introduces the Sodium Metal Halide Battery. Its chemical characteristics have been deeply investigated. In particular, an equivalent circuit model of Thevenin is presented for the description of the dynamic behaviour of the battery. A comparison between two different models of iron (present in SMHB) has been investigated, showing the improvements through experimental tests. Chapter 3 concerns the development of a Dual Active Bridge (DAB) DC/DC converter to be interfaced with the SMHB battery. The converter has been developed in two configurations: the standard and the partial. The two configurations have been compared considering the efficiency of the battery-converter system. A round trip efficiency analysis has been performed, the results of which show higher efficiencies for the partial configuration. In Chapter 4, the main applications of second-life batteries (SLBs) are presented. In particular, the DCFC application has been analysed and compared with other power profiles. The application of Li-ion SLB battery packs has been considered for the DCFC application, developing different power profiles and studying the impact of degradation and replacement rate for a specific system design. Correlations between the characteristics of SLBs and the replacement rate are presented. Finally, a comparison between the lithium-ion SLB technologies and the SMHB for the application of DCFC is presented. The aging effects of SMHB highlight how this technology is a good candidate for the application of DCFC in support of SLBs.

Chapter 1

Battery Energy Storage Systems

Energy Storage System (ESS) is used to indicate a system capable of storing and converting electrical energy into another form of energy, such as chemical, mechanical, electrostatic, or electromagnetic energy. The storage system can be assimilated to a load that absorbs electricity and transforms it into another form of energy, from which it can be drawn later, by carrying out the opposite conversion. Such types of ESSs are experiencing growing interest from both academic and industrial research, mainly due to technological improvements and recent environmental problems. In particular, the continuous change in strategic sectors, such as distributed power generation and electrified transport, is significantly based on the development of high-performance ESSs, which should also be characterized by moderate costs and long life expectancy. Although further improvements are needed to achieve these goals, ESSs are already being used successfully in several fields, as well documented in the technical literature [1–6].

Each energy storage system is composed of three primary components [7]: storage medium; power conversion system (PCS); balance of plant (BOP). The storage medium is the "energy reservoir" that stores potential energy within an accumulation system. The PCS is the system capable of converting from alternating current (AC) to direct current (DC), working as a rectifier in the charging phase and as an inverter in the discharging phase. The PCS also conditions the power during conversion to ensure that no damage is done to the storage system. The BOP typically includes electrical interconnections, surge protection devices, and other control systems.

Nowadays the energy storage typologies are several and differ from each other both from the structural point of view and of use. In the first case, considering the energy conversion mode, it is possible to distinguish mechanical, electrochemical, electrostatic or electromagnetic accumulation systems. In the second case, it is possible to diversify ESSs with high energy density or high power density. High energy density systems are capable of delivering amounts of energy for long periods of time. While high power density storage systems are capable of delivering a large amount of energy, but in short periods of time. From this latter classification, it is clear how the storage systems can intervene

within the global electrical system for various types of applications [8].

Electrochemical storage systems are the most traditional technology for storing electricity. This energy is converted into electrochemical energy through chemical reactions. Commonly called batteries, or battery energy storage systems (BESSs), are divided into two types: primary batteries and secondary batteries. The primary batteries, after their use, can no longer be recharged or returned to their initial state of charge (SoC). The secondary batteries use an external DC voltage generator to be recharged, and returned to their initial SoC.

The operating principle of the battery is based on the electrochemical oxidation-reduction (redox) reaction [9]. This type of reaction involves the transfer of electrons from one material to another through an electrical circuit. The basic electrochemical unit is known as a "cell". A battery consists of one or more cells, connected in series, in parallel, or both, depending on the desired voltage and output capacity. A cell consists of an electrolyte, which contains dissolved ions, and two electrodes containing different active materials. When the cell discharges, the electrochemical reaction which occurs is the following: the negative electrode (anode) gives electrons to the external circuit and oxidizes during the reaction. The positive electrode (cathode) accepts electrons from the external circuit and is reduced during the reaction. When the cell is charged, the reaction is reversed and the electrons flow in the opposite direction (Fig. 1). The electrolyte, placed between the two electrodes, is the medium for the transfer of ions. It typically consists of a liquid, such as water with dissolved salts, acids or alkalis to impart ionic conductivity. Some batteries use solid electrolytes, which are ionic conductors at the operating temperature of the cell.

When the cell is connected to an external load, electrons flow from the anode, which is oxidized, through the external load to the cathode, which is reduced, where the electrons are accepted. The electrons' flow that is established generates a continuous current, due to the potential difference by the electrodes. By suitably intercepting this flow through an electrical circuit and an energy conversion device, it is possible to exchange electricity with the battery in both directions. At the same time, an exchange of ions takes place between the two electrodes, ensuring the balance of the charges. At the end of the process, the potential difference that is established between the electrodes is cancelled due to the state of chemical equilibrium that is reached inside the cell, putting an end to the flow of electrons and ions.

According to the application in which they are used, the batteries can be differentiated according to some specific parameters. In the following are described some of these parameters that allow you to characterize each battery.

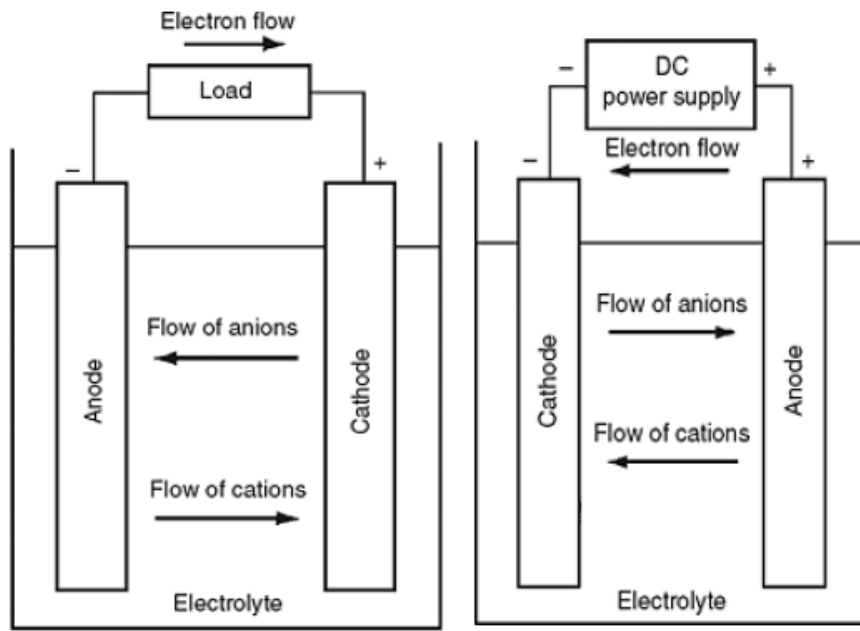


Figure 1: Electrochemical operation's cell. Discharging on the left and charging on the right.

- **Cell Voltage.** It is the voltage that is measured across the two electrodes. It can be distinguished in:
 - Open Circuit Voltage (OCV): the voltage across the electrodes in absence of electrical load;
 - Nominal Voltage: the operating voltage of the cell;
 - Cut-Off Voltage: the minimum end-of-charge voltage, which causes the discharge process to be interrupted.
- **Storage Capacity.** It is the amount of stored electrical charge that can be extracted from the battery during discharge, up to the cut-off voltage value. It is expressed in ampere/hour [Ah] or in watt/hour [Wh]. A nominal capacity value is commonly indicated by the manufacturer, depending on the temperature and discharge current.
- **State of Charge (SoC).** It defines the capacity that can still be supplied by the battery at a defined instant, in relation to the nominal capacity value. It is expressed as a percentage. SoC of zero means the battery is low. The complementary term is the depth of discharge (DoD), which can be expressed as:

$$\text{DoD} = 1 - \text{SoC}$$

- **C-rate.** It indicates how fast the battery discharges or charges, by the current value with which the discharge or charge occurs. For example, a

battery with a nominal capacity of 10Ah, with a C-rate of 1C is equivalent to a discharge or charge current of 10A.

- **Nominal Energy.** Expressed in watt/hour [Wh], it indicates the energy that the battery delivers during operation, starting from a fully charged condition up to complete discharge. It is obtained from the product of the nominal capacity of the battery with the nominal voltage. Can be expressed as specific energy [Wh/kg] or energy density [Wh/m³].
- **Lifetime.** It represents the number of charge-discharge cycles that the battery can sustain. Generally, a battery can be considered exhausted if it cannot sustain a charge exceeding 80% of its capacity. It is an important parameter for determining the cost of the battery. The lifetime of a battery strongly depends on the way it works and is drastically reduced if it is subjected to incorrect management.
- **Self-discharge.** It is a parameter that describes the discharge rate of a battery in open circuit conditions. It is caused by unwanted chemical reactions. It also strongly depends on the outside temperature.
- **Efficiency.** For a battery, the amperometric efficiency and the energy efficiency are identified. The first indicates the ratio between the charge extracted during discharging and that restored during charging. The second indicates the ratio between the released energy and that spent to restore the initial state of charge.
- **Temperature.** The performance of a cell can also vary considerably according to the working temperature. In fact, at low temperatures, in batteries with liquid electrolytes, for example, the electrolyte could freeze; at high temperatures, on the other hand, there could be a change in the kinetics in the redox reaction inside the battery which could discharge prematurely or even accelerate its deterioration.

1.1 Different types of Battery Energy Storage Systems

Based on the use of different chemicals to produce electrical energy, different kinds of batteries have been developed. Today, there is a wide range of battery technologies in the market where each one has its advantages and disadvantages. Among the various battery technologies, some of them seem to be more suitable for power system applications due to technical benefits, which are discussed in the following.

1.1.1 Lead-Acid Battery

Lead-acid batteries are the most established and widespread technology in today's reality [10]. Developed in 1859 by the Frenchman Raymond Gaston

Plantè, it has been continuously evolved up to the present day and is currently used in numerous applications, such as: stationary energy storage, lighting systems for electric and hybrid vehicles, starting the engine of the latter. Due to their inherent heaviness, lead-acid batteries have been employed in applications where size and weight are not an issue. Their strong diffusion is mainly due to the low cost of materials, in particular of lead due to its high availability, and to the fact that it is a very well-established and relatively simple technology. It falls into the category of secondary batteries, and has the advantage of being recyclable. The cell is made up of an electrolyte of diluted sulfuric acid, in which the two electrodes are immersed. The positive electrode is made of lead dioxide, while the negative electrode is made of metal lead. During discharge, the electrolyte is consumed, therefore its concentration linearly decreases with the SoC. The main disadvantages of the lead-acid battery are the need for periodic maintenance of the water and its low energy and specific power. Lead-acid batteries also create difficulties in providing frequent power cycles, often in a partial state of charge leading to early failure due to sulfation [11]. In the last years, Valve Regulated Lead Acid (VRLA) batteries have been developed using new materials, such as copper, fibers and carbon compounds. Compared to conventional lead-acid batteries, VRLAs are characterized by longer life (about 10 times more) and reduced weight (about 1.5 times less) [12].

1.1.2 Nickel-Cadmium Battery

Along with lead-acid batteries, a nickel-cadmium battery (Ni-Cd) is also ranked in terms of maturity and popularity. The development of nickel-cadmium batteries was initially slow because of the limited availability of the material and its high cost. The first closed nickel batteries were made in 1947, after which they started to become more popular. Nickel-cadmium batteries consist of a positive electrode of nickel oxide, a negative electrode of cadmium hydroxide, a separator, and an alkaline electrolyte. Usually, nickel-cadmium batteries have a metal container with a sealing plate with a self-sealing safety valve. The electrodes, isolated from the separator, are coiled in a spiral inside the container. Nickel-cadmium batteries have a high energy density and can provide robust reliability with very low maintenance requirements. These mentioned advantages make them preferred over lead-acid batteries for power tools, portable devices, emergency lighting, UPS, telecommunications, and generator starting. However, portable devices such as cell phones and laptops have actually been supplanted from these markets by other chemicals, such as lithium, over the past decade. A major drawback of these batteries is their relatively high cost due to the expensive manufacturing process. Another drawback is that cadmium is a toxic heavy metal and therefore creates problems associated with the disposal of these batteries. Nickel-cadmium batteries also suffer from the "memory effect", in which the batteries are only fully charged after a series of complete discharges. These drawbacks have discouraged Ni-Cd improvements,

thus they have been replaced by Nickel-Metal-Hydrate batteries (NiMHs). Their structure is quite similar to Ni-Cds, particularly cadmium is replaced by a metal “M”, which consists of a mixture of rare earth elements and of nickel, aluminium, cobalt, or manganese. Consequently, NiMHs have been the most common power source for the first generation of portable electronic devices. However, this technology is not suitable for high charging rates, because it may reduce battery capacity. For these reasons, NiMHs have now been almost totally replaced by Lithium-ion batteries in the majority of applications.

1.1.3 Lithium-ion Battery

Lithium is the lightest metal with the highest potential due to its very reactive behaviour which, in theory, makes it very fitting as a compound for batteries. The first lithium-ion battery is proposed in the 1960s and then, the first commercial lithium-ion batteries came into the market by Sony in 1990. Later in 2000, lithium-ion batteries have become the most important storage technology in the areas of portable and mobile applications like laptops, cell phones, electric bicycles, and electric cars, thanks to their excellent performance in terms of energy and specific power, high energy efficiency, low self-discharging rates, and a long lifetime. Commonly they are small in size with capacities from mAh up to a few tens of Ah. The main disadvantages concern: strong thermal degradation due to high temperatures; high reactivity with water, which produces hydrogen and lithium hydroxide with the risk of explosion; high battery cost [13]. Lithium batteries differ from each other based on the materials that are used in making the electrodes and electrolytes. The common element is lithium-ion, which allows the passage of charge. Generally, lithium batteries are divided into two categories: lithium metal or lithium-ion. Lithium metal batteries consist of a lithium metal anode with solid or liquid electrolyte. They have a high capacity, low internal resistance, and high specific power and energy. Their disadvantage is that they are potentially dangerous due to the high reactivity of the lithium metal ion. Lithium-ion batteries, also called polymeric, are made up of intercalation electrodes, that is, they allow the release of amounts of lithium in a reversible manner, while the electrolyte is liquid. They have lower performance than lithium metal batteries, but greater safety is given the poor reactivity of the anode. The peculiarity of the latter is the absence of metal lithium which significantly reduces the cost. They have lower performance than lithium metal batteries, but greater safety is given the poor reactivity of the anode. The peculiarity of the latter is the absence of metal lithium which significantly reduces the cost. Another difference between the various types of lithium batteries is the material from which the cathode is made. In fact, in addition to the type of electrolyte used, lithium batteries can have a different cathode material, generally made up of a metal oxide, while the anode is mainly made up of graphite. Among the different materials

for the cathode, the most used are: NCA (Nickel, Cobalt, Aluminium), LFP (Lithium, Iron, Phosphorus), LCO (Lithium, Cobalt, Oxygen).

1.1.4 Sodium-Sulphur and Sodium-Nickel-Chloride Batteries

The main feature in these types of batteries is the operating temperature, which is around 300°C. The high temperature allows the electrodes to be kept in the molten state during operation, ensuring greater ionic conductivity of the solid electrolyte. Generally, the cell structure of sodium-sulphur battery (NaS) is of the tubular type, in which sodium constitutes the negative electrode and is located in the inner part. The positive electrode is made up of sulphur, and it is placed the outermost part of the cell. The electrolyte is solid and consists of β -alumina. It also acts as a physical separator, avoiding the mixing of the two electrodes. Another important feature of the electrolyte is the ability to conduct no electrons, thus preventing the battery from self-discharging. Due to their high temperature, the NaSs are equipped with auxiliary devices that allow temperature control at the operating levels. NaSs are characterized by high overall efficiency, long life cycle, lifetime, and are used for high power applications such as electricity generation, distribution, and transmission systems, therefore, for mainly stationary applications. Sodium-Nickel-Chloride batteries (or SMHB) have the same operating principle as NaSs, but in this case, the sulphur is replaced by nickel-chloride. These batteries are better known as ZEBRA, named after the research project during which they were invented in 1985 (ZEolite Battery Research Africa Project). In the next chapter, they will be described in more detail.

1.1.5 Flow Batteries

Flow batteries are particular storage systems developed in recent decades. Energy is stored within the electrolyte solution. The principle of operation is similar to fuel cells: two different electrolytes are stored in two external tanks and pumped into a cell containing a membrane, which allows the electrolytes to separate from each other. The circulation of ions through the electrolyte generated the electric current. The power of the cell is a function of the reactor dimension and the flow rate, the energy capacity instead is related to the size of electrolytes tanks. An advantage of this technology is that the two electrolytes are separated when the battery is completely discharged; in addition, charging/discharging processes do not affect electrolytes, leading to a long life expectancy. Thanks to this structure FBs are easily adaptable to different applications and negligible self-discharge. Moreover, instead of inverting the reaction, they offer the possibility to fast recharge by simply substituting electrolytes empty tanks with full ones. Last but not least materials used for FBs are not toxic. Several technologies have been proposed for FBs, among which are Vanadium Redox Battery (VRB) and Iron-Chromium (FeCr).

BESS	Energy Efficiency (%)	Energy Density (Wh/kg)	Power Density (W/kg)	Life Cycle	Self-Discharge
Lead-Acid	70-90	30-50	75-300	2000-4500	low
Ni-Cd	60-70	15-300	50-1000	2000-2500	low
Ni-MH	50-80	60-80	220	<3000	high
Li-ion	85-95	150-300	50-2000	1500-4500	medium
Li-polymer	85	200	250-1000	>1200	medium
NaS	75-90	150-250	150-230	2500-4500	medium
VRB	65-85	10-35	166	10000-13000	negligible
SMHB	85-90	100-140	150-200	2500-3000	-

Table 1: Battery Energy Storage System Typology.

At the present time, the different types of storage have features that make them suitable for different applications, either used individually or combined. Table 1 summarizes the main characteristics of the most common types of ESS [2, 14]. By evaluating the specific characteristics of the batteries, it is possible to represent the various types through the Ragone diagram, as shown in Fig. 2. This diagram is useful for evaluating which battery is most convenient for a particular application.

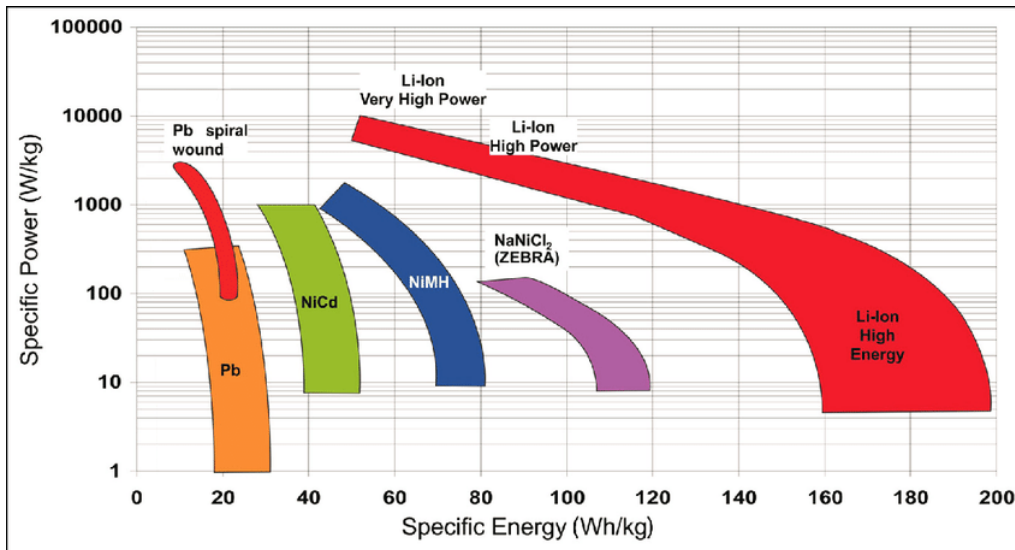


Figure 2: Ragone plot of various battery technologies [15].

1.2 Battery Models

With the ever-increasing development of distributed generations based on renewable energy sources (RESs), energy storage systems, especially batteries, assume a key role. The number of electric vehicles in circulation, with the aim of reducing CO₂ emissions into the atmosphere due to traditional combustion vehicles, also plays an important role in the development and diffusion of batteries. For these reasons, it becomes essential to know the available charge left in the battery, how long it will be able to supply the required energy, and also its useful life. This requires an efficient model that can accurately monitor battery performance and other critical parameters, such as state of charge (SoC), state of health (SoH), and current delivery. Many models in the scientific field have been proposed in order to have accurate monitoring of the batteries dynamically. Among the most widespread and used models to describe the correct behaviour of batteries, there are three categories: electrochemical models, mathematical models, and electrical models. The electrochemical model of a battery is structurally based on the internal electrochemical actions and reactions of a cell. Although accurate, this model is complex and requires precise recognition of the electrochemical processes in the cell. It is not applied in power studies and dynamical systems [16]. Mathematical models adopt empirical equations or mathematical methods as stochastic approaches to predict system-level behaviour such as battery run-time, efficiency, and battery capacity. However, presented a very high computational level. Electrical models, the accuracy of which lies between electrochemical and mathematical models, are the equivalent electrical models of a battery comprising voltage generators, resistors, and capacitors for co-design and co-simulation with other electrical circuits. They are more intuitive, useful, and easier to manage for electrical engineers.

In the following, some of these models used to describe the behaviour of the batteries, are briefly presented.

1.2.1 Electrochemical Models

Electrochemical models are based on the chemical processes that take place in the battery. The models describe these battery processes in great detail. This makes these models the most accurate battery models. However, the highly detailed description makes the models complex and difficult to set up. Doyle, Fuller, and Newman developed an electrochemical model for lithium and lithium-ion cells [17]. This model consists of six-coupled, non-linear differential equations. Solving these equations gives the voltage and current as functions of time, and the potentials in the electrolyte and electrode phases, salt concentration, reaction rate, and current density in the electrolyte as functions of time and position in the cell. Dualfoil is a Fortran program that uses this model to simulate lithium-ion batteries. The program is freely available on

the internet [18]. It computes how all the battery properties change over time for the load profile set by the user. From the output data, it is possible to obtain the battery lifetime. Besides the load profile, the user has to set over 50 battery-related parameters, e.g., the thickness of the electrodes, the initial salt concentration in the electrolyte, and the overall heat capacity. To be able to set all these parameters one needs a very detailed knowledge of the battery that is to be modelled. On the other hand, the accuracy of the program is very high. The program is often used as a comparison against other models, instead of using experimental results to check the accuracy.

1.2.2 Mathematical Models

The concept in these models is to define the voltage of the battery as a function of current, SoC, and some DC gain. The parameters are found in such a way that minimizes the root mean square error between the model voltage and the true voltage. Therefore, some tests data must be available in advance to find the parameters of these models.

Shepherd Model

The Shepherd model [19] describes the voltage of the output battery variation according to the charging/discharging current. It is suitable for all battery types with a minimum of experimental data. The general Shepherd equation is given by

$$y_k = E_0 - Ri_k - \frac{\mu}{(SoC)_k}$$

where k is a time index, y_k is the model voltage, E_0 is a DC (direct current) gain, R is the cell internal resistance, i_k is the cell current (positive for discharge and negative for a charge), and μ is a constant used for curve fitting. This equation is suitable for all battery typologies with a minimum of experimental data, for discharge and charge modes [20].

Nernst Model

The standard electrochemical potential defines the voltage between a redox reaction under standard conditions. The voltage also depends on the concentration (for liquids) or pressure (for gaseous reactants) of the components in the redox reaction since the average energy of the components will be altered by changes in concentration or pressure. The voltage in conditions different from the standard ones is given by the Nernst equation. A key implication of the Nernst equation is that the voltage of a battery is not necessarily constant, but varies as it is charged or discharged as the concentration of the components of the electrolyte changes. Applied for the voltage of a battery, the model based

on the Nernst equation is the following:

$$y_k = E_0 - Ri_k + \mu_1 \ln(\text{SoC}_k) + \mu_2 \ln(1 - \text{SoC})$$

where k is a time index, y_k is the model voltage, E_0 is a DC gain, R is the cell internal resistance, i_k is the cell current (positive for discharge and negative for charge), and μ_1 and μ_2 are constants used for curve fitting.

1.2.3 Electrical Models

Electric models for representing the behaviour of batteries are the most used in the energy sector. Their accuracy lies between electrochemical and mathematical models, but with a lower computational level. The effects of the various oxidation and reduction reactions are represented by simple electrical elements, such as voltage generators, resistors, and capacitors. They are intuitive, useful, and easy to handle. There are numerous techniques available by which a battery can be modelled. A few of them are described below.

Simple Equivalent Circuit Model

This model consists of an ideal battery with open-circuit voltage OCV and a constant internal resistance R_0 (Fig. 3). The terminal voltage V_L can be obtained from the open-circuit measurement and R_0 can be obtained from both open-circuit measurements and one extra measurement with the load connected at the terminal when the battery is fully charged [21]. The result is an electrical circuit, called Thévenin equivalent circuit, by the French engineer Leon Charles Thévenin, through which the behaviour of the battery is described. The major drawback of this model is the fact that both the internal resistance and the OCV are constant.

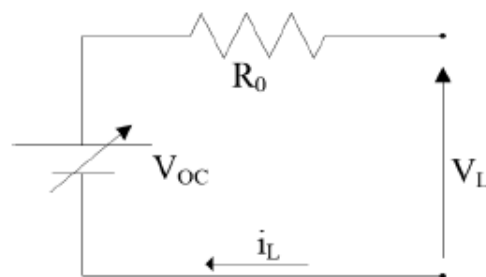


Figure 3: Equivalent circuit of the zeroth-order.

n-Order Equivalent Circuit Model

The Zeroth-order model is an improvement of the previous model. In this model, the electrical parameters, shown in Fig. 4, are not assumed constant but vary in accordance with the battery's SoC, and temperature. For this reason, a series of tests have to be carried out to evaluate the parameters in different battery states. Zeroth-order models are highly utilized in system-level simulations for control optimization and initial system design. A limitation of this model concerns the not being able to represent the voltage transients due to current variations during the charging or discharging phases and for the non-ideality of the reactions that take place in the cells. To overcome this problem, the circuit can be modified by introducing one or more parallel RC circuits in series to the static resistance (Fig. 4). In this way, one or more time constants are introduced into the circuit which allows to better characterize the dynamics of the battery. The increase in the number of RCs in a circuit offers better accuracy in following the dynamics of the battery but presents a high computational load of the model. The accuracy depends on the type of analysis to be performed to describe the operation of the battery.

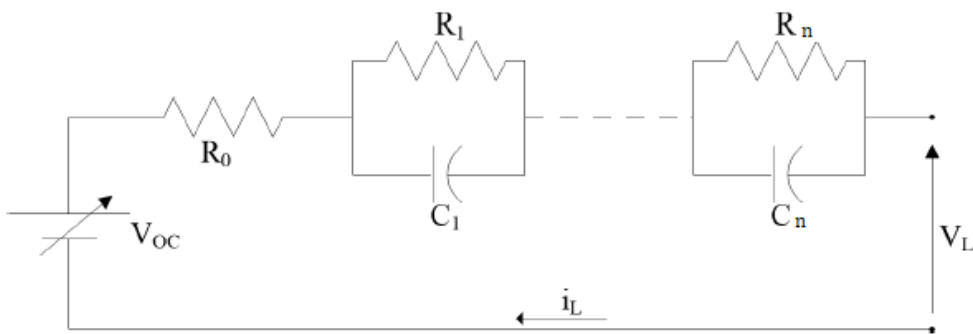


Figure 4: Equivalent circuit of the nth-order.

Impedance-based model

The model in Fig. 5 includes a combination of series resistors and series inductances to account for the internal resistance of the battery and impedance Z to model the electrochemical equivalent of the battery [22]. Impedance-based models use the electrochemical impedance spectroscopy method to obtain an ac-equivalent impedance model in the frequency domain, then use a complicated equivalent network to fit the impedance spectra. The adaptation process is complex, difficult, and not intuitive. Also, the impedance model only works for a constant SOC and temperature setting and therefore cannot predict DC response and battery runtime.

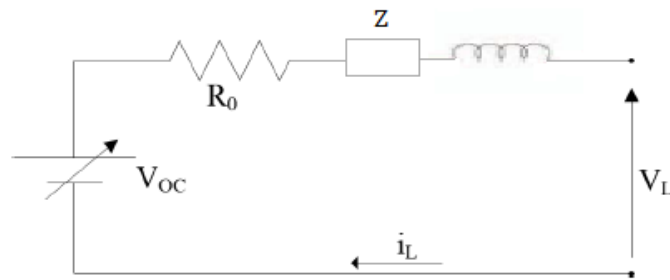


Figure 5: Impedance-based Battery Model.

1.3 Applications of Battery Energy Storage Systems

From an economic and technical point of view, BESS can find different applications. Many of these can be classified as stationary applications, such as grid services and RES exploitation. The increase in distributed generations creates an ever-growing problem in the management of the energy system, a problem that can be adequately solved with the support of the BESSs. Another field of application of BESS is represented by the growing increase of electric vehicles on the road. In fact, in addition to the management of the electric propulsion system, applications such as Fast Charging stations are gradually affecting the use of batteries, within the concept of second life.

Some of the applications for a BESS are described in the following.

1.3.1 Time-Shift

One of bulk energy services is electric energy time-shift which involves purchasing inexpensive electric energy, available during periods when prices or system marginal costs are low, to charge the BESS so that the stored energy can be used or sold at a later time when the price or costs are high. Alternatively, at the generation level from renewable sources such as wind or photovoltaic, storage can provide similar time-shift duty by storing excess energy production. Electric energy time-shift involves many possible transactions with economic merit based on the difference between the cost to purchase, store, and discharge energy (discharge cost) and the benefit derived when the energy is discharged. For this application, BESSs are required to have a large energy capacity with an extended charging/discharging duration (from hours to days). Besides, their efficiency is another crucial factor to consider when choosing BESSs for this application, since an outstanding amount of power will be wasted in an inefficient storage device [23].

1.3.2 Regulation and Reserves

Regulation is one of the ancillary services of BESS which provides for the management of interchange flows with other control areas in such a way that they closely correspond to the scheduled flows and the momentary changes in demand within the control area. Regulation is used to reconcile momentary differences caused by fluctuations in generation and loads. Regulation revenue consists of three parts: the capacity payment, which depends on the amount of the power bid; the service payment, based on the overall exchanged energy; the opportunity cost payment, which has to account for the missing revenue due to reduced production level [24]. Such a service can be profitable if provided by appropriate BESSs of low and medium capacity but with rapid response. Regulation seems very similar to reserve, but they occur in different situations: regulation must support the system in real-time in a continuous way, while the reserve consists of an additional generation capacity that must be kept aside to cope with power losses or sudden load increases. When some electrical power resources become unexpectedly unavailable, reserve capacity is required to ensure continued operation in the electrical network. In general, the reserves are at least as large as the single largest resource serving the system (for example, the single largest generating unit), and the not used capacity is equivalent to 15%-20% of the normal electric supply capacity [25]. Based on the response time, three types of reserves can be distinguished:

- Spinning-reserve: response time from a few seconds to 5-10 minutes to compensate for generation or transmission outages;
- Supplementary reserve: response time from 5-10 minutes to half an hour;
- Back-up reserve: cannot be quickly ready, but can operate over long periods of time.

Generally, the spinning reserve must be able to respond very quickly, but it is not required to operate for long periods of time. In fact, the spinning reserve is replaced by supplementary reserve and, in turn, by backup reserve as soon as they are available. All reserve services are remunerated for power availability and for the energy delivered. Conventional batteries have been already experimented with successfully for both spinning and supplementary reserve, whereas flow batteries seem to be another promising solution.

1.3.3 Frequency Response

Another applicable service of BESS is a frequency response that is very similar to regulation, described above, except it reacts to more general system needs in even shorter time periods of seconds to less than a minute when there is a sudden loss of a generation unit or a transmission line. The size of storage systems to be used in frequency response mode is proportional to the grid or

balancing area in which they are needed. Generally, storage systems up to 20 MW and greater size can provide effective frequency response due to their fast action. However, the location of the storage system within the grid with respect to other generations, transmission corridors, and loads plays a crucial role in the effectiveness as a frequency response resource.

1.3.4 Power Quality and Power Reliability

The Power Quality service involves using storage to protect customer on-site loads downstream (from storage) against short-duration events that affect the quality of power delivered to the customer's loads. The use of BESSs can enhance solutions also to compensate for harmonic disturbances. Power reliability means A storage system can effectively support customer loads when there is a total loss of power from the source utility. This support requires the storage system and customer loads to island during the grid outage and resynchronize with the grid when power is restored.

1.3.5 Load Levelling and Peak Shaving

Load levelling is a service addressed to the distribution utility for reducing the fluctuations of the load demand along the day. Load leveling can be achieved by using 'demand side' measures that reduce the peak demand or by using storage systems able to store energy during light load hours and discharge it during peak load hours. In this case, the installation of a BESS allows for a minimization of the difference between the mean and peak power requests. One of the main advantages for the distribution system operator based on using BESS is related to avoiding new investments in transmission and distribution facilities [26]. Peak shaving refers to industrial customers that can install a BESS to discharge power during peak power periods and charge during low demand periods [27]. The benefits of this application include a reduction in energy cost by reducing peak demand, reduction in energy generation cost by maintaining peak power demand, and avoiding investment cost to install more electricity generating units.

1.3.6 Electric Vehicles and Charging Stations

Recently, electric vehicles (EVs) have found increasing interest from researchers and manufacturers around the world. In particular, EVs are very promising thanks to their high efficiency and low environmental impact, together with the possibility of being recharged directly from power plants and from renewable sources [14]. However, their market diffusion is still limited. Indeed, electric vehicles are characterized by a limited driving range compared to vehicles based on internal combustion engines (ICE) due to size and weight constraints. EVs can be roughly divided into two broad classes, namely plug-in and non-

plug-in electric vehicles, depending on their ability to be recharged from the mains. Non-plug-in electric vehicles are essentially hybrid electric vehicles (HEVs), where propulsion is usually provided by a combination of an ICE and a small electric propulsion system. In particular, the engine operates at relatively high efficiency, while the battery is recharged via regenerative braking or via the engine, resulting in a rather long range of mobility thanks to the gas tank. As a result, HEV batteries are characterized by relatively low energy capacities, typically around 3 kWh, so they are not particularly expensive. Plug-in electric vehicles are available from much larger capacity batteries than HEVs (around 30 kWh), which guarantees a greater all-electric driving range. Specifically, battery electric vehicles (BEVs) are equipped with an all-electric propulsion system. BEVs have the advantage of simpler transmission than HEVs, but the BESS power and energy requirements are much more significant. Lithium-ion batteries are thought of as the best solution for BEVs, due to their high energy density and power capacity.

Well-known challenges related to large-scale electric vehicle distribution are the high cost of the battery pack (200-500 \$/kWh), the uncertainty about the cell life cycle, and the charging time [28]. The use of retired electric vehicle traction batteries for less demanding fixed and grid-connected applications is considered a viable solution to promote the widespread adoption of electric vehicles and provide a secondary revenue stream for Original Equipment Manufacturers (OEMs) and vehicle owners, promoting at the same time more sustainable mobility [29]. Automotive battery packs that have lost 20% of their initial capacity or have a fault condition are generally removed by the electric vehicle propulsion application (Automotive End-of-Life EOL) and sent to recycling facilities [30]. Automotive battery packs are expected to have an average lifespan of 8-10 years, while commercial vehicle applications may result in a battery life of 4-5 years. Therefore, it is estimated that a large number of Second Life Batteries (SLBs) will be available in the near future. The refurbishment of these battery packs and their use in grid-connected applications can help recover some of the investment costs and minimize the cradle-to-grave environmental impact of automotive battery packs. The SLB business plays an important role in the market as it represents a great opportunity for cost reduction and performance improvement for grid-connected systems, or more generally for stationary electricity storage systems, allowing the use of lithium-ion batteries where it would not otherwise be feasible. The integration of SLB into EV DC fast-charging stations (DCFCs) is becoming more and more popular [31]. DCFC installations having full capacity are not always possible, because of the limitation of grid connection and operating costs (eg. A cost-effective approach may involve integrating SLBs from the automotive world into DCFC stations.

Chapter 2

The Sodium Metal Halide Battery

Various battery technologies are implemented in the integration of RES and in the development of the concept of smart grids. Among the most common are lead-acid, lithium-ion, and sodium-sulfur batteries. However, their use in stationary applications is not widespread due to a series of limitations of each technology. For example, lead-acid batteries suffer from limited life cycles, low energy density, and have materials that are toxic to the environment (lead); lithium-ion batteries are among the most performing and widespread, especially for EVs, but have high energy costs and thermal management problems; finally, the NaS batteries present several problems in terms of safety. In this scenario, SMHBs (Sodium Metal Halide Batteries) are one of the most interesting energy storage systems for stationary applications [32].

SMHBs, also called ZEBRA batteries (Zero Emission Battery Research Activities), were developed in the first half of the 1970s in South Africa. They are high-temperature batteries and are characterized by the great availability of materials (sodium chloride and nickel) and by a high discharge rate, fast response to power demand, immunity to ambient temperature, unitary Coulomb efficiency, and intrinsic safety [33, 34]. One of the most attractive features of the SMHB technology is its ability to provide short-time and high peak power pulses at any operating state of charge (SoC) [35]. This is achieved by doping the cathodic active material with iron, forming a second sodium-iron cell. However, the implementation of this solution introduces critical issues in Battery Management System (BMS) especially when the SoC reaches values under 20%. This is due to the non-linear behaviour of the SMHB. For this reason, the operative range of the SoC is limited by BMS to 20%, reducing consequently the exploitation of the SMHB full capacity potential. Moreover, the SMHB model inaccuracy does not allow the implementation of an SoC estimator, imposing the use of a coulomb counter for SoC evaluation. Unfortunately, the use of coulombic counting requires periodical full charging in order to reset the integration offset. Therefore, when the BMS requires the coulomb counter reset, provision of energy services by means of battery energy management is not possible.

Hence, the development of accurate models of the SMHB, able to mimic electrical behaviour in a wide range of SoC, represents an important topic in

the full exploitation of the SMHB capacity. Furthermore, the availability of such models allows for the development of a novel SoC estimator able to overcome the above-mentioned limitations. As described in the previous chapter, battery models can be clustered into three main classes: electrochemistry, mathematics, and electrical. Electrical models are mostly used in electrical engineering applications due to their simplicity and accuracy, which require a low computational load. They provide dynamic simulations of battery quantities that fit well with experimental ones. In particular, the models based on Thévenin are characterized by different circuit topologies capable of providing a much higher precision. They use resistors, capacitors, and voltage sources whose values are related to the SoC [36]. Their values are experimentally determined [37].

The SMHB electrical models are mainly based on the Thévenin circuit approach [38–41]. Of great interest for this thesis work were the studies on first and second-order circuit models. In particular, a two RC-branch electrical model has been proposed [40]. It is characterized by a standard parameters identification process, performed by the application of a sequence of current steps at different values of SoC. Subsequent investigations have revealed inaccuracy in the identification of the equivalent circuit parameters at low values of SoC. This has been mainly due to iron-doping effects. Implementation of optimization algorithms has minimized the identification errors. However, a high computational burden has been required. The subsequent analysis of model parameters dependence by the SoC has highlighted a decoupling between the values expected by electrochemical assessments and the identified ones [41]. The second-order circuit models present in the literature represent the dynamics of SMHB well, for SoC values higher than 40%. For lower SoC values, the iron doping introduces non-linearity, making the evaluation of the parameters less accurate. This chapter presents two second-order circuit models that consider the presence of iron reactions. The identification of the parameters is done through a fitting procedure that takes into account the physical constraints of the battery. The results of these two models are compared with each other and with a model obtained through a standard and optimization procedure, which however does not take into account the effects of iron doping. The results show a significant improvement in the SoC assessment for the range between 40% and 10%, increasing its potential exploitation.

2.1 SMHB's characteristics

The SMHB is made up of several cells connected in series with each other. The SMHC (Sodium Metal Halide Cell) is very similar to classic NaS cells. They work at high temperatures (265–330°C) and consist of a hermetically sealed metal container, the walls of which act as a negative pole while the top acts as a positive pole, connected with a nickel rod which acts as an

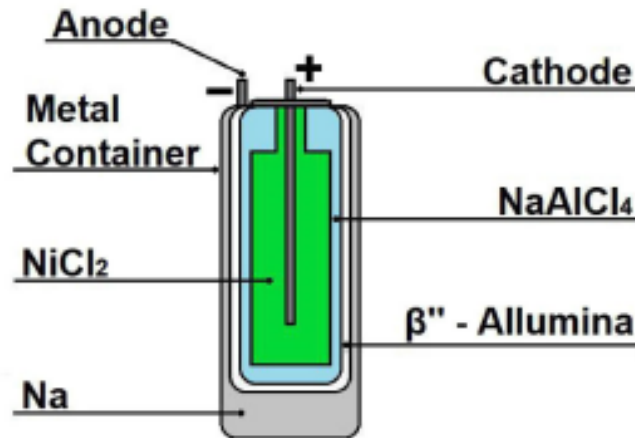


Figure 6: Schematic description of the SMHC.

internal current collector (Fig. 6). The negative electrode (anode) of the SMHC is made up of sodium (Na), while the positive electrode (cathode) is made up of nickel chloride (NiCl_2). Both electrodes are in the molten state during the operation of the SMHC. The two electrodes are physically separated by a solid ceramic electrolyte, consisting of β -alumina, which avoids the mixing of the two electrodes. The electrolyte allows the selective migration of the Na^+ ions that are the inner-battery charge carriers. To ensure greater safety from a chemical point of view, in the cathode section was inserted a second electrolyte, the tetrachloride aluminate (NaAlCl_4). In addition to increasing the ionic flow through the ceramic layer, the second electrolyte allows the formation of aluminium in the event of cracks in the β -alumina. The formation of aluminium seals the cracks in the ceramic layer, keeping the cell active. In the event of major cracks, aluminium short-circuits the cell, ensuring battery operation.

The typical shape of the cell is cylindrical, in which the innermost part represents the positive electrode, while the outermost part represents the negative electrode. The cylindrical shape represents the ceramic layer's shape of the electrolyte. In subsequent generations of SMHBs, the ceramic layer was changed to a quatrefoil shape. This geometry allows reducing the average distance between the electrolyte and the positive electrode, with a consequent reduction of the internal resistance of the cell, and an increase in the efficiency of the system [42]. The two shapes of the cells are shown in Fig. 7.

The SMHB is a secondary type battery characterized by the electrochemical reaction reported in (1). The symbols (\rightarrow) (\leftarrow) point out the discharge and charge reactions, respectively, occurring at an open circuit voltage (OCV) of 2.58 V (OCV_{Ni}).



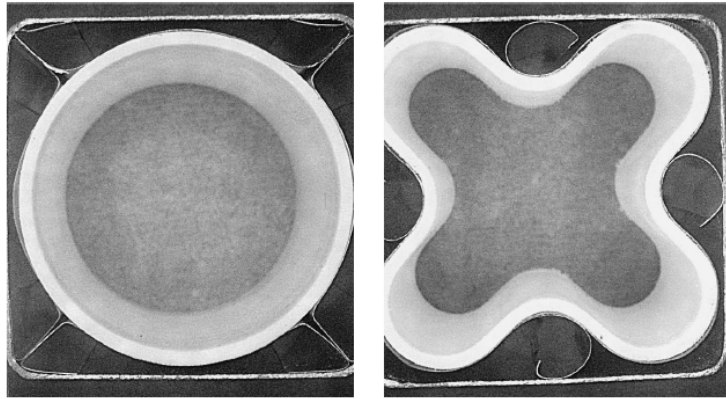


Figure 7: Comparison between the cross-sections of the ceramic electrolyte.

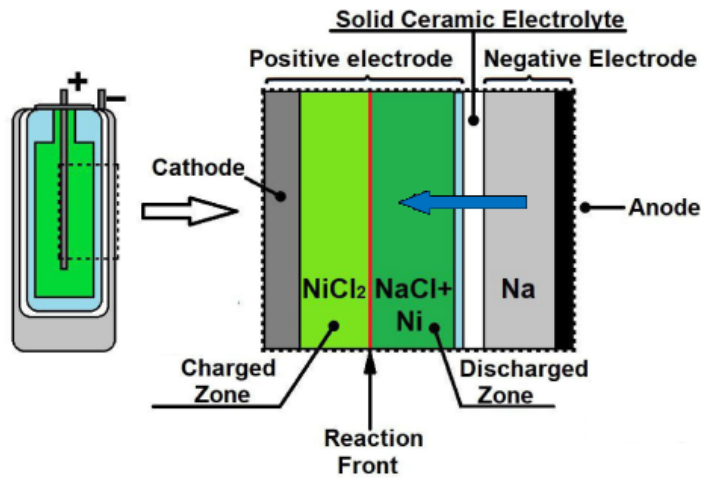


Figure 8: Schematic description of the SMHC during discharging phase. Blue arrow represents the route of ions Na^+ .

A schematic description of the chemical reactions taking place inside the cell is shown in Fig. 8. During the discharging phase, nickel-chloride and liquid metallic sodium react to generate salt and solid nickel. During the charging phase, sodium-chloride reacts with nickel to generate nickel-chloride. The reaction front moves away from the electrolyte as the battery discharges. This phenomenon determines the characteristic increase in internal resistance for these types of batteries. In order to increase SMHC power density, the cathode is doped with iron active materials, as mentioned previously. The iron operates in the SMHC in the same manner as nickel (2), but at an OCV equal to 2.35 V (OCV_{Fe}).



Thus, the reaction of iron occurs in the SMHC just when the output voltage reaches a value ≤ 2.35 V. Hence, during a constant current discharge, the output charges are first generated only by reducing the nickel-chloride until the output

voltage reaches OCV_{Fe} . Subsequently, the output current is generated by the reduction of iron-chloride. However, if a current pulse occurs, the inner cell voltage drop can send the battery voltage below the OCV_{Fe} . This activates both the reactions, (1) and (2), contributing to an increase in output power. When the demand of the SMHC current decreases, the battery voltage rises over 2.35V. In this condition only the iron-chloride reaction switches to charging mode, recovering the $FeCl_2$. This process persists until the iron, produced during the discharging pulse, is completely oxidized. The chemical reactions involving iron are faster than nickel one modifying consequently the dynamic evolution of the output voltage.

Considering the cell reactions depicted above, the modelling of SMHB is particularly complex and assumes a non-linear behaviour depending on the SoC, the temperature, and the current rate. In particular, the current rate can activate the iron reactions that are difficult to reproduce considering just the nickel-based model reported in the technical literature. Therefore, the definition of a simplified model that represents correctly the dynamic evolution of the phenomena occurring in the battery is fundamental for the management of SMHB.

2.2 Model of the SMHB

The modelling of the battery is based on an electrical model, and more precisely on the model of the Thévenin equivalent circuit. The Thévenin equivalent circuit is the model most used in engineering applications to represent the dynamic behaviours of the battery due to its precision and flexibility. It is characterised by the presence of a controlled voltage source OCV, an internal resistance R_0 and a variable number of RC branches connected in series. The higher the number of RC branches, the higher the accuracy will be. However, this implies a higher computational effort. Two series RC parallel circuits are usually considered the most appropriate compromise in battery modelling (Fig. 9). The two RC branches describe the dynamics of the battery, in particular: R_1 and C_1 represent the fastest dynamics connected to the reactions, while R_2 and C_2 represent the slowest dynamics, resulting from the diffusion processes in the electrolyte. This configuration has been used also in the SMHB [43].

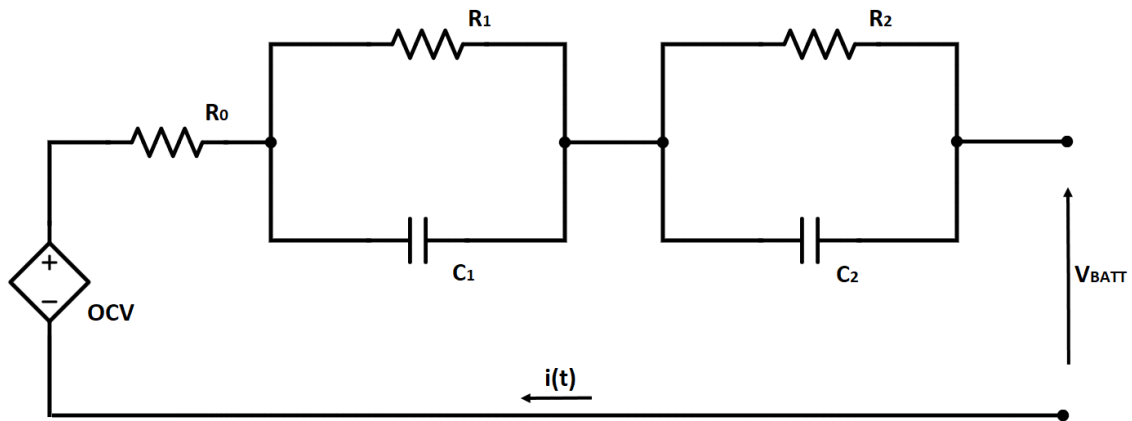


Figure 9: The general structure of a second-order Thévenin circuit model.

All elements of this circuit are characterised by the dependence of the SoC. Consequently, all the parameters of the equivalent circuit are subject to variation during the charging and discharging processes which are generally summarized by expressing them as a function of the SoC. So, for the correct implementation of battery modelling, an SoC estimator is needed. This estimator can be expressed as follows:

$$SoC(t) = SoC(0) + \frac{1}{C_B} \int_0^t i(t) dt \quad (3)$$

where, C_B represents the nominal battery capacity and i represents the battery current. The results obtained with this model demonstrate good performance in the SoC range from 90% to 40%, during discharge. The limitation at low SoC values is due to the presence of the reaction involving iron in the cathode (at low voltage values), seen in the previous section.

In order to reproduce the iron effects in SMHB, the classical two series RC parallel Thévenin equivalent circuit has been modified introducing another parallel branch. The configuration of the proposed equivalent circuit is shown in Fig. 10. The nickel reaction is modelled in the equivalent circuit through the branch composed of a voltage generator OCV_{Ni} , a resistance R_{Ni} and two series RC parallel branches. The R_{Ni} represents the nickel resistive contribute, while the two RC branches introduce two time constants that represent the voltage transient due to current variation during the charge and discharge phases. The iron reaction is modelled through the branch composed of a voltage generator OCV_{Fe} and a resistance R_{Fe} . The OCV_{Fe} has been set with a constant value, that represents the minimum threshold below which the iron reaction takes place (2.35 V for a single cell), while the R_{Fe} represents the iron resistive contribute. The choice of using two parallel iron resistance branches, having the same value R_{Fe} , responds to the requirement of decoupling the evaluation of the discharging and charging currents generated by (2) during the demand of

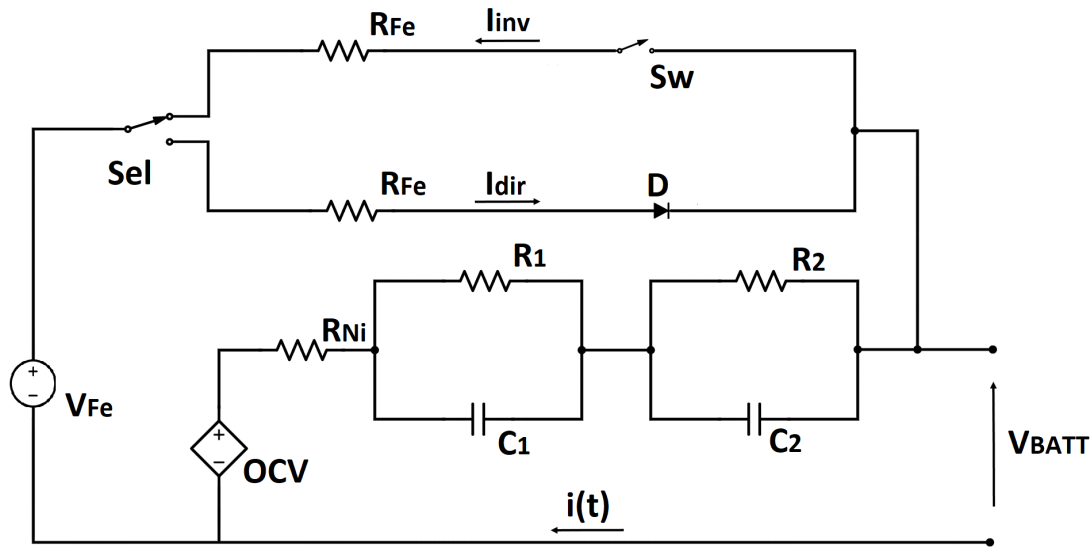


Figure 10: The proposed model of the SMHB.

the pulse current. This solution splits the management of the discharging and charging processes of the iron, allowing the coulombic counting of discharging I_{dir} and charging I_{inv} currents. This is fundamental to the correct modelling of the iron-doping effects during the application of pulse currents.

The switches S_{el} and S_w manage the connection of the iron model in the nickel one. The S_{el} switch is placed between the constant voltage generator and the iron branch and its task is to let the current flows in one of the two iron branches. When the output voltage V_{BATT} is lower than the iron threshold level, the current flows towards the battery terminals, and an integrator counts the amount of charge that flows in that direction; while if the output voltage is higher than the iron threshold level, the current flows in the reverse direction and another coulomb counter measures the charge flowing. The switch S_w is controlled by the state of the two coulomb counters which measure the charges associated with the current flows I_{dir} and I_{inv} . In particular, if the coulomb counter associated with the current I_{inv} is zero, S_w is turned on. The S_w is turned off when I_{inv} is different from zero and the coulomb counter I_{inv} assumes a value equal to the last value of the coulomb counter I_{dir} . This means that all the charges of the iron-sodium reaction that flowed during the discharge have been returned. The detection of the condition of equality between the two coulomb counters resets them both in order to be able to repeat the modelling when a similar condition occurs.

To identify the values of the parameters present in the equivalent circuit, some assumptions have been done, reported in the following:

- charge/discharge OCV_{Ni} has been expressed as just a function of SoC;

- the temperature dependence of OCV_{Ni} and OCV_{Fe} has been considered negligible, due to the temperature control of the SMHB's BMS that guarantees an operating range within 270-330°C;
- resistances and capacitors of the nickel model depend only on the SoC;
- dependence of the internal resistances R_{Ni} and R_{Fe} to the current rate is not taken directly into account.

As mentioned, the parameters of the equivalent circuit can be expressed as just a function of the SoC. Referring to the model shown in Fig. 10, the output voltage $V_{BATT}(t)$ is described by (4) and (5). Output current is given by (6), where $I_{Ni}(t)$ is the current evolution in the nickel branch.

$$V_{BATT} = OCV_{Ni}(t) - V_{Ni}(t) - V_1(t) - V_2(t) \quad (4)$$

$$V_{BATT} = OCV_{Fe}(t) - V_{Fe}(t) \quad (5)$$

$$I_{BATT} = I_{Ni}(t) + I_{dir} - I_{inv} \quad (6)$$

OCV_{Ni} and OCV_{Fe} are the evolutions of the open-circuit voltage in the two meshes of the circuit. V_{Ni} , V_1 and V_2 are the instantaneous evolution of voltage drops of the nickel branch on R_{Ni} , R_1C_1 and R_2C_2 respectively. V_{Fe} is the voltage drop of the iron branch on R_{Fe} . Peculiarly, the OCV_{Fe} is not time-dependent, because is a constant value equal to the iron reaction threshold. The combination of the two equations yields the model equation:

$$2V_{BATT} = OCV_{Ni}(t) + OCV_{Fe} - V_{Ni}(t) - V_1(t) - V_2(t) - V_{Fe}(t) \quad (7)$$

The voltage values can be expressed in the time domain as follows:

$$\begin{aligned} V_{Ni}(t) &= R_{Ni} * i(t) \\ V_{Fe}(t) &= R_{Fe} * i(t) \\ V_1(t) &= v_1(0) * e^{-\frac{t}{\tau_1}} \\ V_2(t) &= v_2(0) * e^{-\frac{t}{\tau_2}} \end{aligned} \quad (8)$$

where, $v_1(0)$ and $v_2(0)$ represent the voltages on capacities C_1 and C_2 at the time $t = 0$, τ_1 and τ_2 are the time constants of the two RC branches.

The analytical solution in the time domain, in order to determine the circuit parameters, is quite complex due to the presence of differential equations. In first approximation, can be considered that the dynamic evolution of the circuit parameters, which depend on the variation of the SoC, is slower than

the fast dynamics of the battery voltage, consequently it can be assumed that the parameters of the equivalent circuit are constant. Therefore, the equation in the Laplace domain can be solved by converting the differential equations into linear equations in the complex variable s . The Laplace transformation of (7) is reported in the following:

$$2V_{BATT}(s) = OCV_{Ni}(s) + OCV_{Fe}(s) - V_{Ni}(s) - V_1(s) - V_2(s) - V_{Fe}(s) \quad (9)$$

In order to obtain the circuit parameters, a step current has been set. Equation (10) shows the application of the Laplace transformation for a time instant t of a step current from I to zero (10).

$$I(s) = -\frac{I(e^{-ts} - 1)}{s} \quad (10)$$

The application of Laplace transform allows the evaluation of each element of (9), as reported in the (11).

$$\begin{aligned} OCV_{Ni}(s) &= \frac{OCV_{Ni}}{s} \\ OCV_{Fe}(s) &= \frac{OCV_{Fe}}{s} \\ V_{Ni}(s) &= \frac{R_{Ni}I(1 - e^{-ts})}{s} \\ V_{Fe}(s) &= \frac{R_{Fe}I(1 - e^{-ts})}{s} \\ V_1(s) &= \frac{R_1I(1 - e^{-ts})}{s(1 + \tau_1s)} + \frac{\tau_1}{1 + \tau_1s}v_1(0) \\ V_2(s) &= \frac{R_2I(1 - e^{-ts})}{s(1 + \tau_2s)} + \frac{\tau_2}{1 + \tau_2s}v_2(0) \end{aligned} \quad (11)$$

When a step current from I to zero on the equivalent battery circuit has been applied, the inverse Laplace transform of (9) allows determining the analytic solution of transient evolution of the terminal voltage. This assumes the form reported in (12) where the parameters k_1 , k_2 and k_3 are the model variables (reported in (13)) and τ_1 , τ_2 are the time constants related to both RC branches. δ_{-1} represents the unit step function (Heaviside function).

$$V_{BATT}(t) = k_1 + k_2e^{-\frac{t}{\tau_1}} + k_3e^{-\frac{t}{\tau_2}} \quad (12)$$

$$\begin{aligned} k_1 &= \frac{OCV_{Ni}}{2} + \frac{OCV_{Fe}}{2} + \frac{I}{2}(R_1 + R_2 + R_{Ni})(\delta_{-1}I - 1) + R_{Fe}\frac{I - I_{Ni}}{2} \\ k_2 &= \frac{R_1I}{2} - \frac{R_1I\delta_{-1}e^{\frac{t}{\tau_1}}}{2} - \frac{v_1(0)}{2} \\ k_3 &= \frac{R_2I}{2} - \frac{R_2I\delta_{-1}e^{\frac{t}{\tau_2}}}{2} - \frac{v_2(0)}{2} \end{aligned} \quad (13)$$

2.2.1 Parameter identification

The method used to identify the equivalent circuit parameters in Thevenin circuit modelling is based on the numerical analysis of the physical quantities of the measured battery. In order to validate the proposed modelling, the parameter identification process has been performed using a commercial SMHB: the FIAMM SoNick battery model ST523. It is characterized by the connection in a series of 240 cells enclosed in a metallic battery container. The FIAMM SoNick ST523 includes an electric heater for battery temperature management which is controlled by the BMS. Moreover, the BMS provides other functions, such as charge regulation, monitoring, and diagnostics, developed through the measurements of battery current, voltage, and temperature. The main operating data of the SMHB under test are reported in Table 2.

	Unit	Value
Rated discharge power	kW	7.8
Rated voltage	V	620
Electrical stored capacity	kWh	23.5
Volumetric energy density	kWh/m ³	280
Gravimetric energy density	Wh/kg	140
nominal temperature	°C	270
Calendar Life @ 80% DoD	years	15
Cycle-life @ 80% DoD	cycles	4500

Table 2: SMHB module characteristics of FIAMM SoNick ST523.

To develop the pulse tests and voltage measurements, the SMHB test bench was composed of an Elektro-Automatik generator model EA PSI 8150030, an Elektro-Automatik electronic load model EL 9750-75 HP, and a National Instruments data acquisition system model NI cDAQ-9172. All instruments were controlled by software developed in LabVIEW environment.

In order to identify the electrical model parameters, charging and discharging pulse tests have been performed on the test bench. All the tests have been distinguished by the application of a current profile characterized by the time evolution shown in Fig. 11. The tests have been conducted in sequences of step current output profiles consisting of the first portion at 5A that changed the SoC by 9%, and a second one at 10A that changed the SoC by 1%. Each test has been characterized by a rest time at zero A to reach the OCV steady-state value. In this way, it has been possible to verify the evolution of the parameters with a step of 10 % of the SoC, in charging and discharging phase. The step current applied generates a battery voltage evolution depicted in Fig. 12. The voltage response of the battery exhibits a double voltage drop at the double step

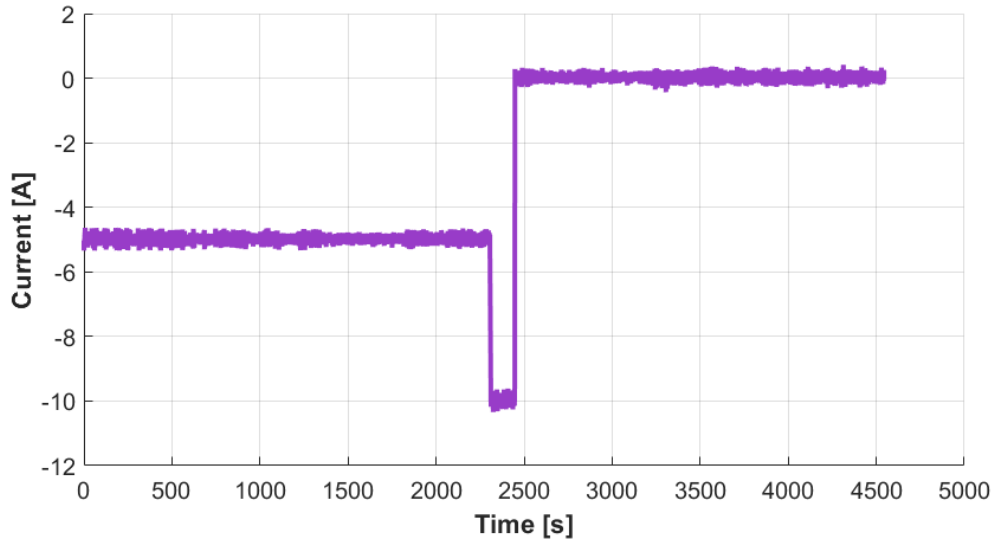


Figure 11: Step current evolution during a pulse discharge test on the SMHB.

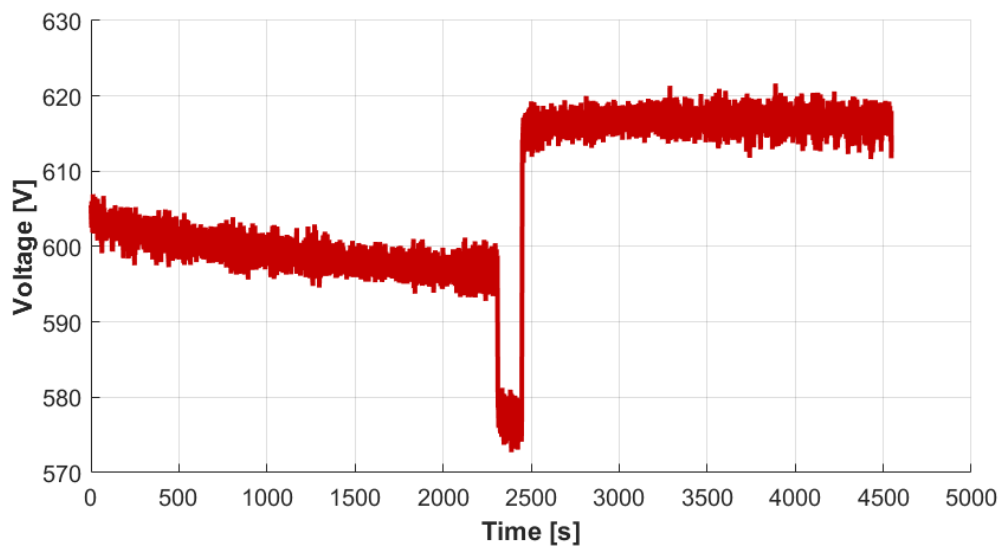


Figure 12: Voltage evolution during a step current applied in discharging phase.

current. The first step in identifying the parameters has been the determination of the internal resistance. By applying equation (14), the value of the internal resistance has been calculated, associated with the voltage variation when a step current is present.

$$R = \frac{\Delta V}{\Delta I} \quad (14)$$

In this way, it has been possible to obtain two values of internal resistance, each for a voltage drop. Moreover, it has been necessary to decouple the fast dynamic of the battery voltage from the slow one. Being identified near the same SoC value (difference of 1 %), by averaging the two internal resistance values it has been possible to obtain the internal resistance value for each SoC interval with greater precision. This value represents the resistances due to nickel and iron. However, it has been seen that the iron reaction is triggered only when the voltage reaches the threshold value. For the FIAMM SoNick ST523 battery, the threshold value of the iron reaction is 564 V. Therefore, the voltage drops for values higher than 564V are attributable only to the nickel resistance R_{Ni} .

A specific procedure for the evaluation of the resistance of iron R_{Fe} is required. During the tests, the iron threshold value is exceeded in the proximity of low SoC values (less than 30 %) and only during the discharge processes. When on the step current from 5A to 10A the voltage drop does not decrease under the limit threshold of 564V, it is possible to evaluate R_{Ni} as the ratio between voltage and current because it can be assumed that the current is only a function of the R_{Ni} . It is worth noting that during this step the current flows only through the nickel branch. Whereas, during the step current from 10A to zero A the voltage drop decrease under the threshold, so it is possible to determine R_{Fe} as the ratio between voltage and current, based on the superposition principle and assuming R_{Ni} as constant in the entire step (the variation between the two step current is 1% of the SoC).

In order to determine the RC-branch parameters, that portion of the voltage-time evolution that held the information about the battery dynamic has been processed. In particular, when the load has been disconnected, the battery freely evolved toward the OCV steady-state value. Hence, to calculate the RC-branch parameters, the experimental evolution of battery voltage has been fitted by (12). This procedure allowed the identification of parameters k_1 , k_2 , k_3 , τ_1 and τ_2 for each SoC step. Then, the application of (13) allowed evaluation of the circuit parameters R_1 , C_1 , R_2 and C_2 . In the fitting procedure, the value of k_1 has been set manually, equal to the value of the OCV of the reference step, which can be obtained from the trend of the curve in the relaxation time reached equilibrium.

Applying this procedure to the whole operational range of SoC, identification of electrical parameters of the proposed SMHB model has been developed for discharging and charging processes. In Table 3 and 4, the discharging and charging identified parameters are reported. It is possible to notice that passing

SoC	OCV [V]	R_{Ni} [Ω]	R_{Fe} [Ω]	R_1 [Ω]	R_2 [Ω]	C_1 [F]	C_2 [F]
90%	617.9	2.4	-	0.0611	0.1233	1181.7	25.25
80%	617.7	2.55	-	0.0804	0.2759	952.74	6.071
70%	617.5	2.62	-	0.0979	0.5357	1570.5	3.6065
60%	617.3	2.65	-	0.1351	1.107	1221.3	1.7886
50%	616.8	2.66	-	0.1827	1.463	846.74	1.6261
40%	616.6	2.39	-	0.2216	2.521	1430.5	2.3937
30%	616.4	2.48	4	0.2743	4.024	2155.3	5.7033
20%	614.4	2.82	4	0.5068	4.73	2.48	28.54
10%	576.7	2.7	4	0.2795	2.02	4.9517	438.86

Table 3: Discharging circuital parameters of the SMHB model.

SoC	OCV [V]	R_{Ni} [Ω]	R_{Fe} [Ω]	R_1 [Ω]	R_2 [Ω]	C_1 [F]	C_2 [F]
20%	616.8	2.12	-	0.2698	0.1392	23.94	1301.7
30%	617.3	2.14	-	0.3938	0.1371	17.58	946.75
40%	617.7	2.13	-	0.4431	0.1702	16.92	420.21
50%	617.8	2.25	-	0.5033	0.334	14.01	177.99
60%	617.8	2.29	-	0.6709	0.4489	14.62	183.47
70%	617.8	2.49	-	0.9602	0.852	16.34	144.01
80%	617.6	2.91	-	1.2282	1.7817	19.92	112.14
90%	617.6	3.15	-	1.6366	2.126	29.02	163.64

Table 4: Charging circuital parameters of the SMHB model.

from 30% to 20% of SoC, some parameters, such as capacities, drastically change their value. This is due to the difficulties in evaluating the parameters when the iron reaction takes place in parallel with the nickel reaction, and explains the different dynamics during this phenomenon. In the evaluation of the parameters during the charging phase, the BMS has been not allowed the battery to be discharged below 10%. Therefore, the charging tests were carried out starting from this last value.

2.2.2 Experimental result

Experimental tests have been carried out for the battery discharge and charge processes, applying a step current such as to reduce or increase the SoC by 10%. The experimental evolutions of battery discharge and charge are shown in the Fig. 13 and Fig. 14, respectively. The current profile in the charging phase

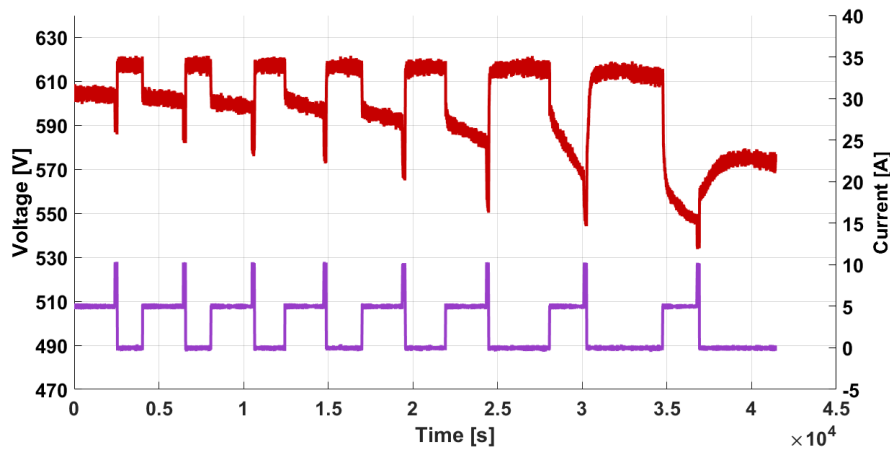


Figure 13: Time evolutions of voltage (red trace) and currents (purple trace) on SMHB during discharge test.

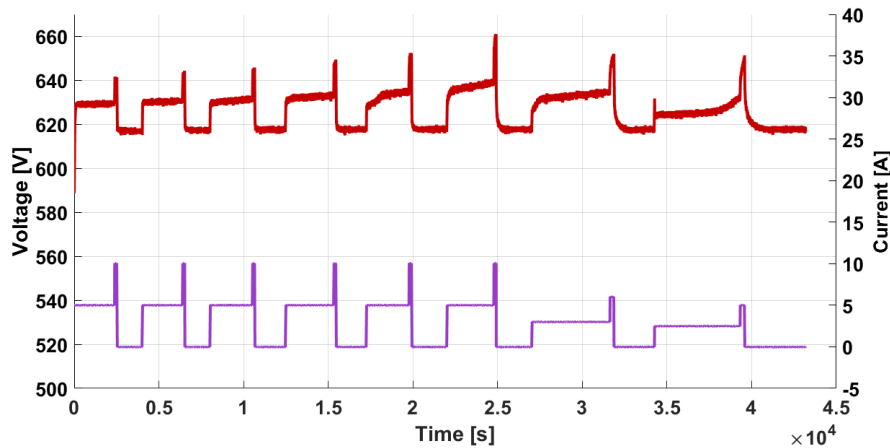


Figure 14: Time evolutions of voltage (red trace) and currents (purple trace) on SMHB during charge test.

has been changed in the SoC range between 80% and 90%. In fact, by applying a current of 10A, the BMS detected an over-voltage value and intervened by disconnecting the load, in order to safeguard the battery. To overcome this, two different step currents have been applied, keeping the ratio double on the step current in order to guarantee the same configuration as the previous tests.

The identified parameters allowed to develop of a model to simulate the battery voltage time evolution during tests. A comparison between model response and experimental curves has been investigated to verify the accuracy of the proposed model. Discharge test from 90% to 80% SoC range related to step current (violet trace) is shown in Fig. 15. In this interval of SoC, the iron does not intervene, because the output voltage values are over 564V during the entire test.

The proposed model (green trace) follows the evolution of the experimental voltage (red trace). As confirmation, the error between the experimental voltage

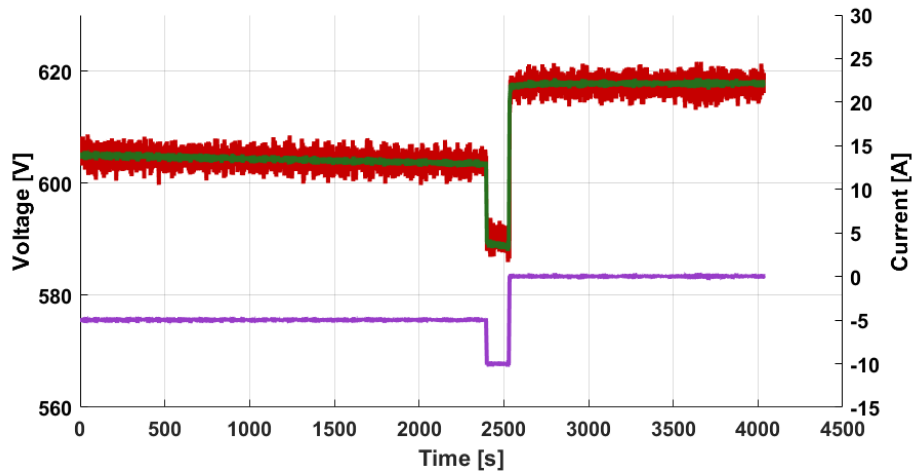


Figure 15: Comparison between experimental voltage (red trace) and simulated voltage with proposed model (green trace) at step current (purple trace) during the discharge phase from 90% to 80% of the SoC.

and simulated one by the model has been evaluated. Fig. 16 shows that the percent error is below 0.5%.

Discharge test from 40% to 30% of SoC range related to step current (violet trace) is shown in Fig. . In this interval, the iron effect on the dynamic battery starts. In this case, the proposed model (green trace) results to be coherent with experimental voltage evolution (red trace), as shown in Fig. where can be seen that the error presents an approximately constant error during the test and remains below 2%.

In order to highlight the improvement obtained, a comparison with a model without the iron modelling [41] has been reported in Fig. 19. It shows the experimental curve (red trace) compared to simulated voltage-time evolution with the proposed model (green trace) and voltage without the iron modelling (blue trace), during the discharge phase from 90% to 10% of SoC.

The corresponding percentage error is depicted in Fig. 20. The error of the model without the iron effect (blue trace) stand out more than the proposed model (green trace) confirming the improvement obtained by taking into account the iron effect, especially at low SoC (red trace). The step-current chosen allowed to identify more accurately R_{Ni} , and that explains the improvement between the proposed model and the original one.

All the tests performed in the discharge phase, have been proposed, in the same manner, to evaluate the model during the charge phase. A comparison between the experimental curve (red trace) and simulated voltage time evolution with the proposed model (green trace) during the charge phase from 10% to 90% SoC range has been shown in Fig. 21. The percentage error (green trace) during the charge phase, shown in Fig. 22, presents an approximately constant error during the test and remains below 1% until 80% of SoC, confirming the accuracy of the proposed model also in the charging phase.

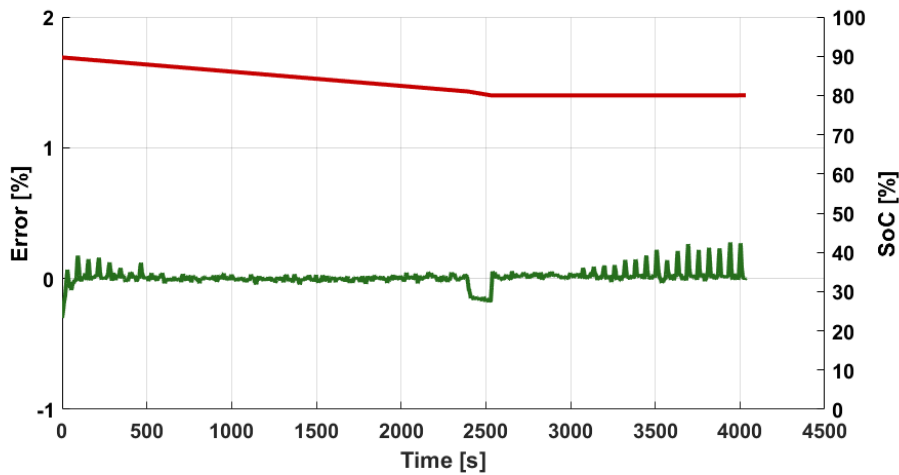


Figure 16: Error evolution from 90% to 80% of SoC. Green trace represents the evolution of the percentage error; red trace represents the SoC evolution.

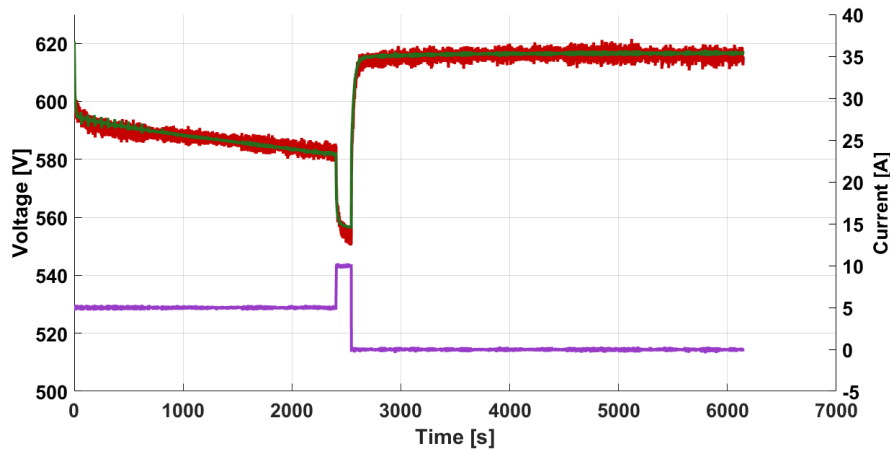


Figure 17: Comparison between experimental voltage (red trace) and simulated voltage with proposed model (green trace) to step-current (violet trace) during the discharge phase from 40% to 30% of SoC.

In order to validate the model, a discharge test with the power profile of a typical battery application with different currents has been implemented. In this test the battery has been discharged from 90% to 10% of SoC.

A comparison between the experimental evolution, the proposed model and the model without the iron effects has been done, as shown in Fig. 23. The proposed model follows the experimental evolution with a maximum error lesser than 1.5% for SoC greater than 30%, whereas the maximum error is 1.7% for an SoC value lower than 30%, as shown in Fig. 24. Moreover, it is possible to evaluate the improvement between the proposed model and that without the iron effect, especially for value below 30% of SoC.

Analogously, a charge test to simulate a typical application of a battery with different currents has been implemented. The battery has been charged

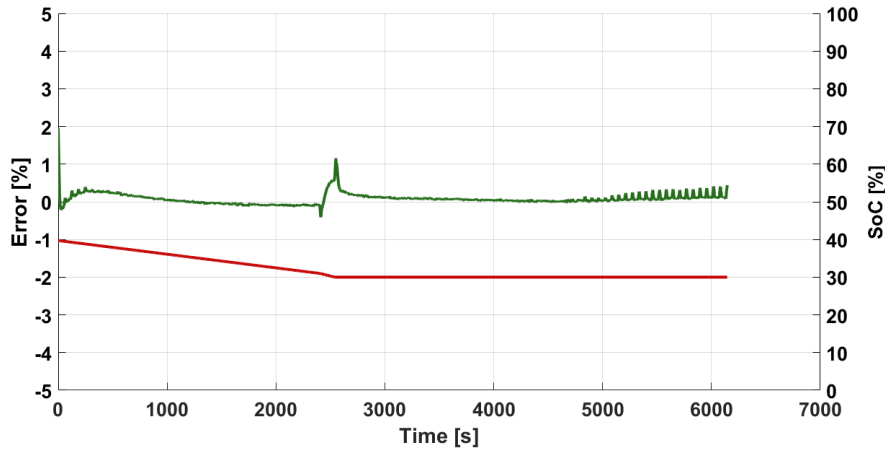


Figure 18: Error evolution from 40% to 30% of SoC. Green trace represents the evolution of the percentage error; red trace represents the SoC evolution.

from 10% to 90% of SoC. A comparison between experimental evolution (red trace) and the proposed model (green trace) is shown in Fig. . In this test, the maximum error is lesser than 1,5% for SoC, as shown in Fig..

2.3 Improved model

As explained in the previous section, the model based on the Thévenin equivalent circuit characterised by two RC branches presents a good accuracy in the dynamics of the SMHB. However, a minor mismatching between experimental and simulated results still occurs during the transient voltage evolution for SoC values $\leq 30\%$.

In order to improve the accuracy for low SoC values, the model shown in Fig. 10 has been improved by replacing the constant voltage generator OCV_{FE} with a variable generator V_{var} to simulate the behaviour of the iron inside the battery. The configuration and the management of the switches remain the same. The proposed mathematical model was developed with the same assumptions. The battery voltage output is described by the (12), where the only change is on k_1 , as shown in (15).

$$k_1 = \frac{OCV_{Ni}}{2} + \frac{V_{var}}{2} + \frac{I}{2}(R_1 + R_2 + R_{Ni})(\delta_{-1}I - 1) + R_{Fe} \frac{I - I_{Ni}}{2} \quad (15)$$

In fact, during the application of step current to zero, the current flowing in the iron branch ($I-I_c$) can assume a value different from zero. Therefore, a time variation of voltage drop on R_{Fe} can occur. Since, for the assumption of linearity, k_1 and OCV_{Ni} are constant, a compensation by means of voltage V_{var} has to be generated. This has supported the introduction of a time variable V_{var} when V_{BATT} is less to 564V (V_{th}) and I_{inv} is different to zero. This solution appears suitable to compensate for the mismatch occurring between experimental and simulated results during the transient voltage evolution for $SoC \leq 30\%$.

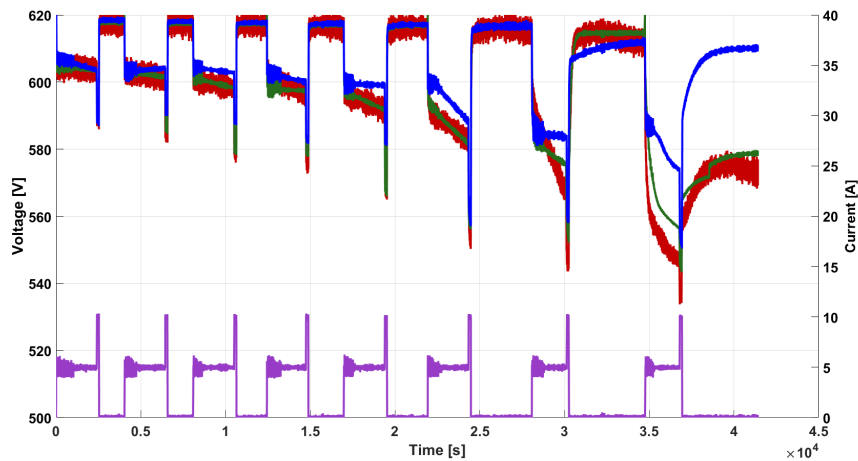


Figure 19: Comparison between experimental voltage (red trace), simulated voltage with proposed model (green trace) and simulated voltage without iron effect (blue trace) to step-current (violet trace) during the discharge from 90% to 10% of SoC.

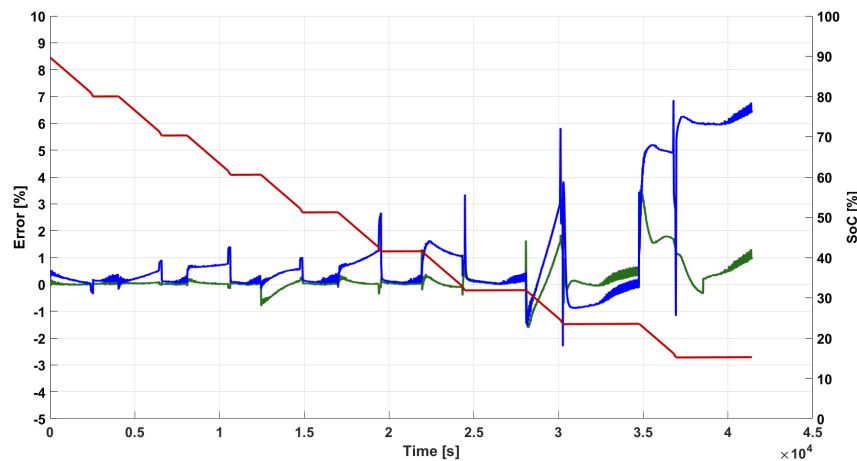


Figure 20: Percentage error evolution from 90% to 10% of SoC. Red trace represents the evolution of the SoC, green trace represents the percentage error considering the iron effect and the blue trace represents the percentage error without considering the iron effect.

From the chemical point of view, this effect can be justified by the presence of the parasitic iron drift phenomenon of the charging reaction (2) that is not modelled. In fact, during the charging process, the iron that is in the solid state is transformed into liquid iron chloride (FeCl_2). Consequently, the phase change introduces the drift phenomenon, necessary for the establishment of chemical equilibrium. This influences the time evolution of the iron charging current I_{inv} . To take into account this phenomenon, a novel function for the time

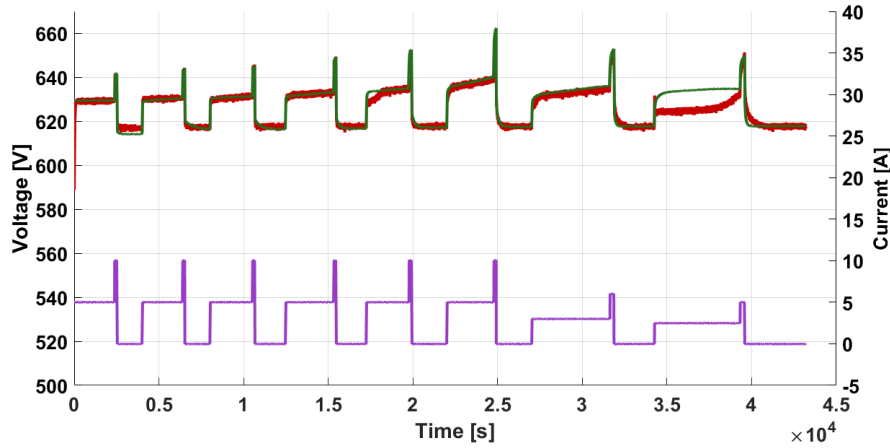


Figure 21: Comparison between experimental voltage (red trace), simulated voltage with proposed model (green trace) to step current (violet trace) during the charge from 10% to 90% of SoC.

evolution of generator V_{var} has been introduced. The proposed generalized of V_{var} is described in (16):

$$\begin{cases} V_{var} = V_{th}; & \text{with } I_{dir} > 0 \\ V_{var}(t) = V_{th} + \alpha t + e^{-\frac{t}{\tau_{Fe}}}; & \text{with } I_{inv} > 0 \end{cases} \quad (16)$$

As in the previous model proposed, identification of the SMHB equivalent circuit parameters has been performed using a numerical approach. It consisted of using the improved model as a fitting function to match with the experimental output battery voltage after discharge and charge pulse tests. The tests consisted of a sequence of current pulses characterised by a constant magnitude and span time aimed at reaching previously set values of SoC.

The steps followed for the parameters identification are summarized in the following:

1. application of discharging and charging pulse tests;
2. measurement of the voltage-time evolution and SoC during discharging and charging pulse tests;
3. evaluation of OCV_{Ni} for the different values of SoC;
4. estimation of internal resistance at different values of SoC, evaluating voltage drop in the application of a set step current;
5. estimation of the parameters k_1, k_2, k_3 by the numerical fitting of experimental results using the model (12);
6. estimation of the iron resistance R_{Fe} during the transition of V_{BATT} across the threshold iron-sodium value $V_{var} = (V_{th})$;

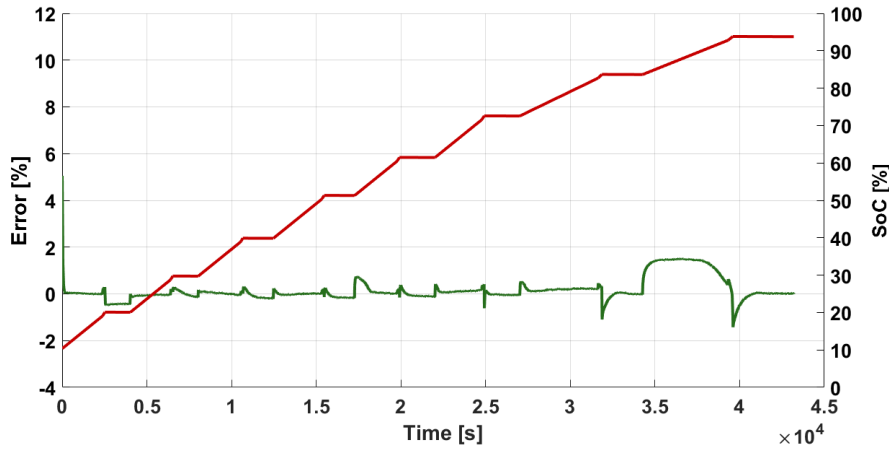


Figure 22: Percentage error evolution from 10% to 90% of SoC. Red trace represents the evolution of the SoC, green trace represents the percentage error of the proposed model.

7. estimation of the parameters R_1 , C_1 , R_2 and C_2 by the application of (13) in the whole operational range of SoC;
8. iterative fitting procedure for estimation of α and τ_{Fe} of $V_{var}(t)$ in the range of SoC below 30%.

A specific shape of battery current has been implemented during both charging and discharging phases. All of the tests have been developed considering step variations of SoC of 10%, as seen in the previous section (2.2.1). The battery operating range was between 10% and 90% due to manufacturing constraints associated with this type of technology.

Identification of R_{Fe} required a specific procedure. Detection of the battery voltage transition V_{BATT} across the triggering threshold V_{th} of the iron reaction has been necessary. Referring to the pulse test, the analysis of the voltage evolution during the application of maximum discharge current allowed the detection of the above-mentioned transition. Hence, knowing the parameters of the nickel branch and assuming that they were constant, it has been possible to determine the current flowing through this branch. Applying the superposition principle, the current flowing from the iron branch has been evaluated as a difference from the total current. Therefore, the R_{Fe} value for the SoC at which voltage transition occurs has been calculated. Estimation of R_{Fe} at lower SoC values required the implementation of a fitting procedure based on (16) because the superposition principle could not be further applied.

In Fig. 27, the SMHB voltage evolution, regarding the application of the step current during the SoC variation from 60% to 50% is shown. The area highlighted in ZOOM 1 has been numerically processed to determine resistances R_{Ni} and R_{Fe} , whereas the area ZOOM 2 has been processed to determine the RC-branch parameters. Specifically, the resistance R_{Ni} has been determined to be the ratio between voltage drop and the respective current magnitude. The

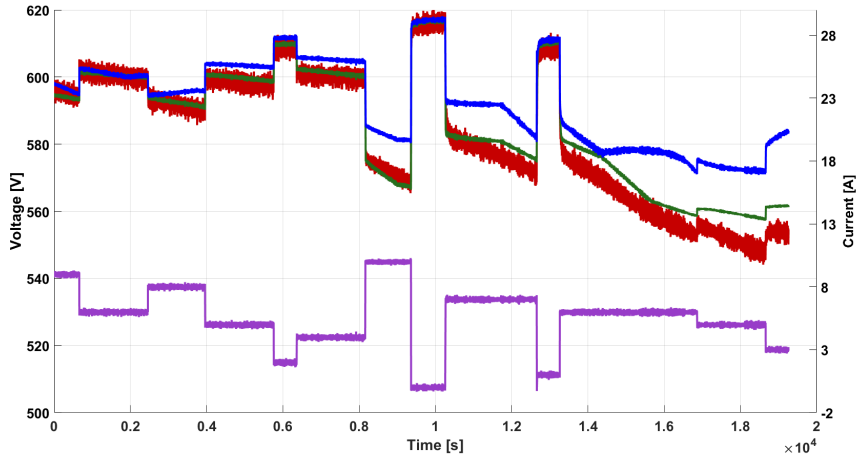


Figure 23: Comparison between experimental voltage (red trace), simulated voltage with proposed model (green trace) and simulated voltage without iron effect (blue trace) to different currents (violet trace) during the passage from 90% to 10% of SoC.

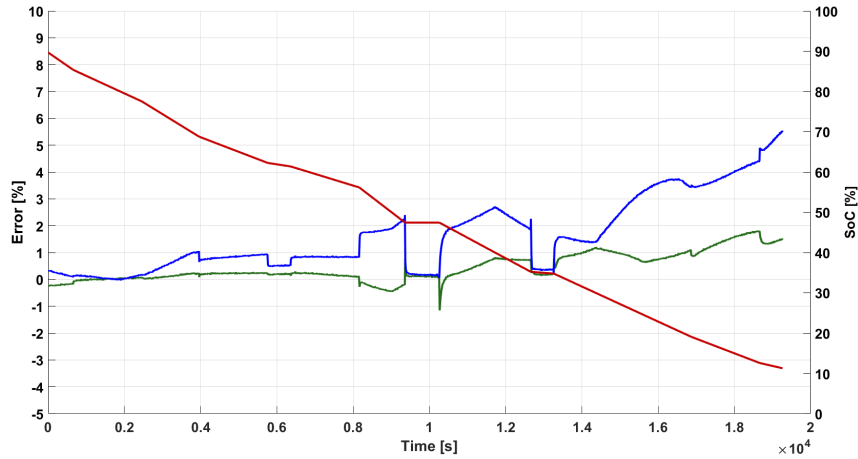


Figure 24: Error evolution from 90% to 10% of SoC to different currents. Red trace represents the evolution of SoC, green trace represents the percentage error considering iron effects (proposed model), and blue trace represents the percentage error without considering the iron effect.

more accurate the voltage drop estimation has been, the more precise has been the parameter. Therefore, to improve the accuracy of identification of R_{Ni} , the tests have been performed using two steps from 5A to 10A and from 10A to zero A. Each step corresponded to a voltage drop on the same resistance that allowed its identification by (17)

$$R_{Ni} = \left| \frac{(V_a - V_b)}{I_{5A}} \right|; \quad R_{Ni} = \left| \frac{(V_c - V_d)}{I_{10A}} \right| \quad (17)$$

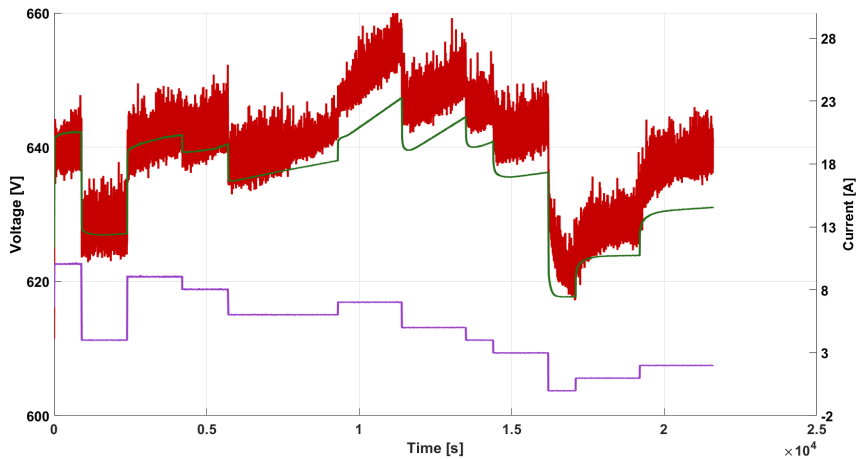


Figure 25: Comparison between experimental voltage (red trace), simulated voltage with proposed model (green trace) and simulated voltage to different currents (violet trace) during the passage from 10% to 90% of SoC.

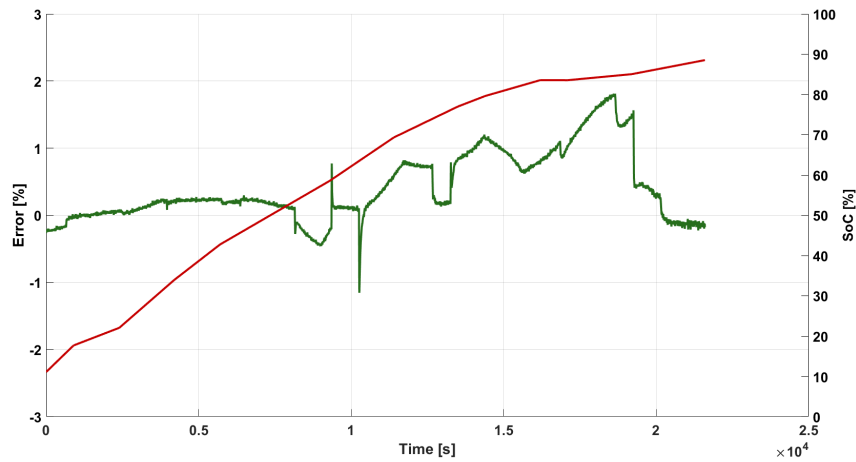


Figure 26: Error evolution from 10% to 90% of SoC to different currents. Red trace represents the evolution of SoC, green trace represents the percentage error of the proposed model.

Resistances evaluated by (17) had to be the same, but due to measurement inaccuracy, they were slightly different. By averaging them, the identification resistance error was smoothed. Fig. 28-1 shows the two voltage drops associated with the above described steps current. In order to determine the RC-branch parameters, that portion of the voltage-time evolution that held the information about the battery dynamic has been processed (Fig. 28-2).

Applying this procedure to the whole operational range of SoC, identification of electrical parameters of the improved SMHB model was developed for discharging and charging processes. The improvement introduced led to the modification of the parameters during the discharge phase., in particular for SoC values below 30%, as shown in the Table 5.

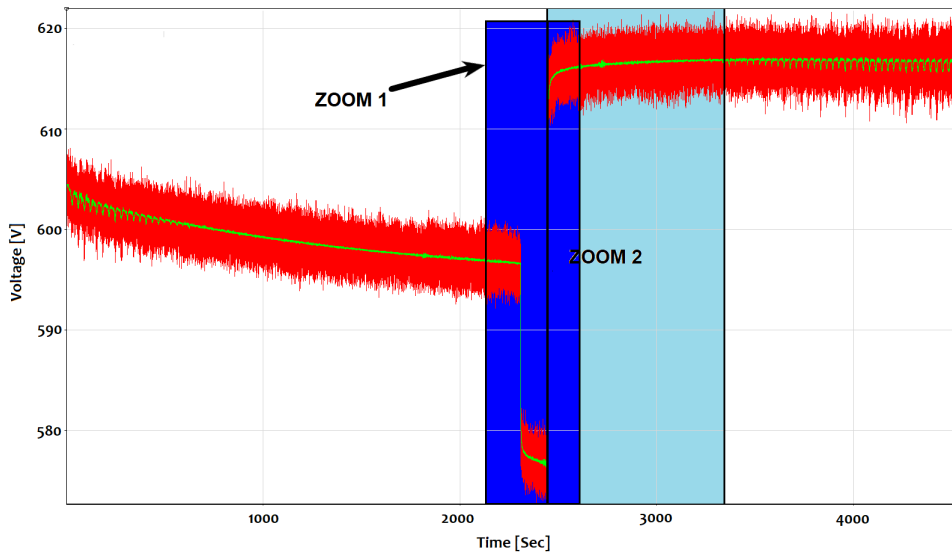


Figure 27: Details of the SMHB voltage evolution during discharging pulse test for SoC variation from 60% to 50%.

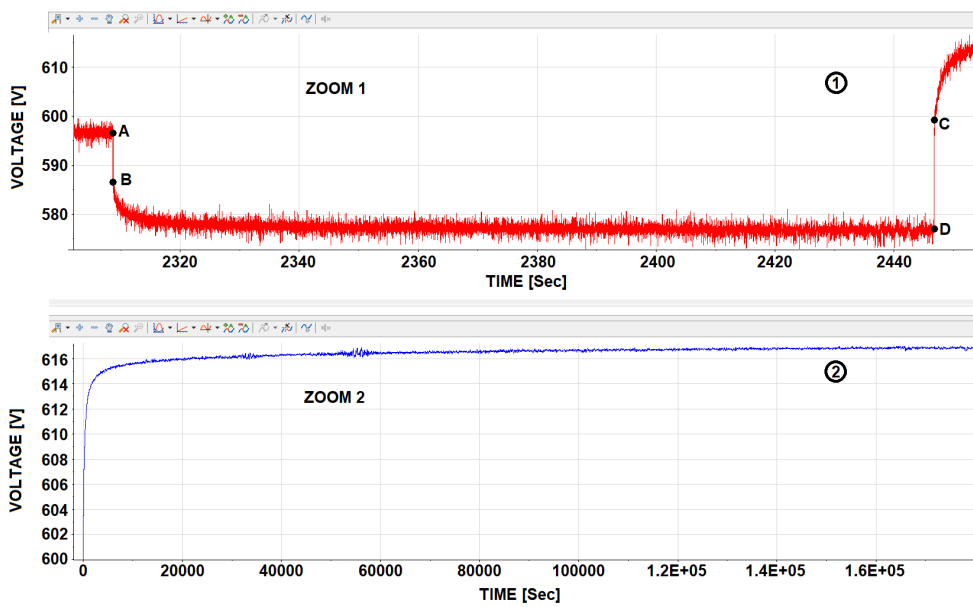


Figure 28: (1) Detail of the battery voltage variation corresponding to the current step. (2) Evolution of battery voltage during relaxation time.

SoC	OCV [V]	R_{Ni} [Ω]	R_{Fe} [Ω]	R_1 [Ω]	R_2 [Ω]	C_1 [F]	C_2 [F]
90%	617.9	2.4	-	0.0611	0.1233	1181.7	25.25
80%	617.7	2.55	-	0.0804	0.2759	952.74	6.071
70%	617.5	2.62	-	0.0979	0.5357	1570.5	3.6065
60%	617.3	2.65	-	0.1351	1.107	1221.3	1.7886
50%	616.8	2.66	-	0.1827	1.463	846.74	1.6261
40%	616.6	2.39	-	0.2216	2.521	1430.5	2.3937
30%	616.4	2.6	4	0.2743	4.024	2155.3	5.7033
20%	614.4	4.96	5	1	8	19.07	168.14
10%	576.7	6	6	1	8	4.9517	301.71

Table 5: Discharging circuital parameters of the improved SMHB model.

2.3.1 Experimental results of the improved model

The simulation results of the proposed SMHB model have been discussed and compared to the experimental ones in order to validate and evaluate its accuracy. Comparison with the simulated results of other models reported in the scientific literature is also presented. In particular, the following models were used:

CASE A: SMHB model without iron doping effects [41];

CASE B: SMHB model with iron doping effects considering a constant iron-voltage generator $OCV_{Fe} = 564V$ (section 2.2);

CASE C: improved SMHB model with iron doping effects and time variable voltage generator $V_{var}(t)$.

Fig. 29 shows the comparison between the experimental and simulated results, performed with the implementation of the models in Case A, B, and C, during a pulse test in the SoC range of 30% to 20%. Respective mismatching errors are reported in Fig. 30. The comparison highlights the improvements achieved by the use of iron doping in the Case B and C. However, Case B showed a voltage surge, absent in the experimental results, showing evidence of neglecting drift phenomena. Implementation of the variable voltage generator $V_{var}(t)$ in Case C, accounted for this phenomenon, highlighting the improvement.

In Fig. 31 and the same comparison among Case A, B, C and the experimental results were extended to the SoC range from 90% to 10% incorporating discharge pulse tests. Fig. 32 highlights the improvements obtained by the introduction of modelling of drift phenomena in Case C for an $SoC \leq 30\%$ versus Case B.

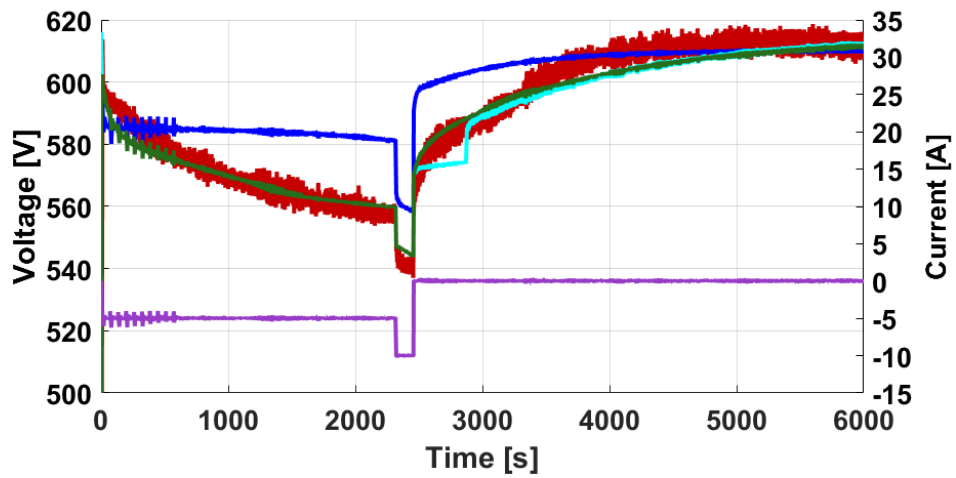


Figure 29: Comparison between experimental voltage evolution of the SMHB (red trace), and the simulated ones considering the models named Case A (blue trace), Case B (cyan trace) and Case C (green trace) during the discharging pulse test characterised by the application of the SMHB current (violet trace) and by variation of the SoC from 30% to 20%.

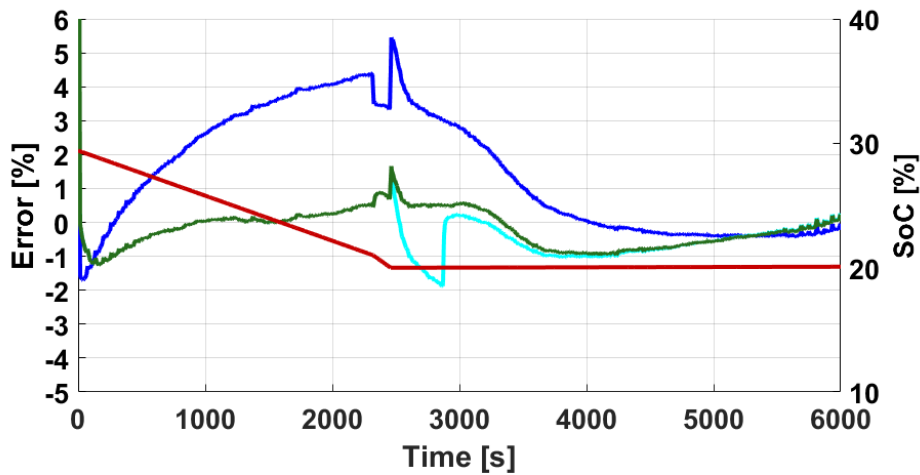


Figure 30: Time evolution of models mismatch errors for SoC variation from 30% to 20%. Time evolution of SoC (red trace), mismatch errors of the models named Case A (blue trace), Case B (cyan trace) and Case C (green trace).

In order to evaluate the model's behaviour during the charging/discharging transitions, a proper current profile was implemented on the SMHB. This profile was used to perform the simulation using the model associated with Cases B and C. In Fig. 33, comparison between the experimental voltage-time profile and the simulated ones in the critical SoC range of 40%-10% are reported. Analysis of the model mismatching errors in these two cases, compared to the experimental data reported in Fig. 34, underlines the improvements achieved by the proposed modelling. The error peaks when there is a zero-crossing of the current are related to the change in the value of the capacitors C_1 and C_2 .

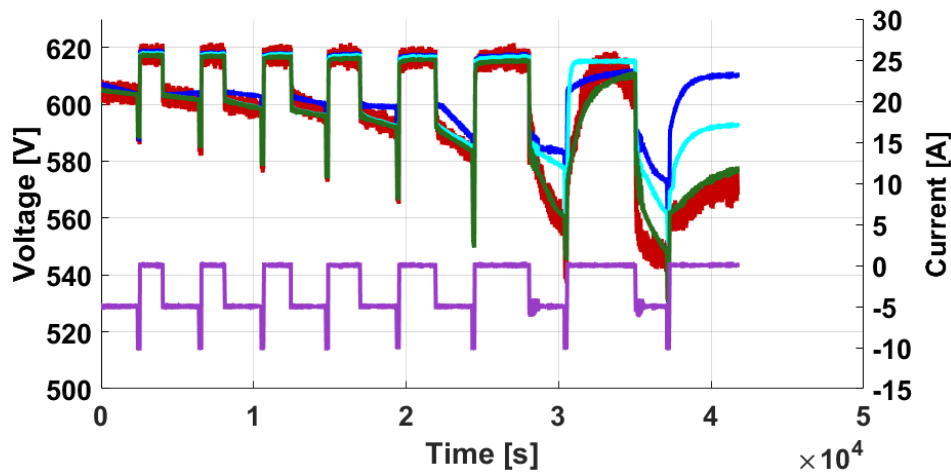


Figure 31: Comparison between experimental and simulated voltage evolution of the SMHB (red trace), for the models named Case A (blue trace), Case B (cyan trace) and Case C (green trace) during discharging pulse test characterised by the application of the SMHB current (violet trace) and by varying SoC from 90% to 10%.

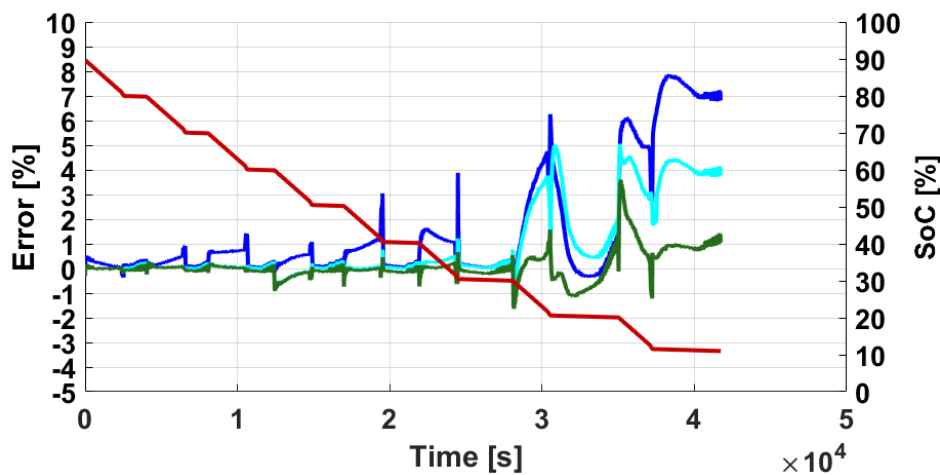


Figure 32: Time evolution of model mismatching errors for SoC varying from 90% to 10%. Time evolution of SoC (red trace), mismatching errors of the models named Case A (blue trace), Case B (cyan trace) and Case C (green trace).

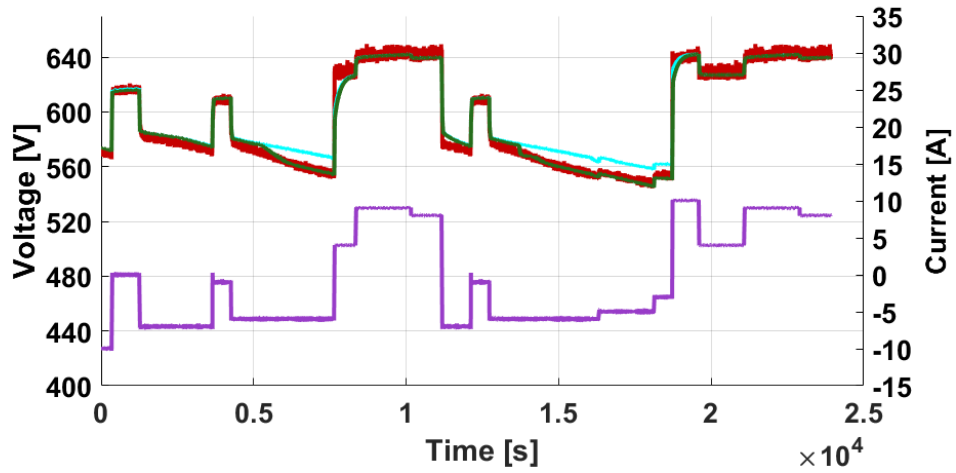


Figure 33: Comparison between experimental and simulated voltage evolution of the SMHB (red trace), for the models named Case B (cyan trace) and Case C (green trace) during the discharging/charging operative test characterised by the application of the SMHB current (violet trace) and by a varying SoC from 40% to 10%

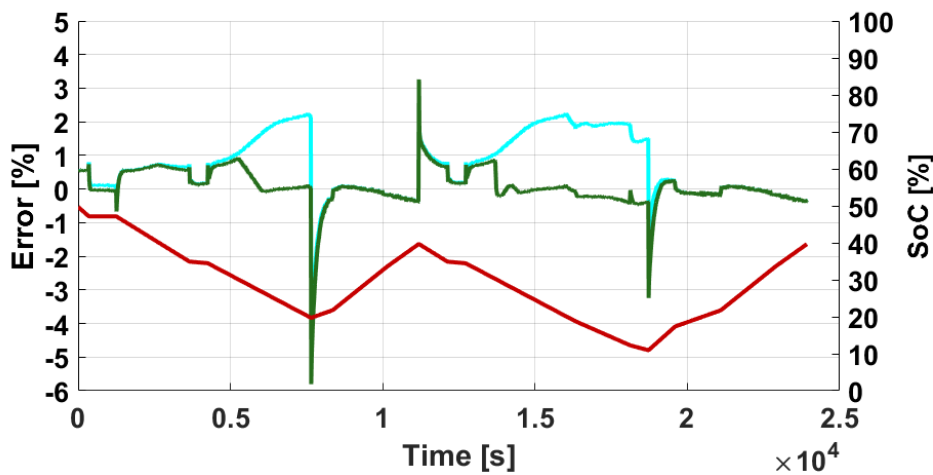


Figure 34: Time evolution of model mismatching errors for SoC varying from 40% to 10% during the discharging/charging operative test. Time evolution of SoC (red trace), mismatching errors of the models named Case B(cyan trace) and Case C (green trace).

Chapter 3

SMHB and DAB-DC/DC Converter Coupling

In the previous chapter, the development of an equivalent circuit model that describes the behaviour of the SMHB has been presented. This allowed extending the operating range of the battery. The proposed model can be fully exploited with the addition of external control to the battery, to ensure the required power evolutions. In order to reduce the ageing effect and to improve performances of the SMHB, specific power management of battery current and voltage is required in order to limit the stress on the electrochemical components. For this reason, a specific interface able to partially decouple the current and voltage evolutions on the SMHB from that applied on the DC-side of the grid-connected inverter is mandatory. This implies resorting to a specific DC/DC converter able to manage the current and voltage of SMHB according to its non-linear dynamic characteristics. Moreover, the DC/DC converter has to guarantee a bidirectional operation and high efficiency.

This chapter introduces the coupling between SMHB and a Dual Active Bridge (DAB) topology DC/DC converter. The design of standard and partial power DAB converter has been carried out referring to a commercial SMHB. At the aim of evaluating the advantages and the disadvantages of proposed E-ESSs configurations the simulations of both grid connected systems has been performed considering a SMHB model experimentally validated. The dynamic performances in different operative conditions of SMHB and the efficiency of the standard and partial power DAB has been compared. The simulation results have highlighted an improvement in the round-trip efficiency of the ESS implementing partial power DAB and good performances in managing the SMHB voltage variations in all operative conditions.

3.1 Dual Active Bridge Converter

Dual Active Bridge (DAB) converter is commonly found in different sectors such as in electric vehicles, in which DAB converters are used as battery charges [44, 45] or as active balancing systems [46]. The conventional DAB topology consists of two active bridges, a high-frequency transformer, and a series inductor. The main characteristics of the DAB are bi-directionality, galvanic isolation, high power density, and soft switching in some operating conditions. Additionally, in the state-of-art, a variant of the DAB without transformer can be found, for application in mobile phones and computer chargers [47]. Due to the symmetry of this converter, with identical primary and secondary, it is capable of bidirectional power flow control, and this is the reason why it has been selected to interface the SMHB with the grid. The topology is shown in Fig. 35, where V_{in} and V_{out} are the DC-link voltages, L_{leak} is the leakage inductance of the transformer, C_{1-2} are the DC-link capacitors and P_{1-4} and S_{1-4} are the controllable switches, on the primary and secondary sides respectively.

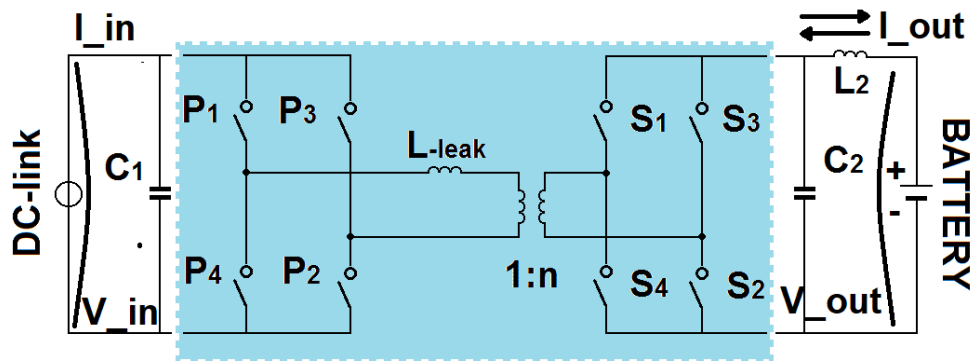


Figure 35: Standard DAB configuration.

The partial power DAB configuration has a similar structure from the topological point of view to the standard DAB, but the negative output pole is connected to the positive input one as shown in Fig. 36 and it is characterised by a rated power that is a fraction of the rated output power. This configuration makes it possible to modulate a lower voltage than that modulated with a standard DAB, ensuring benefits like better efficiency and lower hardware costs.

The power flow in the DAB can be directed by phasing the signals of one side with respect to the other. This form of control, called phase shift modulation (PSM), directs power between the two DC-buses in such a way that the main side supplies power to the delayed side [48]. This concept is illustrated in Fig. 37, where the applied square waves create a voltage differential across the transformer leakage inductance and direct its stored energy. Considering the control pulses for switches P_{1-4} of the primary side and S_{1-4} of the secondary

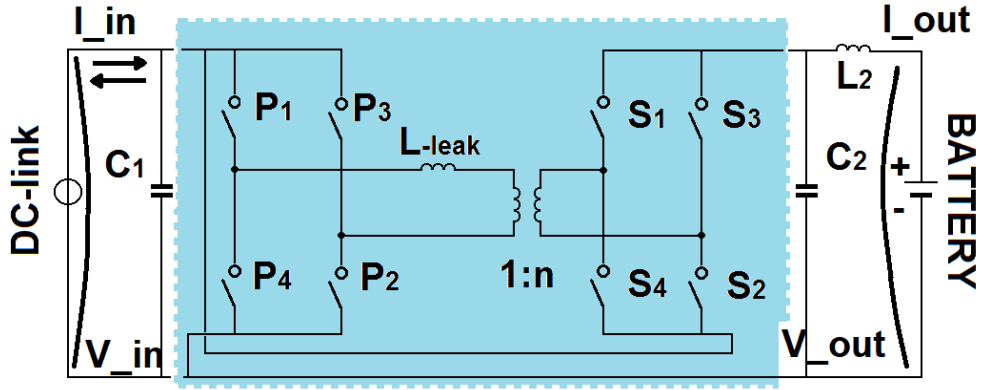


Figure 36: Partial-power DAB configuration.

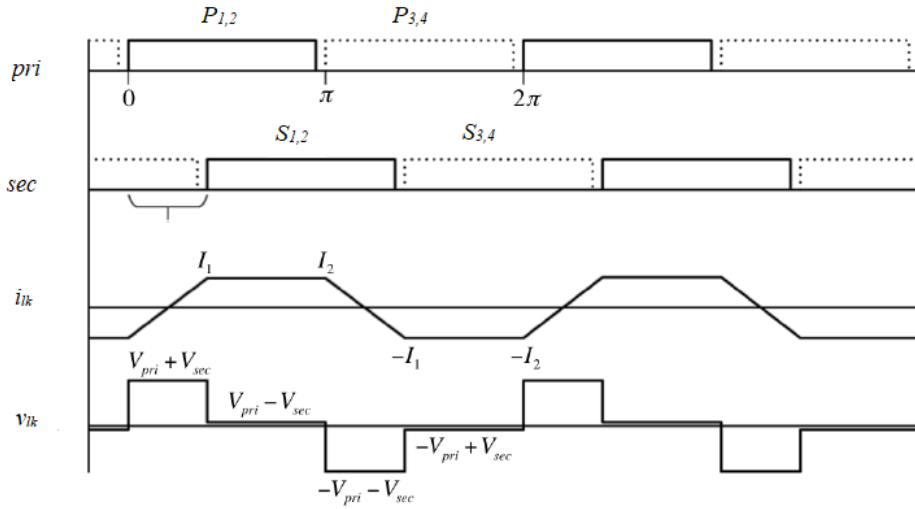


Figure 37: DAB phase shift modulation.

one, shifting the secondary side pulses by ϕ instantiates power delivery from the primary side to the secondary one. Similarly, shifting the secondary side by $-\phi$, making it the leading side, causes power to be delivered to the primary one. The symmetry of the current waveform i_{lk} through the leakage inductance allows for the following power flow analysis to be developed using a half switching period. The inductor current waveform can be expressed as:

$$\frac{di_{lk}(t)}{dt} = \frac{V_{pri}(t) - V_{sec}(t)}{L_k} \quad (18)$$

The output power can be express as:

$$P = V_{out}I_{out} = \frac{nV_{in}V_{out}}{2\pi^2 f_s L_k} \phi(\pi - \phi) \quad (19)$$

where n is the turn ratio of the transformer, and f_s is the switching frequency. This expression shows a relationship between the power delivered to the output as a function of the phase shift between the two bridges, the switching

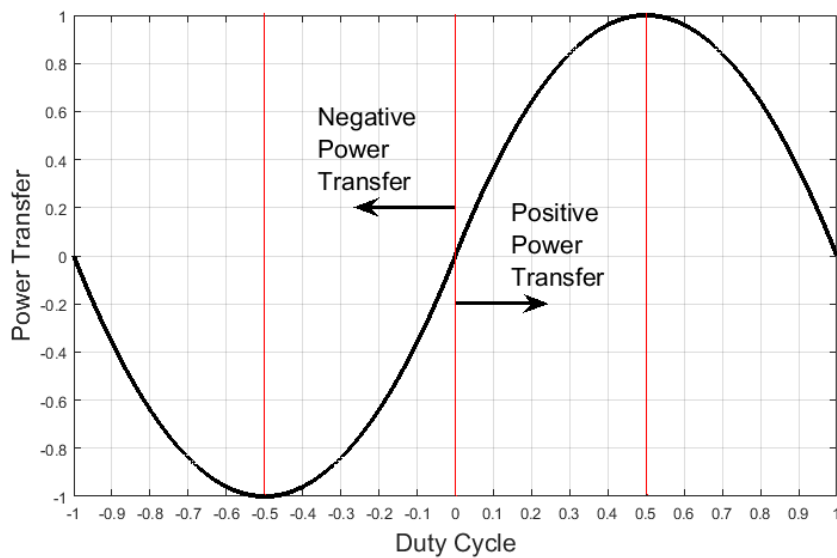


Figure 38: DAB power transfer as a function of duty cycle.

frequency of the converter, and the energy transfer inductance. Additionally, also indicates that a negative phase shift between bridges will cause power to be drawn from the output and delivered to the input DC-bus. Typically, the phase shift of the switches is indicated as a duty cycle, expressed as $D = \phi/\pi$. Fig. 38 shows the power transfer as a function of the duty cycle.

The control strategy is one of the important research directions for DAB. The different control methods are characterized by a different switch modulation. Different modulation strategies have been presented in technical literature for the current control in DAB converter [49, 50]. The most widely used control method for DAB is the Single Phase Shift (SPS) control. In SPS control, the cross-connected switch pairs in both full bridges are switched in turn to generate phase-shifted square waves with a 50% duty ratio to the transformer's primary and secondary sides. Only a phase-shift ratio can be controlled. By adjusting the phase-shift ratio between V_{pri} and V_{sec} , the voltage across the transformer's leakage inductor will change. Then, the power flow direction and magnitude can simply be controlled. The SPS control is attracting more and more attention due to its advantages, such as small inertia, high dynamic, and ease of realizing soft-switching control, and so on. For these reasons, the SPS modulation has been adopted to control the DAB converter.

3.2 DAB Configuration

To manage the DAB converter in its two configurations (Fig. 35 and Fig. 36), the SPS modulation has been adopted, characterised by the application of square-wave modulation signals at a fixed frequency. The current and voltage control has been performed by properly shifting the modulation square waves.

In order to calculate the mathematical law that governs the converter output current as a function of the phase shift between the switch in the primary and secondary side of partial-power DAB, ad-hoc tests were performed, according to the methodology described in [51]. In particular, a linear variation of the phase shift ϕ between $0-2\pi$ has been made, maintaining the output and input voltages constant. In this way, it is worth noting that the output current assumes a sinusoidal-type trend whose amplitude is linked to the input voltage. The law governing the output current with the phase shift can therefore be expressed as (20), where $f(V_{in})$ links the sinusoid peak to the input voltage.

$$I_{out} = f(V_{in}) * \sin(\phi) \quad (20)$$

In order to determine the trend of the function $f(V_{in})$, different tests have been performed whose results are shown in Fig.39. The first two tests keep the output voltage constant by varying the input voltage linearly, respectively with $\phi = \pi/2$ (red curve) and $\phi = 3\pi/2$ (purple curve). The other two tests keep the input voltage constant by varying the output voltage linearly, respectively with $\phi = \pi/2$ (blue curve) and $\phi = 3\pi/2$ (green curve).

These tests highlight that the DAB is particularly suitable for the SMHB. In fact, the current control by means of phase shift is decoupled from the battery voltage evolution. Referring to these results, two linear equations, expressed in (21), have been defined for control purposes. K^+ , K^- , C^+ , and C^- are constant values determined by a fitting procedure.

$$\begin{aligned} f(V_{in}) &= K^+ * \frac{V_{in}}{V_{max}} - C^+ & @\phi = \pi/2 \\ f(V_{in}) &= K^- * \frac{V_{in}}{V_{max}} - C^- & @\phi = 3\pi/2 \end{aligned} \quad (21)$$

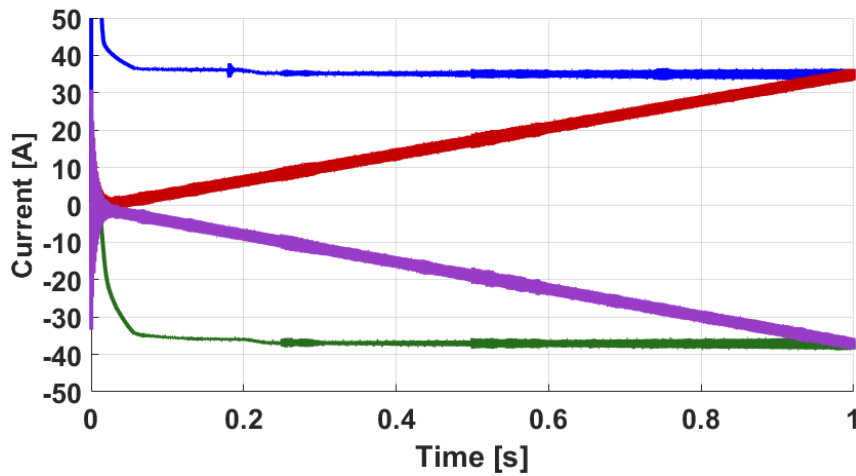


Figure 39: I_{out} time evolution. Constant V_{out} , variable V_{in} , $\Phi = \pi/2$ (red trace) and $\Phi = 3\pi/2$ (purple trace). Constant V_{in} , variable V_{out} , $\Phi = \pi/2$ (blue trace) and $\Phi = 3\pi/2$ (green trace).

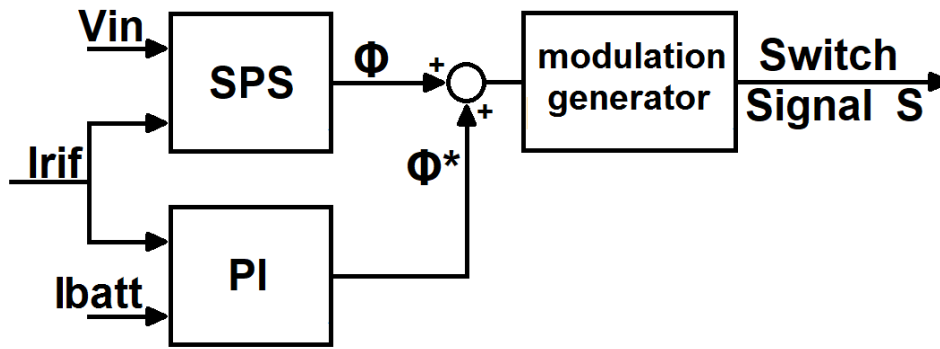


Figure 40: Current control block diagram.

The dependence of the output current by the output voltage can be considered negligible and hence has been omitted.

The combination of (20), (21) leads to (22) which connects the phase shift ϕ between switching signals in the primary and secondary side of the insulation transformer to both the output current and input voltage.

$$\phi = \arcsin \left(\frac{I_{out}}{f(V_{in})} \right) \quad (22)$$

Therefore, the DAB current loop control has been defined to impose the charge and discharge currents of the battery. In particular, Fig. 40 depicts the block diagram of the proposed current control. It was characterised by the definition of the phase shift angle between modulation signals of full bridges of DAB resorting to the combination of a feed-forward action, performed according to 22, and of a feedback action, obtained by means of PI current regulator. In particular, the SPS block evaluates the feed-forward value of ϕ using the information of the battery voltage estimated by the model of SMHB and the current set-point. This value is then adjusted by the PI block in order to obtain a more precise output current. Finally, the modulation generator block generates the signals to be sent directly to the converter's switches. The proposed current control strategy has been implemented in standard and partial power DAB.

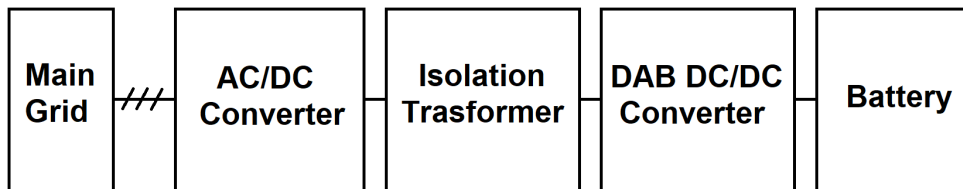


Figure 41: Block diagram of the proposed structure.

With the aim of implementing the SMHB within an electrical network as a support to the network, the proposed schematic structure is shown in the block

Parameter	Symbol	Value	Unit
Collector-emitter voltage	V_{CE}	650	V
DC collector current (100°C)	I_C	50	A
Pulsed collector current	I_{Cpuls}	150	A
Gate-emitter voltage	V_{GE}	± 20	V
Turn-on resistance	R_{on}	14	m ω

Table 6: Characteristics of IGBT IHW50N65R5.

Parameter	Symbol	Value	Unit
Maximum power	P_{max}	12	kW
Input voltage	V_{in}	500	V
Output voltage	V_{out}	600	V
Leakage inductance	L_{lk}	300	μ H
Efficiency	η	99.2	%

Table 7: Characteristics of high-frequency transformer.

diagram of Fig. 41. The DAB DC/DC converter is used to connect the SMHB to the DC side of an AC/DC converter. The DAB converter has the purpose of managing the current on the SMHB according to the constraints imposed by the BMS and with the aim of extending the operative SoC of SMHB.

The design of DAB has been developed referring to a rated power of 10kW and input voltage V_{in} of 500V and a battery rated voltage V_{out} of 620V. In particular, the full bridges implement IGBTs whose characteristics are reported in Table 6. The choice of IGBTs has been made as they are typically used in applications characterized by high voltages and with output powers greater than 5 kW. They are also used with low switching frequencies (below 100 kHz). As a transformer for the DAB, a high-frequency ferrite transformer was chosen, the characteristics of which are shown in Table 7.

The transformation ratio of the high-frequency transformer has been set to 1:1. The switching frequency (f_{SW}) has been set to 20 kHz. The DAB is completed by filters on the input and output sides. For sake of completeness, the DAB has been connected to the main grid characterised by a rated voltage of 400V and a frequency of 50Hz by means of an ideal three-phase DC/AC converter connected to an isolation transformer. In order to perform a correct comparison between the standard and partial power DAB configurations, the design partial power DAB has been developed considering exactly the same components of the standard one. The only difference is in the transformation

ratio of the high-frequency transformer that has been set in partial power DAB at 1:3.

3.3 Simulation and results

In order to evaluate the performance of the proposed structure, an extensive simulation in Matlab/Simulink environment has been developed. The same battery current set points have been imposed considering both standard and partial power DAB configuration, in order to compare coherently the results. Specific tests, aimed to evaluate the proposed control and design of the DC/DC converters, have been developed. Short duration simulations (two seconds) with continuous variations in the reference current of the battery have been carried out. This approach allows the evaluation of dynamic performances of current control and the comparison of current and voltage evolution of the two DAB configurations under test.

Specific evaluation on the DC/DC converter in both standard and partial-power configuration has been performed in order to evaluate the efficiency η during both in discharge and charge phases according to equations 23 [52].

$$\eta = \frac{P_{batt}}{P_{batt} + P_T} \quad (23)$$

$$P_T = I_{SRMS}^2 * R_s + \frac{1}{2} * I_p * V_x * t_c * f_{SW} + I_{LRMS}^2 * R_L + P_{core}$$

where

$I_{SRMS}^2 * R_s$	conduction switch losses
$\frac{1}{2} * I_p * V_x * t_c * f_{SW}$	switching losses
$I_{LRMS}^2 * R_L + P_{core}$	transformer losses

In the efficiency evaluation the switching losses are negligible [53], hence have been omitted. In this way, it has been possible to determine the whole efficiency of the system composed of the DAB converter and the SMHB, by a long duration simulation (six hours), taking into account the converter's losses by considering the efficiency according to (24).

$$\begin{aligned} P_{in} &= P_{batt} * \eta & P_{batt} > 0 & \text{Discharge} \\ P_{in} &= \frac{P_{batt}}{\eta} & P_{batt} < 0 & \text{Charge} \end{aligned} \quad (24)$$

The tests have been aimed at verifying the correct functioning of the two DAB configurations. In particular, tests have been carried out by setting a variable power request at the output of the battery-DAB system, keeping the voltage output constant at 500 V. The evaluation has been made by comparing

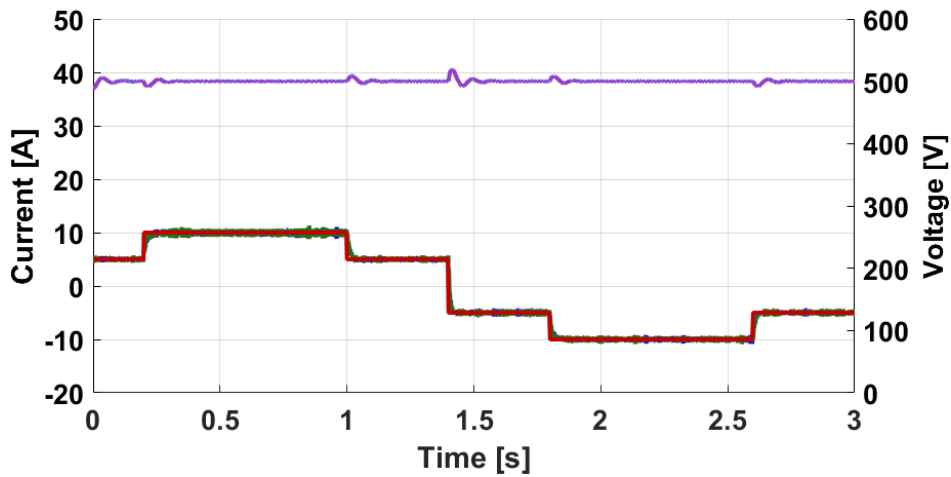


Figure 42: Comparison between simulated battery current evolution at 50% of SoC (green curve), at 20% (blue curve), and reference current (red curve) for standard DAB converter. DC-link simulated Voltage evolution at 50% of SoC (purple curve) and at 20% (cyan curve).

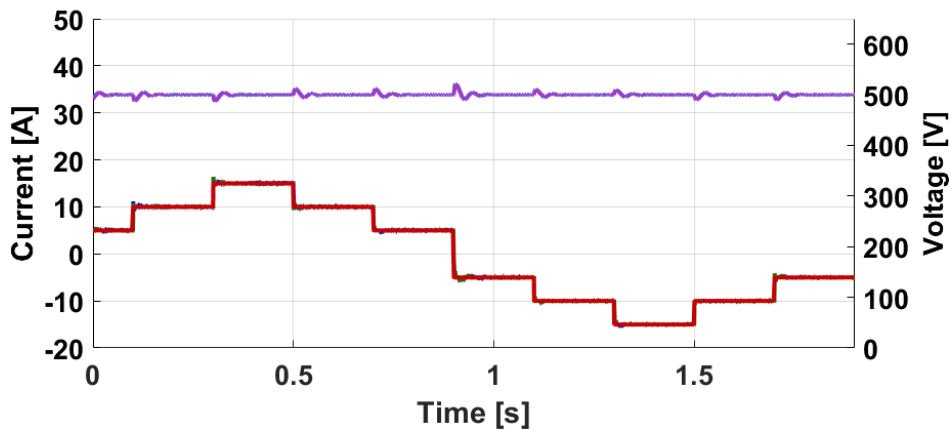


Figure 43: Comparison between simulated battery current evolution at 50% of SoC (green curve), at 20% (blue curve), and reference current (red curve) for partial DAB converter. DC-link simulated Voltage evolution at 50% of SoC (purple curve) and at 20% (cyan curve).

the behaviour of the two DAB configurations with an SoC value battery at 50% and 20%.

In Fig. 42 the simulation results of the tests performed on the standard DAB, are shown. In particular, the comparison between the battery current evolutions at 50% of SoC (green curve) and at 20% of SoC (blue curve), respect to the reference current (red curve), is depicted. The three current evolutions overlap, suggesting that SMHB's SoC differences do not affect the handling of the DAB converter in response to the demand for power. Furthermore, the voltage-time evolution of the DC-link (purple and cyan curve) appears constant and equal to the value of 500V for both SoC situations. In Fig. 43 the

simulation results relative to the same tests on the partial DAB configuration are shown.

The simulated currents follow the reference current with good matching in correspondence with both 50% and 20% SoC values and with two proposed configurations taken into consideration. Similarly, the voltage on the DC-link remains correctly constant and equal to 500 V except for small transients in correspondence with the current variation, proving that the converter works properly.

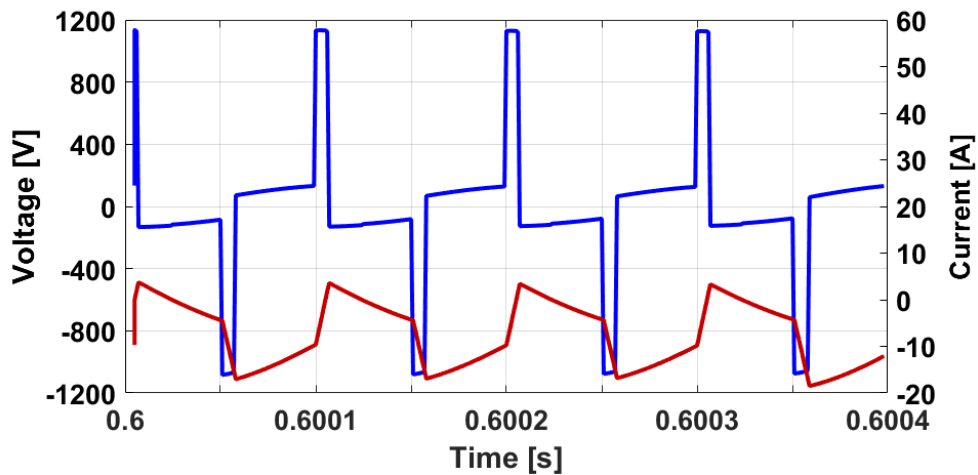


Figure 44: Voltage (blue curve) and current (red curve) evolutions into the transformer leakage inductance in the standard DAB configuration.

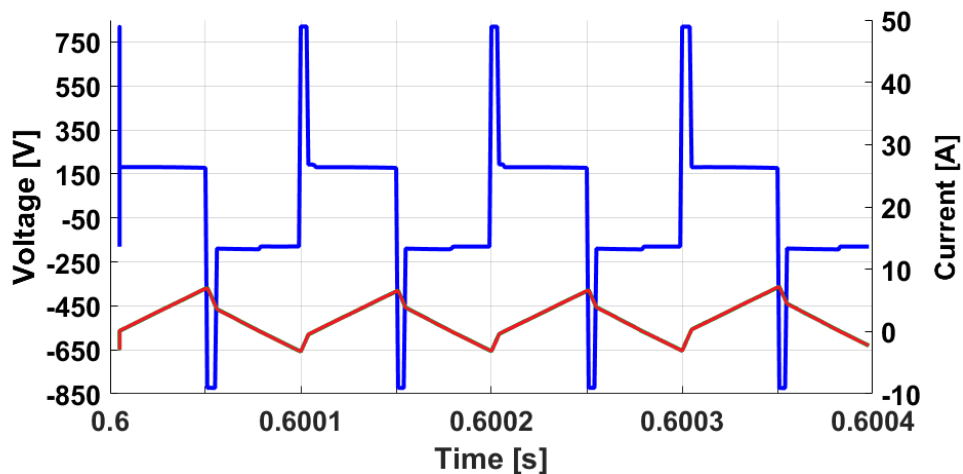


Figure 45: Voltage (blue curve) and current (red curve) evolutions into the transformer leakage inductance in the partial DAB configuration.

In order to highlight the difference between the two converter configurations, the voltage and current evolutions that flowed into the transformer have been reported. In particular, Fig. 44 and Fig. 45 show the voltage (blue curve) and

the current (red curve) evolutions in the transformer leakage inductance of the standard DAB and partial one.

The simulation results highlight that the voltage evolution in the transformer of the standard DAB configuration is higher than that partial one due to the different transformation ratios used. Fig. 46 and Fig. 47 show the voltage evolutions in the two converter configurations in the primary (blue curve) and secondary (green curve) side, during a battery charging phase.

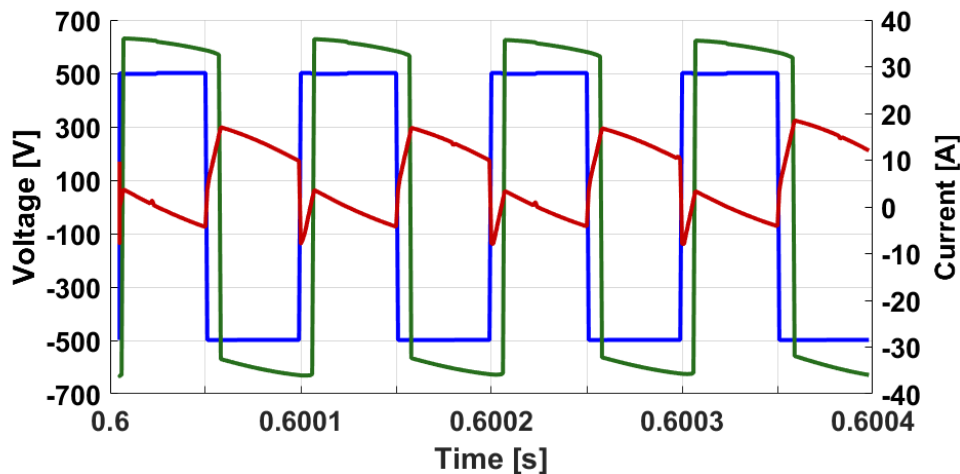


Figure 46: Voltage in the primary side (blue curve) and secondary side (green curve) evolutions in standard DAB converter. The red curve is the output current of the converter in a battery charge phase.

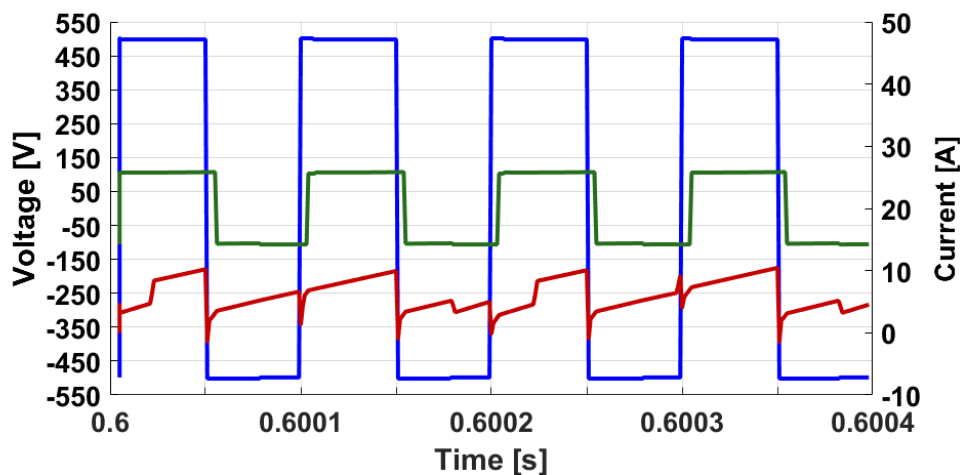


Figure 47: Voltage in the primary side (blue curve) and secondary side (green curve) evolutions in partial DAB converter. The red curve is the output current of the converter in a battery charge phase.

In order to evaluate the efficiency as a function of the required power, appropriate investigations have been carried out. Introducing variations in the model of the converter used, considering the (23), efficiency table shown in

Power [W]	η_{std} [%]	η_{part} [%]
-6000	98.65	98.16
-3000	97.59	96.63
3000	92.78	95.97
6000	94.86	98.37

Table 8: DAB converter efficiency of both standard and partial configuration.

Table 8 both for the standard configuration and for the partial configuration has been calculated. This analysis highlights how the DAB partial has improved efficiencies when the power flows from DC-link to the battery compared to the standard configuration, while during the reverse flow, the efficiencies are similar.

Applying the DAB converter efficiency on SMHB model, the whole system efficiency has been evaluated during the charge and discharge phases. In particular, charging the battery from 10% to 90% of SoC, 20.82 kWh of energy have been absorbed from the DC-link and just 19.67 kWh have been delivered to the battery for the standard DAB configuration. Similarly, during the discharge phase from 90% to 10% of the SoC, 19.74 kWh of energy has been absorbed by the battery and only 19.43 kWh has been delivered to the DC-link. Thus, the charge and discharge efficiency for the standard DAB configuration is 94.47% and 98.43% respectively. By applying the same output current evolutions to the partial configuration, it has been possible to determine that during the charging process 20.82 kWh have been absorbed from the DC-link and just 20.38 kWh have been delivered to the battery. During the discharging phase, 19.74 kWh have been absorbed from the battery and just 19.31 kWh have been delivered to the DC-link. The efficiencies in the charge and discharge phase for the partial DAB configuration are 97.88% and 97.82% respectively.

In order to evaluate the round trip efficiency for the battery-DAB system, a complete charging and discharging procedure have been executed. In particular, the power absorbed by the network to charge the battery from 10% to 90% has been evaluated, and subsequently the power that the battery has been able to supply to the DC-link before reaching again the value of 10% of SoC. Fig. 48 and Fig. 49 show the simulation results referring to the standard and partial DAB respectively. In both the configuration presented, during the charge phase, the power absorbed from the DC-link (green curve) is higher than that delivered to the battery (blue curve), while during the discharge phase, the power absorbed from the battery is higher than the one delivered to the DC-link.

Analysing the individual configurations, it is clear how the partial configuration has the best efficiencies, shown in the Table 9. In fact, considering the standard DAB, 20.83 kWh have been absorbed from the DC-link and just

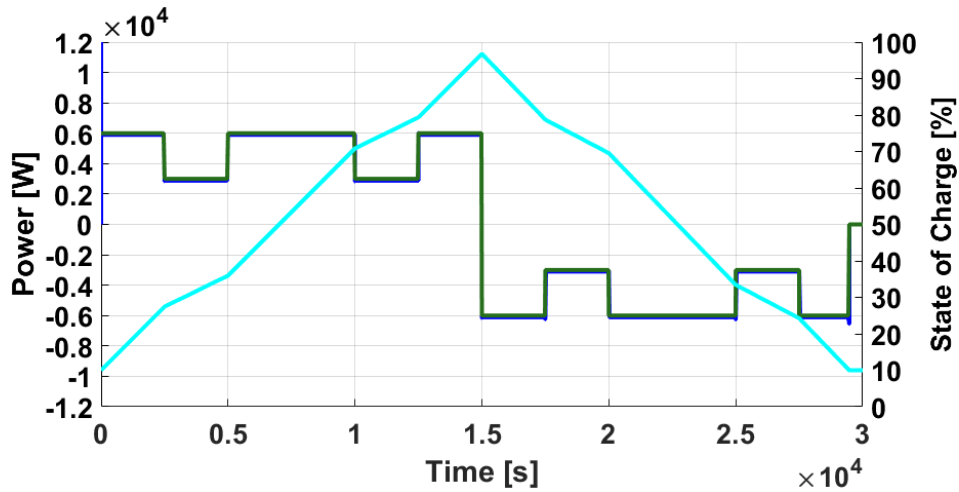


Figure 48: Comparison between power absorbed/supplied by the DAB (green curve) and supplied/absorbed by the battery (blue curve) with the battery SoC evolution (cyan curve) for the standard DAB configuration.

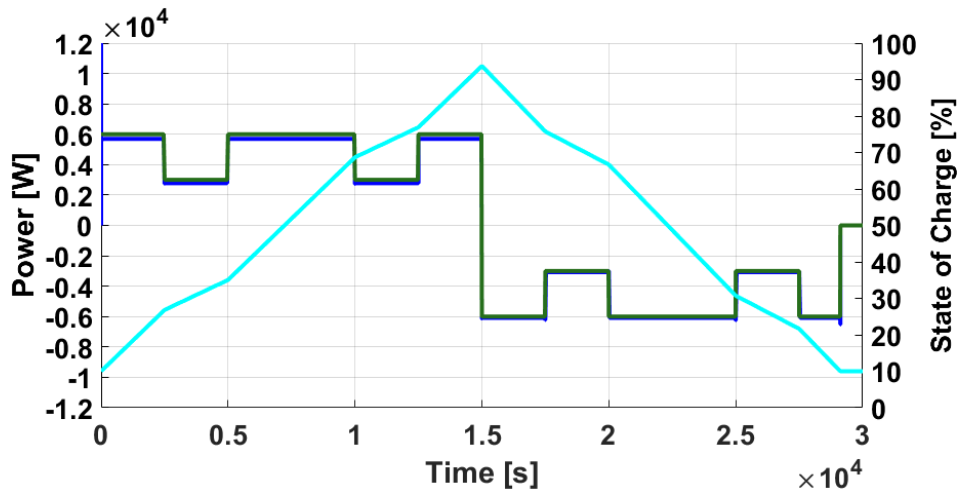


Figure 49: Comparison between power absorbed/supplied by the DAB (green curve) and supplied/absorbed by the battery (blue curve) with the battery SoC evolution (cyan curve) for the partial-power DAB configuration.

	E_{adsorb} [kWh]	E_{deliv} [kWh]	η [%]
Standard DAB	20.83	19.32	92.9
Partial DAB	20.83	19.96	95.8

Table 9: Round trip efficiency of both standard and partial DAB configuration.

19.32 kWh are returned to it, so the round trip efficiency is 92.9%. Otherwise, considering the partial configuration, 20.83 kWh have been absorbed from the DC-link and 19.96 kWh are delivered to it, so the round trip efficiency is equal to 95.8%.

In conclusion, from an energy point of view, the comparison between the two proposed system configurations has highlighted the better performance of the configuration implementing a partial DAB converter with respect to the standard one. Moreover, when the same evolution on the power system has been imposed, the round trip efficiency of a system implementing the partial DAB converter presents performances that are 3% higher than the standard DAB. However, the analysis of voltage and current evolutions in partial DAB has highlighted critical issues that require further research activities that will be developed in future works.

Chapter 4

Second Life Batteries

The ever-increasing need to reduce CO₂ emissions related to the public transport sector is driving more and more growth in the number of electric vehicles (EVs) in circulation. The large-scale implementation of EVs may cause a reduction of the stability and power quality of the electricity grid if charging events will be uncontrolled. A solution to these issues can be found in the implementation of a smart grid fusing renewable energy sources (RES) and stationary energy storage systems (ESSs) to support EVs charging [54]. However, the high cost of batteries (\$ 200-500/kWh) represents a significant part of the initial investment cost that may limit the widespread adoption of micro-grid systems [55]. A reduction of the investment costs can be provided by the adoption of second-life battery packs (SLBs) [56, 57]. In fact, EV batteries that have lost as little as 20% of their initial capacity are often withdrawn from application and sent to battery recycling plants. Such batteries would still be able to provide services for stationary applications [58], minimizing the environmental impacted cost of recycling.

Among the applications that are attracting the most interest in the use of battery packs composed of SLBs, it is possible to find frequency regulation and DC fast-charging stations (DCFC), the latter directly connected with the increase in the number of EVs. However, several issues need to be solved before the wide adoption of SLBs, especially the development of algorithms capable of accurately estimating the remaining useful life (RUL) without extensive laboratory testing.

In this chapter, a general methodology for analysing the power profiles associated with SLB applications, such as frequency regulation and DCFC is proposed. The study then focused on the example of DCFC, developing several power profiles and investigating the impact of degradation and replacement rate for a specific system design. As SLBs, lithium-ion batteries withdrawn from EV application have been considered. Using an empirical aging model, degradation effects such as calendar and cyclic effects, have been studied based on the different power profiles. A correlation between the power profiles and the aging stress factors has been evaluated. Finally, a comparison between SLB lithium-ion and SMHB for DCFC application has been made.

4.1 Power Profiles for Second Life Batteries

Batteries have the potential to improve grid reliability, power quality, efficiency, flexibility, provide ancillary services to the grid, support RES, and delay system expansion/investment. In the field of stationary applications, there are many opportunities for use for SLBs, since they provide a low-cost solution for stationary ESSs, such as peak shaving, area regulation, self-consumption, and frequency regulation [59].

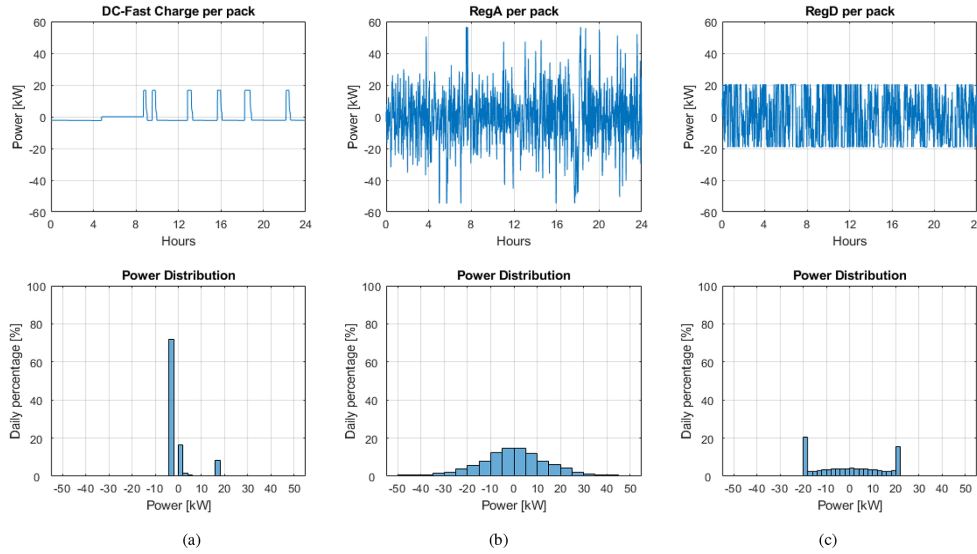
In peak shaving applications, the accumulated energy during off-peak periods can be used to respond to peak demand periods. A typical peak shaving application is DC fast charging (DCFC) of EVs in which the load on the power grid can be reduced through the use of stationary battery packs [60]. With the increase in the number of EVs in circulation, more and more DCFC stations may be required, and SLBs represent an interesting business opportunity to enable the integration of ESSs in DCFC with the aim of developing more grid-friendly stations.

The typical DCFC profile may request a peak power on the order of kW (generally between 50-300 kW). Fig. 50(a) shows an SLB power profile for a DCFC station application. SLBs from the Ford Focus EV 2011 model have been considered, which characteristics are shown in Table 10. The profile consists

SLB chemistry	NMC-LMO Li-ion
SLB Nominal Capacity	73.5 Ah
SLB State of Health (SoH)	90%
Energy Battery	23 kWh
Operating Voltage	260 V to 360 V
Operating Temperature	-10°C to 45°C
SoC Operating Range	10%-90%
Continuous Power Limit	(60 kW, 110 kW) for SoC=5-95%

Table 10: SLB parameters considering a Ford Focus EV [61].

of intermittent discharge pulses with a duration of 5-30 minutes. Depending on the number of EVs charge request per day, the number of daily pulses and their duration is different. Each DCFC pulse consists of a constant current and constant voltage section [62]. In the absence of request of DCFC events, the station charges the SLBs through the grid connection, with constant low power (e.g. 7 kW) to ensure that the daily net energy flow through the batteries is quasi-zero. The DCFC power profile has been obtained using the probability distribution function reported in [63, 64]. In detail, the power profile has been normalized considering the fleet of EVs, the power capacity, and the operating time range. The profile has been then converted from average power per hour to operating time. In this way, a normal probability function is used to create



DC FAST CHARGING	REG. A	REG. D
System power demand 50 kW	System power demand ± 1 MW	System power demand ± 1 MW
Pulse duration ~ 5-30 minutes	Pulse duration ~ 2-5 seconds	Pulse duration ~ 2 seconds – 3 minutes
Intermittent pulses with rest time	Low-amplitude high-frequency dynamic	High-amplitude high-frequency dynamic
Variation in duration and timing of peak power events for each day	Primary frequency control profile (slow dynamic)	Primary frequency control profile (fast dynamic)
Critical limit = 3 batteries	Critical limit = 18 batteries	Critical limit = 49 batteries

Figure 50: Daily power profile and power distribution of: (a) DCFC; (b) RegA; (c) RegD. The battery pack profile has been achieved by considering the battery pack specifications reported in Table . Note, positive power represents discharge.

a time-based profile with a peak of 50 kW per station. To ensure the random distribution of EVs power requests during the day, the start of the probability of the power pulse has been defined within a three-hour bandwidth. Finally, the charging phase of the station has been added considering a 7 kW connection to the grid to ensure zero net energy in a day.

For frequency regulation, two different types of power profiles have been analysed based on the PJM Regulation Market (regional transmission organization in the United States). One kind of power profile, called RegA, is a traditional, slow-moving signal best used for generators due to their slower ramp rates. The second power profile, called RegD, is a quick-moving signal best suited for energy storage due to its fast ramp rates [65]. Fig. 50(b) and 50(c) show example SLBs power profiles for RegA and RegD applications, where it is important to note the dynamic behaviour of the RegD signal compared to the RegA signal. Both systems have been designed considering a capability of ± 1 MW. However, the number of batteries required to fulfil the RegD profile is much larger (49 SLBs) than the RegA profile (18 SLBs), so the power request is scaled down considering these design specifications. RegA and RegD are characterised by a different revenue based on the movement (mileage) of the signal [66]. Since it is very favourable for the electric grid to have fast-responding

frequency regulation resources, PJM has implemented a payment system that compensates RegD signals more than RegA [67].

4.1.1 Definition of the Metrics

From an initial analysis of Fig. 50, it is possible to point out how the different profiles affect the system design (number of SLBs), moreover, it is possible to identify specific characteristics for the different applications. This work proposes a statistical analysis of the SLB profiles with the aim of identifying specific metrics for each application. Similar analyses have been reported in the literature for other applications, as for example in [68] a methodology for analysing real-world driving cycles was developed and used to build new driving cycles without losing the specifications of a vehicular application. Nine statistical metrics have been defined for the SLB application:

- **Power distribution:** distribution of occurrence of the battery power;
- **Mean:** daily average of the power, in kW;
- **RMS:** root mean square value of the daily power, in kW;
- **Derivative:** t what speed the daily power changes, in kW/s;
- **Mean of the derivative:** (for positive and negative power) in kW/s;
- **Peak of the derivative:** (for positive and negative power) in kW/s;
- **Energy:** the amount of energy stored or extracted daily, in MJ;
- **Mileage:** daily movement of the power, in MW;
- **FFT:** Fourier analysis of the power profile.

All these metrics have been analysed considering the power request to each SLB for the specified applications, as shown in Table 11. The power distribution metric reports the probability that the power request will be in a specific power range over a day period. In the case of the DCFC (Fig. 50(a)), 72% of the time is spent charging the SLBs (7 kW/3 batteries), while the DCFC events represent 12% of the total profile (50 kW/3 batteries), then the SLBs are 16% of the time in rest. Regarding frequency regulation, RegA distribution (Figure 50(b)) shows a Gaussian distribution, with a zero mean. RegD distribution (Fig. 50(c)) instead can be represented by a Gaussian with a superimposed U-shape distribution. It is possible to notice that RegD requires the batteries to operate for a long time at high power when compared to RegA.

The results show that the mean power, for all profiles, is close to zero. This demonstrates how all the profiles during the day have quasi-zero net energy.

	Profile	DCFC	RegA	RegD
Mean [kW]		-0.06	-0.20	-0.15
RMS [kW]		5.3	16.56	14.33
Derivative	positive mean [kW/s]	0.001	0.11	0.091
	positive peak [kW/s]	17.74	29.37	2.46
	negative mean [kW/s]	-0.001	-0.11	-0.09
	negative peak [kW/s]	-4.26	-22.72	-4.01
Energy (charge) [MJ]		-140.29	-543.46	-551.06
Energy (discharge) [MJ]		134.69	525.7	537.4
Total Energy [MJ]		-5.6	-17.76	-13.66
Mileage [MW]		0.08	18.22	15.73

Table 11: Results of all metrics for each profile applied to a typical day.

However, daily SoC gain/loss can be observed due to the non-zero total energy. This is very typical for several grid-connected applications.

The RMS value shows how the two frequency regulation profiles have higher power requests. RegD has an RMS value very close to that of RegA, but the number of batteries is very different. This is consistent with the fact that in RegD the power is held at high values for most of the time and requires a system with high energy capacity to fulfil the mission profile.

The derivative metric allows analysing how fast the power changes for the different profiles. Due to the battery size difference, the RegD and RegA mean derivative values are quite similar to each other, when in reality at the system level the RegD mean derivative would be greater than RegA because of its more dynamic profile. The derivative peak values for RegA and RegD also differ by a significant amount, but this is mostly because of outlier values in the RegA profile that give it very high peak values. For the DCFC application, the power profile has very little movement, keeping the mean derivative values low, but incorporates quick power spikes to provide the DCFC, allowing for high positive and negative derivative peaks.

Another way to investigate the power profiles is by using the mileage metric. The mileage is defined as the total movement requested by the frequency regulation control signal (here it is applied to DCFC as well), as shown in the following equation (25):

$$Mileage = \sum_i^N P_i - P_{i-1} \quad (25)$$

where P is the SLB power at a discrete-time i . The mileage can help determine how quickly and often a signal changes (the movement) since it tracks the power differential of the signal. This supports the analysis reported by the

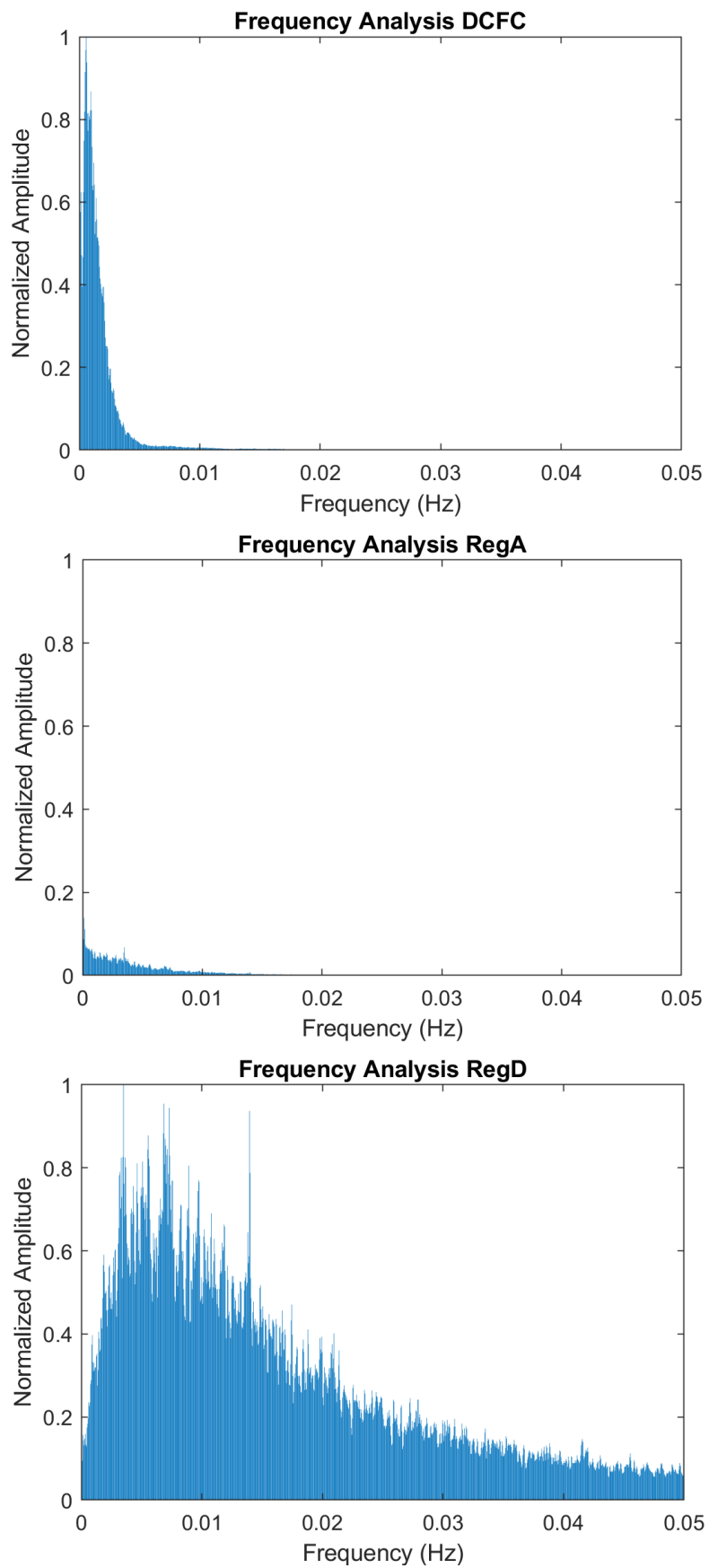


Figure 51: FFT analysis results for the SLB applications.

derivative metrics. In fact, the DCFC has a very low mileage due to its low power profile movement, and RegA and RegD take on similar mileage values because of the battery size difference. As with the derivative mean values, the RegD profile normally has a much higher mileage at the system level than RegA. Note that the mileage of several profiles can be compared only if the signals have the same time resolution and the calculation is performed on the same timespan.

Finally, the FFT analysis for DCFC, RegA, and RegD signals is reported in Fig. 51. Welch's Method has been used to help reduce the amount of noise in the frequency analysis, in detail data from 4 months with a window length of two days and Hamming Window has been applied to each of these segments. The DCFC frequency analysis involves a short bandwidth of low-frequency components, representing the periodicity of the DCFC pulses each hour. RegA signal is characterised by high magnitude, low-frequency components, while RegD has a much larger bandwidth and higher frequency components. This finding is in line with the nature of the two signals, as matter of fact, the analysis is showing the sporadic, fast-moving signal pace of RegD compared to the more periodic, stable RegA signal.

4.2 Battery and Aging Model for Lithium-ion

After analysing the SLBs power profiles for the three different applications, the study focused on the DCFC profiles. Starting from the power profiles, and considering in particular, the SoC trend, the goal was to identify parameters that allow estimating the effects of battery aging for this specific application. Previous studies performed by the authors [60, 64] show that SoC-driven calendar aging is the predominant aging effect for this application. In fact, the current level and temperature effects can be ignored due to the fact that SLBs have been initially designed for a more demanding power application (automotive). The battery pack considered in this analysis consists of n-SLBs that operate in parallel in order to reduce ohmic losses. In the analysis, it was considered that each battery had the same electrical, thermal, and chemical characteristics [69]. The parameters of the SLBs are reported in Table 10 and represent the characteristics of the battery pack of a Ford Focus EV 2011. The size of the system is n=3 batteries. The State of Health (SoH) has been set to 90% indicating the wear due to the automotive life. Note that usually traction batteries are dismissed from the automotive application when they reach SoH=80%, however, due to the lack of experimental data for low SoH, this analysis considers initial SoH=90% and a time-frame of 3 years.

To describe the behaviour of the batteries, a zero-order equivalent circuit model has been used [70], described by the following equations:

$$I_{SLB} = \frac{V_{OC} - \sqrt{V_{OC}^2 - 4 * R_{SLB} * P_{SLB}}}{2 * R_{SLB}} \quad (26)$$

$$V_{SLB} = V_{OC}(SoC) - I_{SLB} * R_{SLB} \quad (27)$$

$$SoC(t) = SoC_0 - \frac{1}{C_{SLB}(t)} * \int_0^t I_{SLB} dt \quad (28)$$

where, I_{SLB} = current flowing in the battery pack; V_{OC} = open-circuit voltage (function of SoC); R_{SLB} = internal resistance of the battery pack (function of SoC, temperature and c-rate); P_{SLB} = power of the battery pack; V_{SLB} = voltage of the battery pack; SoC_0 = initial SoC; C_{SLB} = capacity of the battery pack. The temperature of the SLBs is considered constant and a thermal model is not included in this analysis.

In general, the degradation phenomena of Li-Ion batteries are mainly due to exposure to extreme temperatures (high/low), high SoC values, high charging voltage, time of use, and number and depth of charge/discharge cycles. Considering the single cell, the main effects that can be identified at the output terminals are the loss of cell capacity (capacity fade) and the increase in internal resistance, which results in a reduction in power (power fade) [71].

The degradation mechanisms of lithium ions have been extensively studied in the literature to improve materials, model the underlying mechanisms and reduce aging kinetics. Understanding the evolution of battery pack performance over various time scales (days, months, years, etc.) is essential for discovering strategies to make the system work efficiently. Knowledge of aging mechanisms at different length scales, such as at the electrode or cell/module or system level, provides valuable insight into strategies in battery design, thermal management and charge control. With the increasing number of retired traction battery packs, extending battery life, albeit in an alternative application, would increase the economic value of the pack and open up new second-life market opportunities. An important piece of the puzzle involves predicting the health of the battery when used for a specific second life use. For this purpose, one can choose from a wide range of aging models, ranging from physics-based models to semi-empirical models to purely mathematical empirical models. The accuracy of any model for predicting battery response to an input current and ambient conditions is determined by comparing the voltage response through simulations and experiments. It is essential to find a balance between the complexity of the physical information on the system and the execution time for the estimation/prediction of the battery behaviour. Generally, physics-based aging models are suitable for capturing physical phenomena, such as the growth of the SEI layer (Solid Electrolyte Interphase), active material isolation, particle cracking, gas generation, and lithium plating. Typically, physical models have high complexity and a very high computation time. Semi-empirical models focus on using severity factor-related models for

aging estimation, whilst not giving up on their physical meaning. Empirical models rely on concepts of regression and data-driven modelling to capture trends from experimental data from aging campaigns. A capacity/power fade over time due to a particular stress factor is identified and is generally supplemented by a theory to validate it. Common stress factors include current (C-rate), temperature, SoC, depth of discharge (DoD), and charge (Ah) throughout. The number and type of stress factors in any aging model vary based on the type of operating conditions and the accuracy of matching the experimental data. The development of empirical models does not mandate understanding the physical processes leading to aging.

The empirical aging model used in this work is based on the model reported in [60, 64], where several LMO-NMC cells have been aged at different temperatures, SoC, and currents, which highlight the aging effects classified as calendar and cycling aging. Calendar aging is a function of time and its effect increases at high temperatures and high SoC values. Cycling aging is directly related to the current level to which the battery is subjected, the number of charge/discharge cycles, and the temperature. Based on this model, the C_{SLB} battery pack capacity and R_{SLB} internal resistance can be estimated as:

$$C_{SLB}(t) = C_0 * \exp(-k_C * t) \quad (29)$$

$$R_{SLB}(t) = R_0 * \exp(+\gamma * k_R * t) \quad (30)$$

$$k_C = k_{C,cal} * k_{C,cyc} \quad (31)$$

$$k_R = k_{R,cal} * k_{R,cyc} \quad (32)$$

where C_0 = initial capacity; R_0 = initial resistance; γ = scale factor for the increase in resistance (function of SoC). k_{cal} and k_{cyc} represent the degradation rates due to the calendar and the cycling aging, defined as:

$$k_{cal}(t) = \frac{1}{\Delta SoC} \int_{SoC_1}^{SoC_2} \exp\left(\frac{c * SoC_i(t)}{a}\right) \exp\left(\frac{d}{a}\right) \exp\left(-\frac{b}{a * T_{SLB,i}(t)}\right) dSoC \quad (33)$$

$$k_{cyc}(t) = \exp\left(\frac{I_{SLB,i}(t)}{I_0} \exp\left(\frac{a_3}{a * T_{SLB,i}(t)} + b_3\right)\right) \quad (34)$$

where a is the gas constant, I_0 is equal to 1 A added for dimensional accuracy. The other values are described in Table 12 with reference to capacitance and

	Capacity fade model	Power fade model	Unit
a	8.314	8.314	$\left[\frac{J}{K \cdot mol} \right]$
b	67.6	57.82	$\left[\frac{kJ}{mol} \right]$
c	34.6	29.2	$\left[\frac{J}{K \cdot mol} \right]$
d	131.36	111.24	$\left[\frac{J}{mol} \right]$
a ₃	49.45	-	$\left[\frac{kJ}{mol} \right]$
b ₃	-24.06	-	-

Table 12: Aging model parameter for NMC-LMO battery pack.

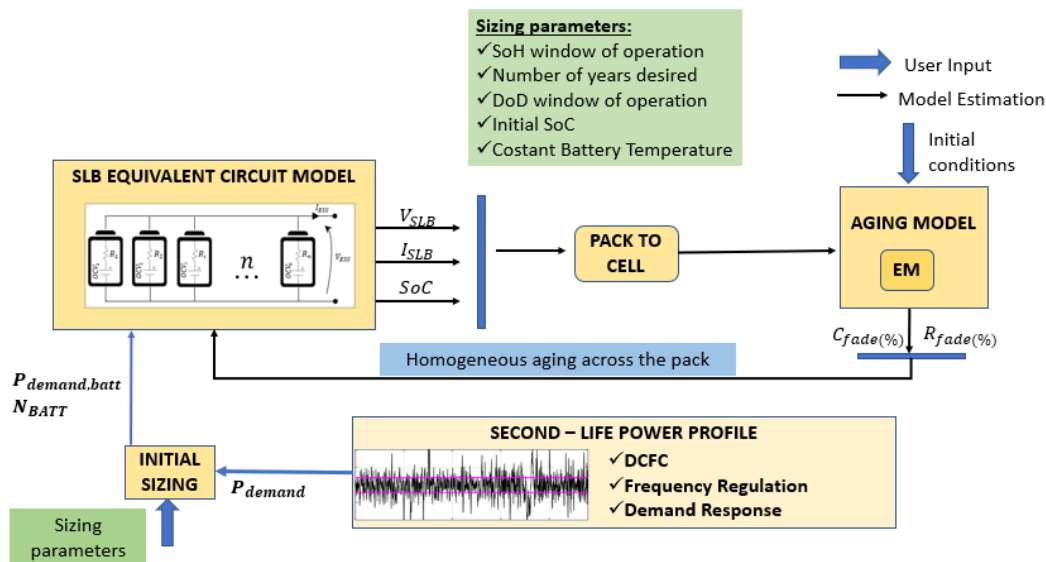


Figure 52: Schematic of the SLB-system.

resistance. Using these equations, a model has been developed using Matlab (Fig. 52) that simulated the SLB pack including the estimation of the capacity and power fade. The input of the model is the system parameters, the power profile, and the initial conditions (SoC₀, C₀, R₀). The tool can be utilized also to provide an initial energy-based sizing of the system that respects the specific mission profile, however, a more in-depth analysis needs to be performed to evaluate the lifetime expectation of the system. By setting the SoH values, the time, the initial SoC, and setting a constant temperature, it has been possible to trace the aging evolution for the various DCFC profiles. For example, Fig. 53 reports the evolution of capacity fade and power fade of the SLB when the profile of Fig. 50(a) is applied for 3 years. The increase of capacity fade after 3 years is 20%; while power fade increased by 52.3%.

Fig 54(bottom) shows the evolution of the daily SoC at the end of each day. Due to the capacity and power fade, the SoC trend decreases over time and

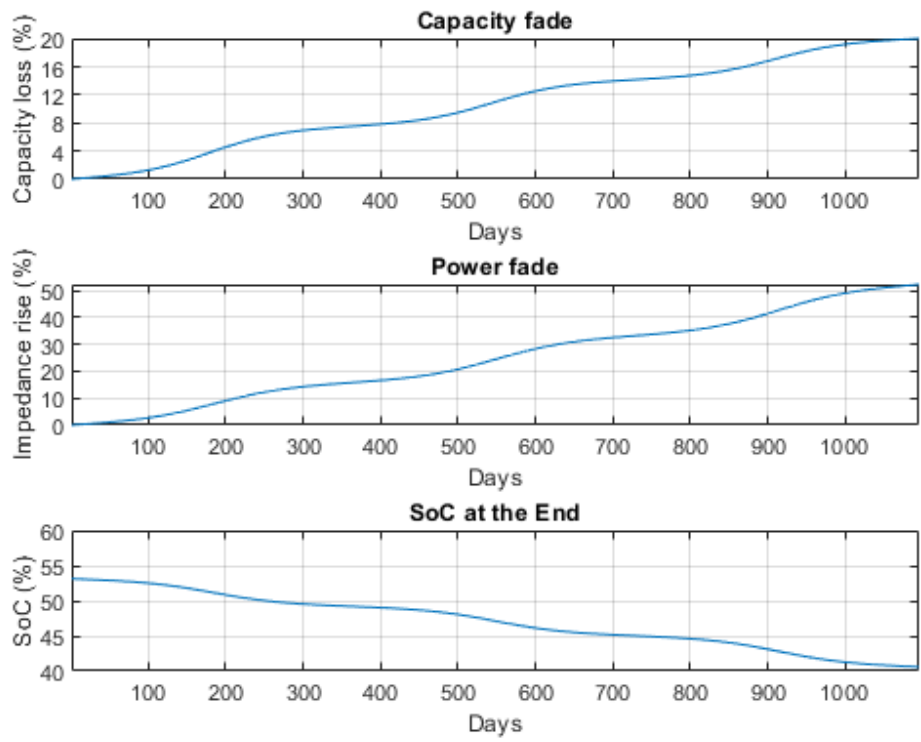


Figure 53: Simulation battery aging effect after 3 years for DCFC application: Top: Capacity fade; Center: Power fade; Bottom: SoC at the end of each day.

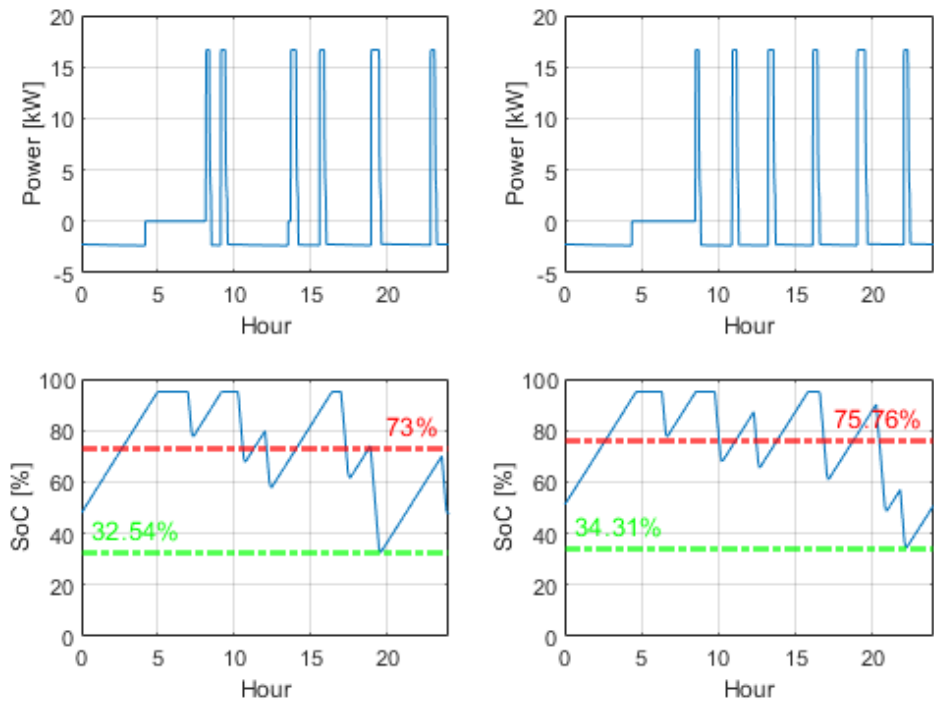


Figure 54: Comparison between two different DCFC power profiles with the relative SoC evolutions. The red trace is the SoC mean; the green trace is the minimum SoC value.

highlighting the reduced capability of the SLB in supplying energy during the day. This SoC drift has been calculated as the difference between the final SoC value of the first day with the final SoC value of the last day. For this profile, a SOC drift equal to 12% is noted. Then, if the SLB loses its ability to supply the required energy to EVs during the DCFC events, the battery pack will be automatically replaced.

4.3 Application and aging correlation

Using the Monte Carlo simulation methodology, 50 random profiles of the daily 50 kW DCFC power demand have been generated. Then the SLB power profile has been achieved considering $n=3$. Fig 54 shows an example of two different SLB power profiles and related SoC evolution. It is possible to notice that these profiles are characterized by different SoC mean and minimum values, while the maximum SoC is the same due to the specific control strategy.

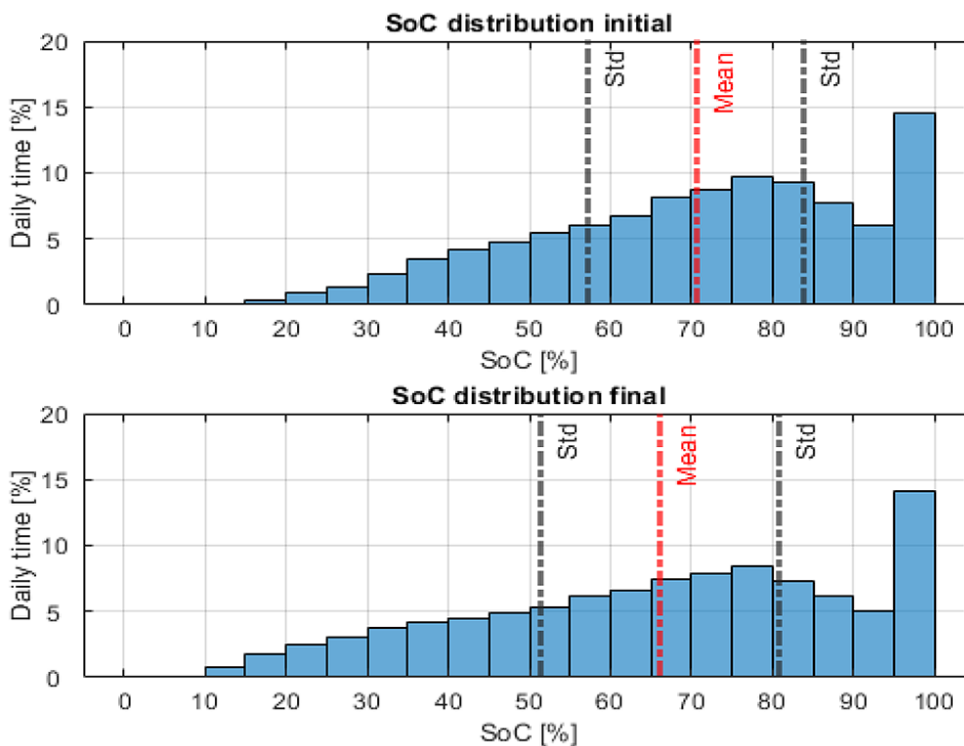


Figure 55: SoC distributions referred at first (top) and last (bottom) day of the time horizon of 3 years for the DCFC profile reported in Fig. 54(a).

Fig. 55 shows the probability distribution function of SoC considering the profile of Fig. 54(a), evaluated on the first (top) and on the last day of simulation (bottom). It is possible to note that the SLB pack is kept at high SoC during rest (SoC=95%) and that the percentage of time at this high SoC decreases at the end of the 3 years. The rest at high SoC is greatly accelerating calendar

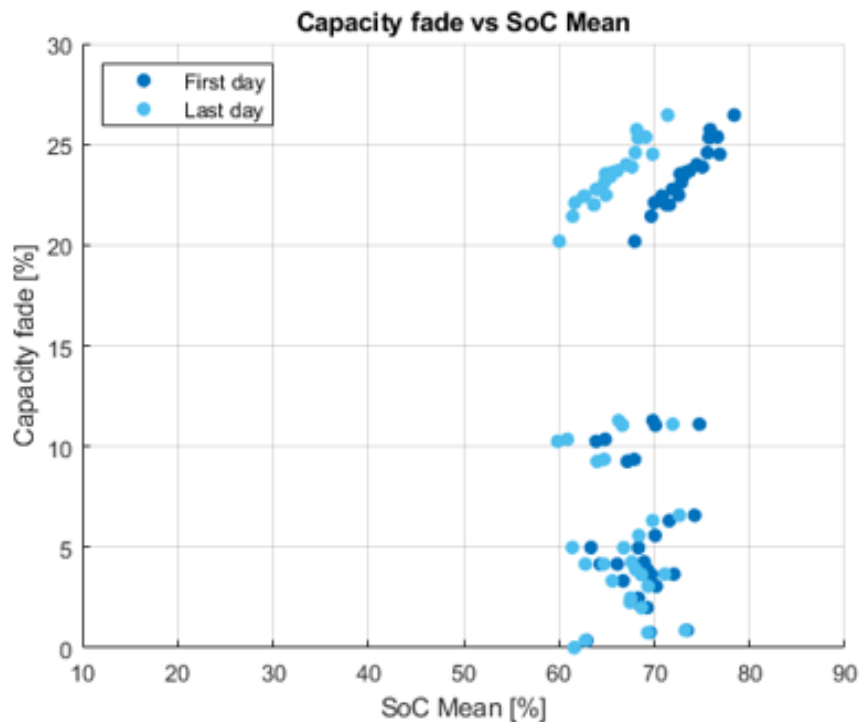


Figure 56: Capacity fade distribution as a function of the SoC means for each profile.

aging. Then, due to increased capacity fade the SLB pack will be subject to a higher depth of discharge, so the minimum SoC decreases over time as well. If the SLB pack reaches the minimum SoC a replacement will be likely activated, since the system will not be able to supply the power requested by the load. For this daily analysis mean and standard deviation are defined as shown in Fig. 55.

The following metrics have been then considered to statistically correlate the power profile behaviour (in particular of the SoC dynamics) with the aging phenomena (such as capacity fade, power fade, and SoC drift):

- SoC maximum
- SoC minimum
- Daily mean of SoC
- SoC standard deviation

These metrics have been applied to the 50 DCFC profiles. The simulation platform has been used to simulate the aging behaviors of the SLBs when the 50 developed profiles are considered. Note that the maximum SoC=95% for all the profiles, so no further analysis is performed on this metric. Fig. 56, 57, 58 show the statistical distribution of the capacity fade for each profile after the 3-year period in relation to the mean SoC, the minimum SoC, and the SoC standard deviation, respectively. Moreover, the dark and light blue points

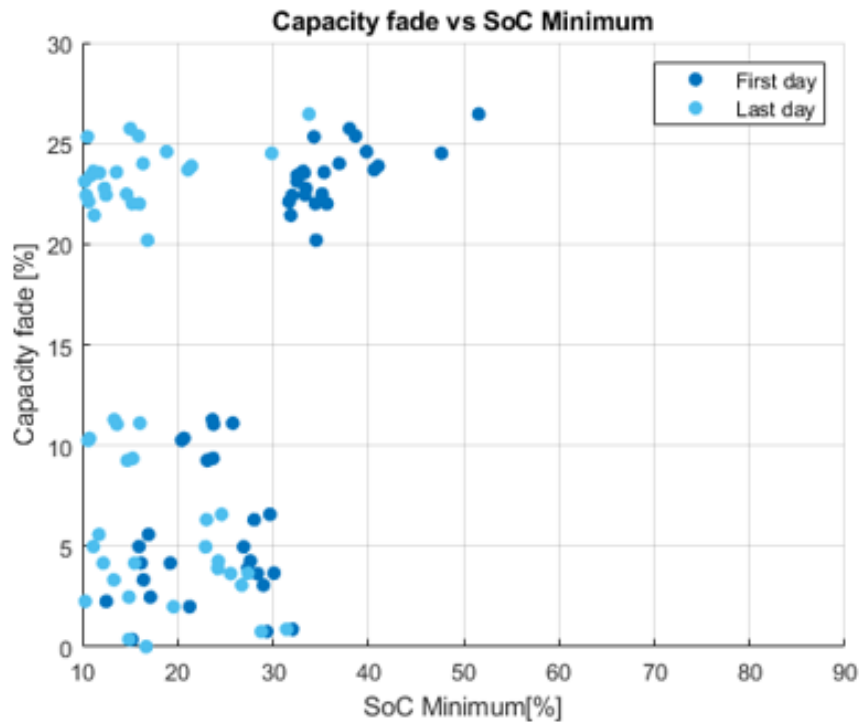


Figure 57: Capacity fade distribution as a function of the minimum value of SoC for each profile.

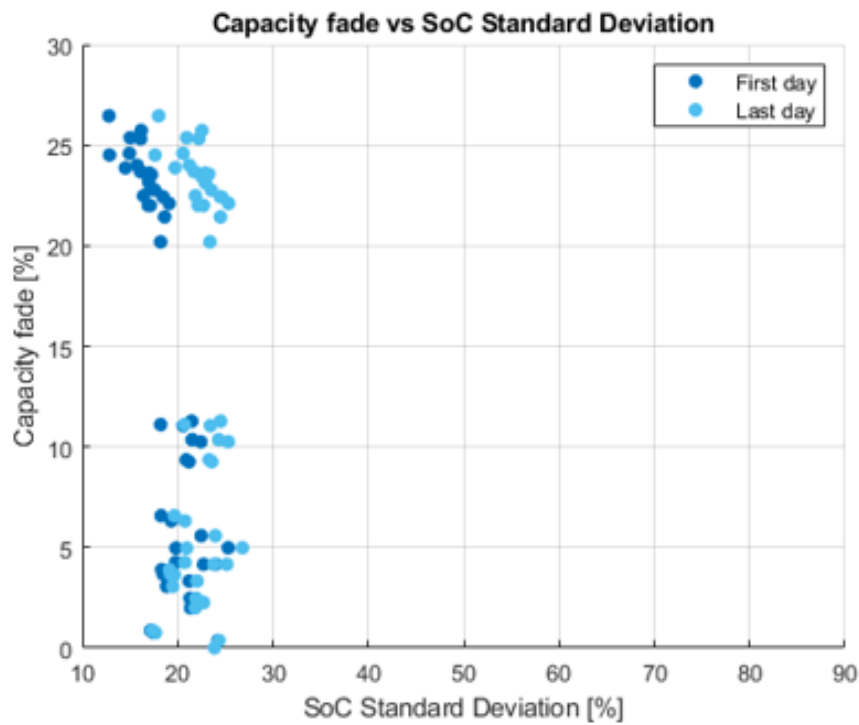


Figure 58: Capacity fade distribution as a function of the SoC standard deviation for each profile.

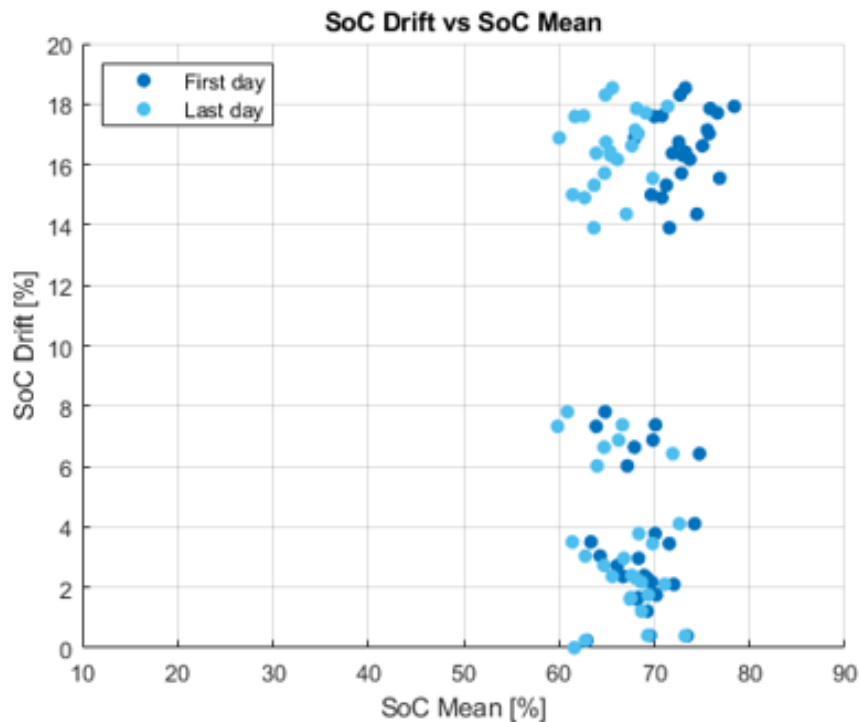


Figure 59: SoC drift distribution as a function of the SoC means for each profile.

identify the SoC at the start and the end of the period of analysis (e.g. first and last day of the simulation). It has been observed that the mean and minimum SoC values tend to decrease between the initial and final day of the analysis, while there is an increase in the value for the standard deviation due to the more variability of the SoC in a day caused by the aging effect.

Fig. 59, 60, 61 show the correlation between the SoC drift and the SoC mean, minimum and standard deviation. The SoC drift has been evaluated as the difference between the initial and final SoC value of day one (dark blue) and the last day of the simulation (light blue). A similar trend can be observed for the power fade.

Then the reported data of Fig. 57 can be categorized considering the replacement rate, as shown in Fig. 62 (first day) and Fig. 63 (last day) and it is possible to notice how the replacement rate is well correlated with the SoC minimum. In particular, in this application there are:

- Power profiles with no need for replacement: capacity fade will be 20-25% after 3 years - the SoC minimum at day 1 is about 40%;
- Power profiles with 1 SLB replacement: capacity fade will be 0-10% after 3 years (depending on when the replacement happened) - the SoC minimum at day 1 is 20-30%;
- Power profiles with 2 SLB replacements: capacity fade will be 0-5% after 3 years (depending on when the replacement happened) - the SoC minimum at day 1 is about 20%;

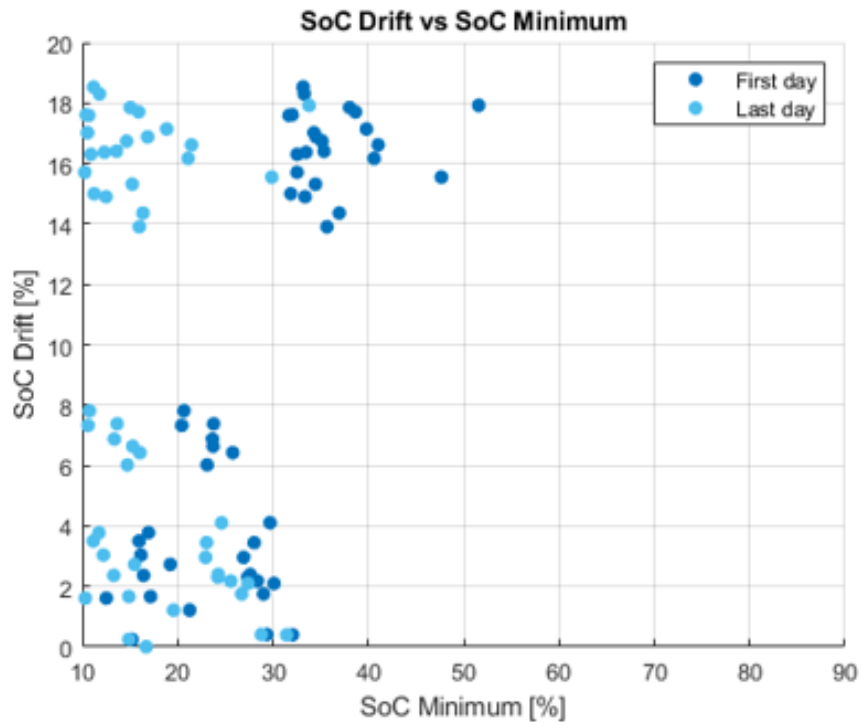


Figure 60: SoC drift distribution as a function of the minimum value of SoC for each profile.

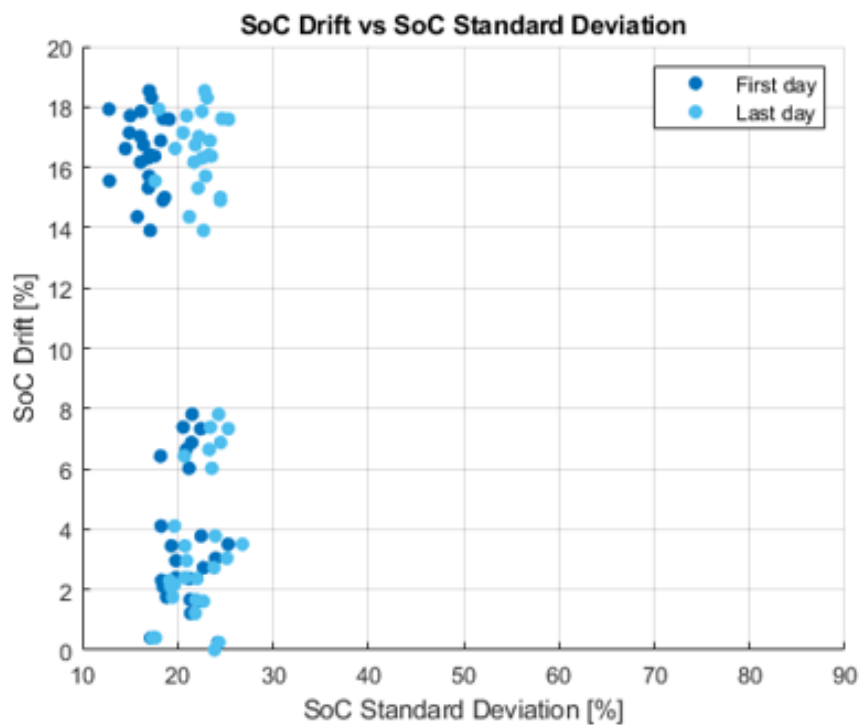


Figure 61: SoC drift distribution as a function of the standard deviation of SoC for each profile.

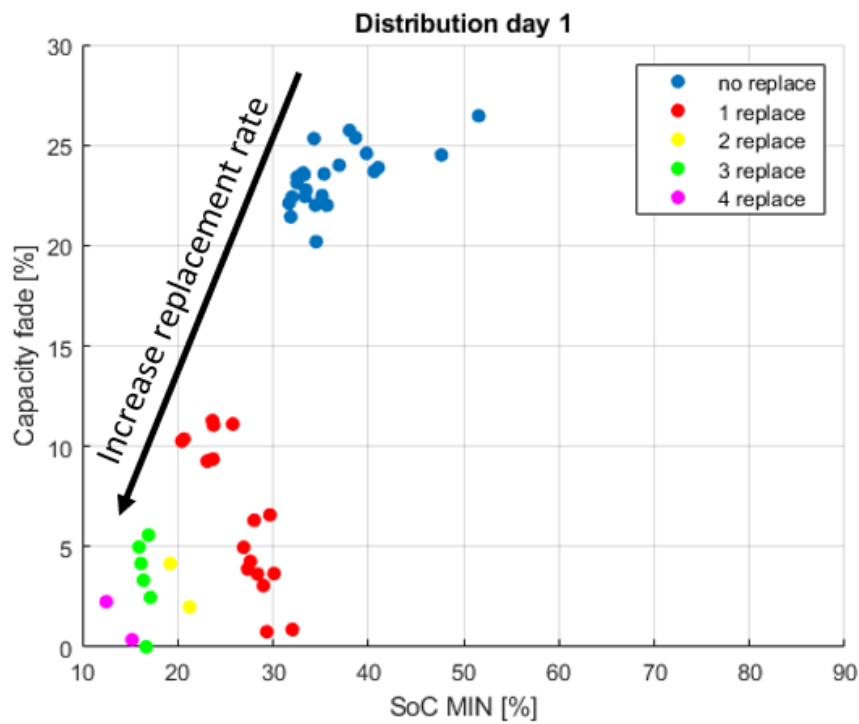


Figure 62: Capacity fade distribution considering the initial minimum value of SoC for each profile and related replacement.

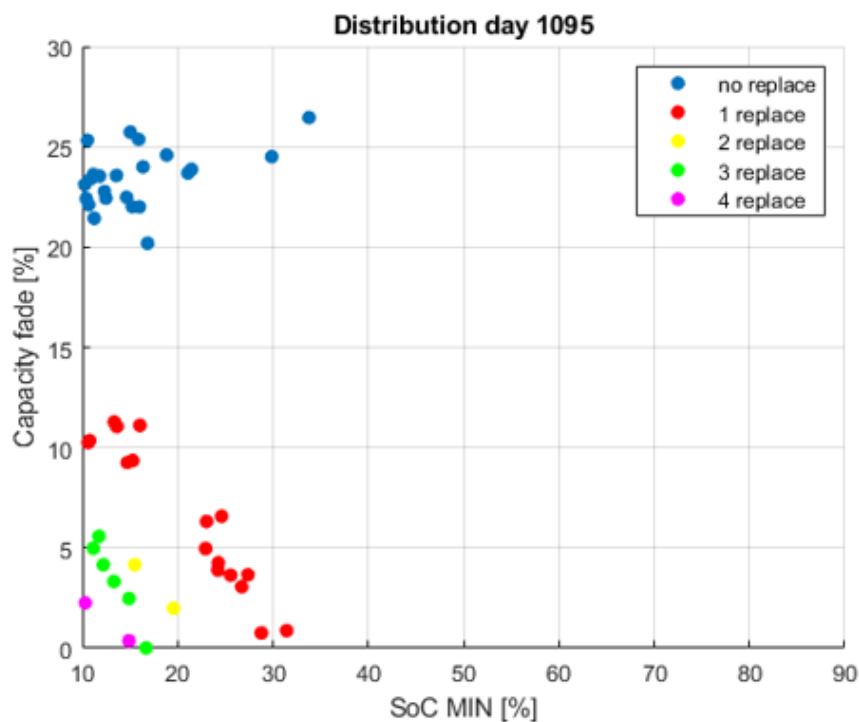


Figure 63: Capacity fade distribution considering the final minimum value of SoC for each profile and related replacement.

- Power profiles with 3 SLB replacements: capacity fade will be 0-5% after 3 years (depending on when the replacement happened) - the SoC minimum at day 1 is about 18%;
- Power profiles with 4 SLB replacements: capacity fade will be 0-2.5% after 3 years (depending on when the replacement happened) - the SoC minimum at day 1 is 12-13%.

It is important to point out that in general, the DCFC station will be applying a combination of these power profiles and not always the same one, as reported in this study. However, the main scope of this study is to identify the gravity of the different power profiles the probability of these profiles to affect the aging performance of the SLB. The results achieved with this analysis can be expanded to cases in which the power profiles are combined, or another cycling aging is present.

4.4 SMHB comparison

The implementation of SLB for applications such as DCFC turns out to be an important factor from an economic point of view, considering the ever-increasing diffusion of electric vehicles. However, other technologies can be used in this context. Due to their characteristics, the SMHB can form the battery packs that make up the electric charging stations. As seen in Chapter 2, the intrinsic characteristics of SMHBs allow for a rapid power response thanks to the doping of iron. For this reason, a comparison between lithium-ion SLBs and SMHBs for DCFC applications has been evaluated. This evaluation has been made considering the SMHBs both as an alternative to the SLBs and as a support to them, for the application of DCFC. Using the circuit model proposed (12), the response behaviour of a battery pack consisting of SMHB for a daily DCFC profile has been simulated.

Fig. 64 and 65 show the evolution of power and current for a single SMHB, respectively. The battery pack has been considered to consist of 4 SMHBs. It can be seen that the peak power required by the charge during a daily profile does not exceed 20 kW, while the current ones do not go beyond 30 A. The battery pack is recharged at a constant rate, equal to 5 A per module. With this information, it has been possible to verify that a commercial SMHB (Table 2) managed by a BMS that exploits the proposed circuit model (thus expanding its operating range) is perfectly suitable for DCFC application. Fig. 66 shows the relative evolution of the SoC. The operating range has been kept the same as that used for the SLBs, in order to make the comparison more consistent.

From an economic point of view, using SMHBs as charging stations can be inconvenient, as they cost more than lithium-ion batteries [72]. What drives interest in using SMHBs is the low degradation rate for stationary applications. As seen in the previous section, the factors that determine cell life, hence

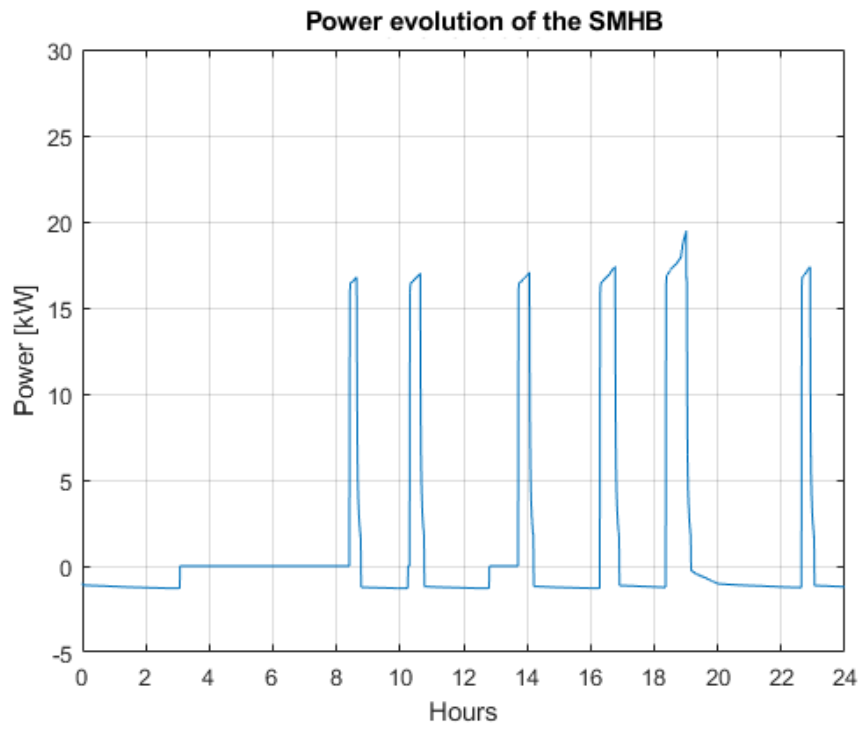


Figure 64: SMHB power evolution for the DCFC application.

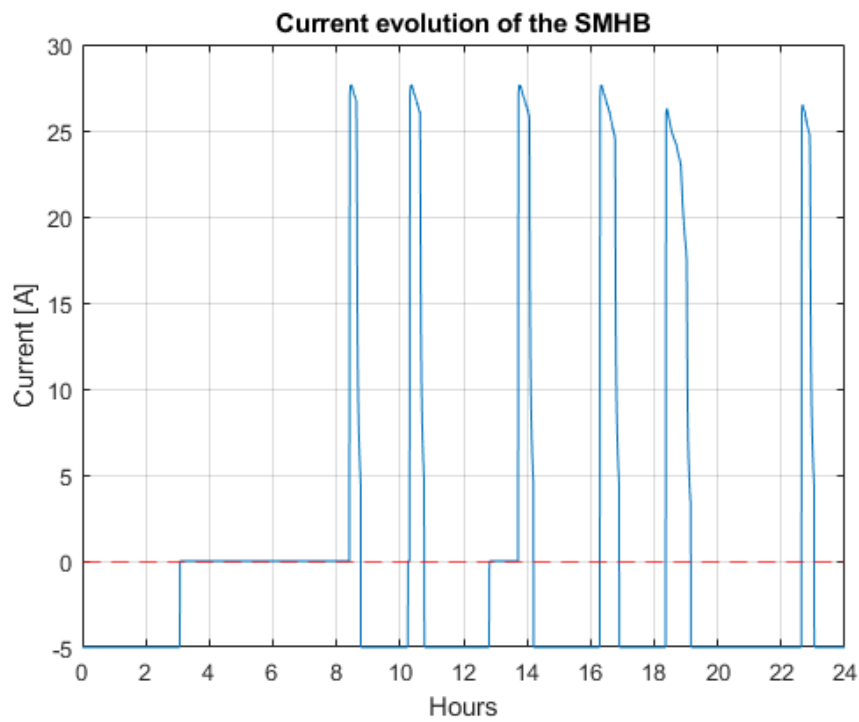


Figure 65: SMHB current evolution for the DCFC application.

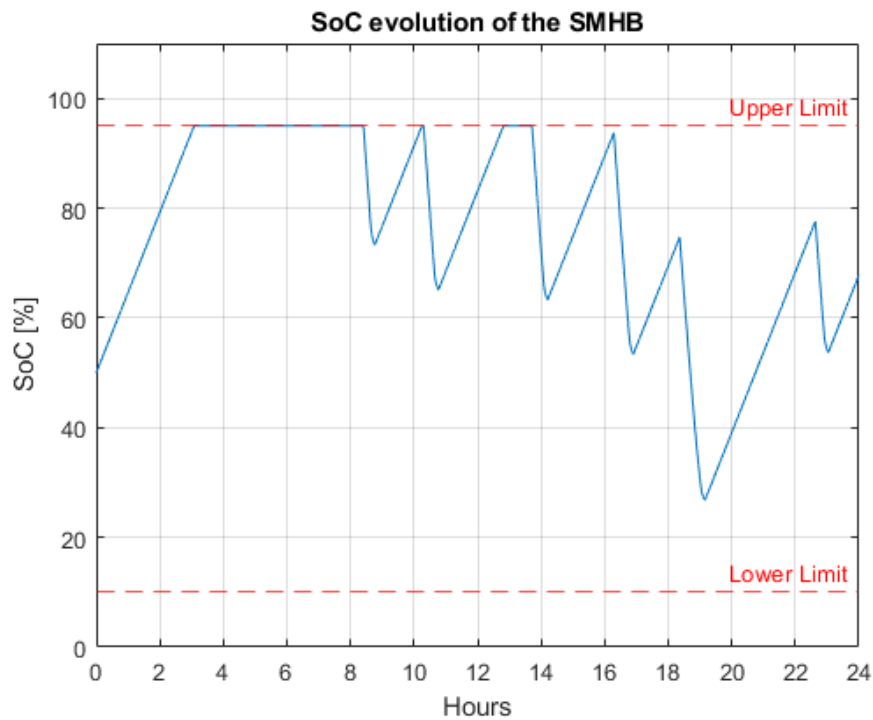


Figure 66: SoC evolution of the SMHB during a DCFC application.

battery life, are corrosion, increased resistance and loss of capacity. Several studies have been done on the degradation rate of SMHB.

In [73] it was shown that in the absence of cycles, the SMHB cell degrades very slowly. This fully charged battery has been kept in idle mode for at least 15 years and periodically cycled. The measured capacity remained unchanged and the results clearly indicate that there is no damage to the power capacity either. Regarding the electrical performance with aging, the results for the repeated deep cycle [35] and the EV continuous cycling [73] have been reported. In the deep cycle test, the battery is discharged at the rate $C/5$ up to the end of the discharge voltage or capacity (End of Discharge) criterion, whichever comes first. Charging starts immediately after discharge. The results show that the battery still consistently provides initial capacity after more than six hundred cycles. The only evident degradation is the decrease of the voltage at the end of the discharge due to the increase of the internal resistance. The EV profile cycling test simulating weekly vehicle use over a period of 7 years, has been carried out by performing a peak pulse power between 5% and 80% of the DoD (Deep of Discharge). The results show that after more than 5,000 cycles (in terms of equivalent nominal capacity), the capacity remained unchanged again, while the average energy availability of the cells decreased due to the increase in internal resistance.

From these results, it can be stated that the main effect of SMHB aging is the overall increase in the internal resistance of the cell. Studies of the chemical analysis of the performance of SMHB have shown that the increase in

internal resistance is due to the formation of a low conductive layer of NiCl_2 on the surfaces of the Ni particles. The active surface area of the Ni particles is crucial for the performance of the battery because the redox reaction can only occur on the surface of the electrically conducting Ni particles. Therefore, the formation of a thick and dense NiCl_2 layer often limits the charge. The main parameters leading to faster growth of Ni particles are high current density, high SoC at end of charge (EoC), and high Ni/NaCl ratio. The results imply that higher current density is a major parameter that induces Ni particle growth while the effect of higher EOC is minimal on Ni particle growth [74]. However, next studies have demonstrated that the operating temperature has a significant influence on the cell chemistries during the battery cycling [75]. Cell polarization, an important indicator of cell degradation, has been shown to increase faster at 280°C than at 175°C due to the faster growth of grains in the cathode. This turns out to be an advantage from the point of view of cell operation, as a lower temperature can potentially reduce costs associated with cell packaging and reduce heat loss. Against this background, the long-term cycle of an SMHB showed excellent stability over 1,000 cycles. No battery degradation was observed up to the 700th cycle and thereafter the degradation rate was 0.01% per cycle. The system has been found to be less energy efficient, but the benefits of using a lower operating temperature are greater.

Based on these studies, tests simulating the continuous charge and discharge of the SMHB have been performed, varying the value of the internal resistance. The simulation has been based on the long-term peak shaving test described in [76]. Here, each complete cycle consisted of four steps lasting a total of 24h. The steps included a charge phase in which maximum capacity (100% SoC) was reached, a discharge phase, and two rest phases. In this way, battery behaviour in the peak shaving application has been simulated. The results showed a capacity loss of 0.0046%/cycle over 150 cycles. However, the evolution of the SoC has shown how the storage system has always reached the maximum available capacity (200 Ah). The degradation element is attributable to the fact that continuous use leads to an increase in internal resistance with a consequent delay in dynamics.

To verify this concept, the following simulation has been developed: a discharge starting from 95% of the SoC up to 10% has been imposed; subsequently, a charge in order to bring the SoC back to the initial value has been imposed. The power was kept constant at 4 kW both in discharge and in charge. Using the SMHB model described in chapter 2, it was possible to derive the evolution of the SoC of the total cycle. Fig 67 shows the evolution of the SoC for the described cycle. The characteristic parameters of the equivalent circuit are those described in Table 5 and Table 4, for discharge and charge phase respectively. To simulate degradation of the SMHB, the internal resistance has been varied gradually. As the internal resistance increases, it has been noted that the required discharge time takes longer to reduce the SoC to 10%. Fig.

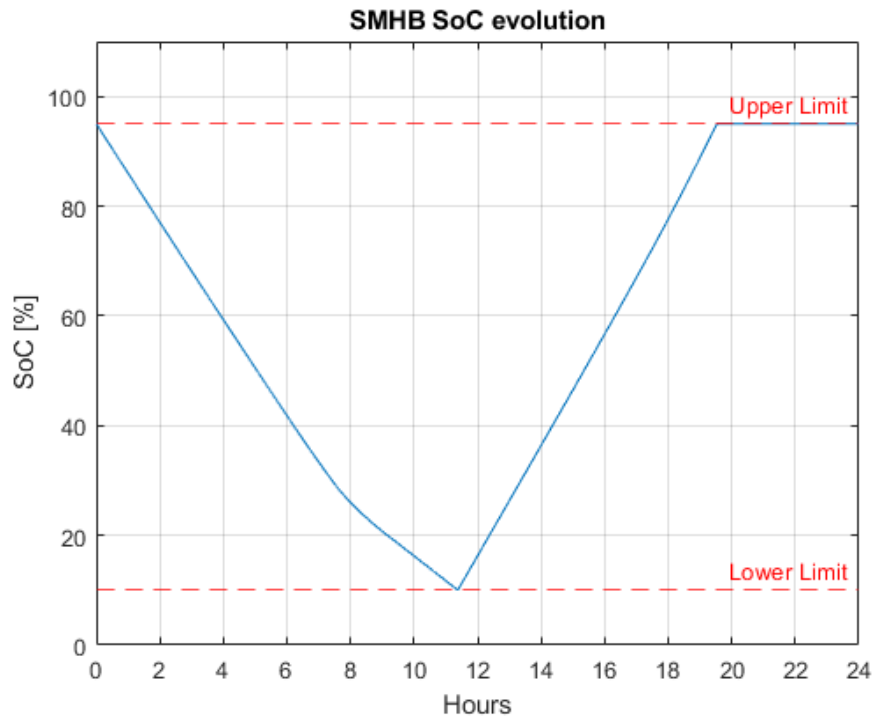


Figure 67: SoC evolution of the SMHB during a simulation peak shaving test.

68(a) shows the SoC trend for different internal resistance values. In particular, the comparison between the optimal internal resistance values and the relative increase of 20%, 40%, and 60% has been depicted. Fig. 68 (b) shows in detail the delay of the individual tests in relation to the increase in internal resistance. The element that is noticeable is the delay in dynamics. To describe the rate of degradation, the discharge capacity (Ah) for the 20%, 40%, and 60% increase of resistance has been measured. The difference between these values and the optimal condition revealed a reduction in the capacity of approximately 0.7 Ah for a 60% increase in internal resistance. For a correct description of the phenomenon, it is necessary to evaluate the rate of increase of the internal resistance in relation to the number of cycles to which the SMHB is subjected. In the absence of such data, it is still possible to consider SMHB as a good solution for stationary applications such as DCFC, to support SLBs.

The assessment of aging is still a matter of great interest for SMHB. Given the need to find a valid alternative to lithium-ion batteries (which will focus on vehicular applications), many studies are turning to this solution for the characteristics described in these works.

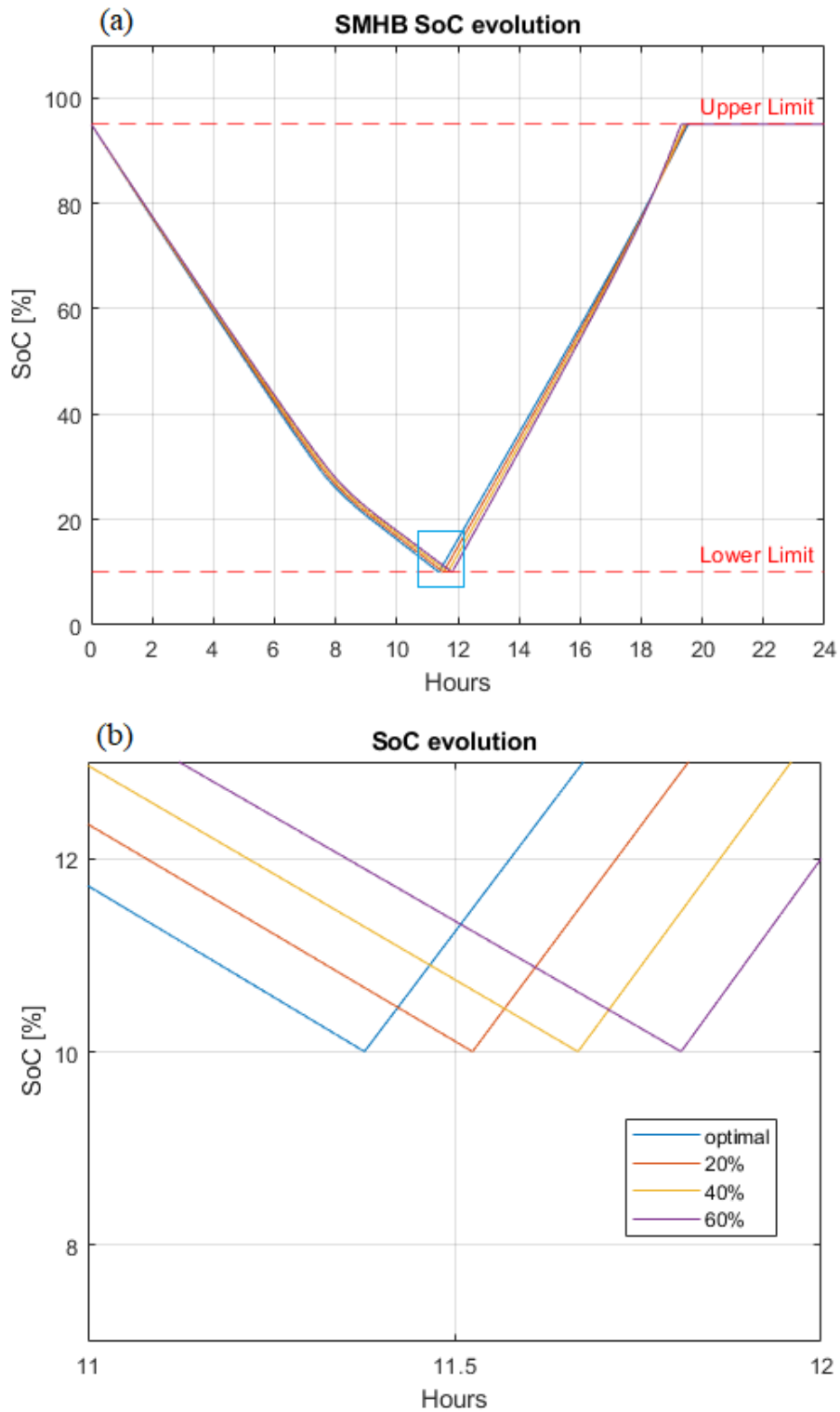


Figure 68: SoC evolutions of the SMHB (a) during a simulation peak shaving test. (b) detail at low SoCs.

Conclusion

This PhD dissertation has presented the dynamic modelling and implementation of a molten salt storage system, of the Sodium Metal Halide Battery (SMHB) type. In particular, in Chapter 1 the state-of-art of the various technologies of Electrochemical Energy Storage Systems (E-ESSs) has been presented. The various E-ESSs modelling techniques and the main fields of stationary application have been presented. In this context, the Sodium Metal Halide Battery (SMHB) is considered one of the most interesting E-ESSs to provide ancillary services in transmission and distribution systems. In Chapter 2, the analysis and dynamic modelling of SMHB have been presented. The proposed model has been the purpose of representing the dynamics of the system in the best possible way, considering all its critical issues at a low State of Charge (SoC). The modelling technique used is based on the second-order Thevenin equivalent circuit. The proposed model has been experimentally validated. By setting an impulse current in the discharge and charge phase of the battery, the parameters of the equivalent circuit have been identified, in the SoC range from 90% to 10%. The presence of iron has been found to be essential for the correct modelling of the system. The behaviour of the iron has been modelled through a voltage generator (first constant and subsequently variable). With these measures, the modelling error within the operating range of the SoC has been reduced to values close to 1%. In Chapter 3 the SMHB interface to a DC-link through an innovative DCDC converter has been presented. The converter topology examined has been of the Dual Active Bridge (DAB) type. Two configurations of the DAB converter have been presented: the standard configuration and the partial configuration. The latter configuration has been shown the advantage of being able to modulate a reduced voltage level (that of the battery, subject to variation). In this way, the dissipation losses and the dimensions of the converter are reduced. The modulation technique adopted has been the Single Phase Shift (SPS), whose phase shift angle has been determined through a control procedure based on empirical equations and on the implementation of a PI controller. The efficiencies of the two converters considering the Round Trip Efficiency of the battery-converter system have been presented. A 3% higher efficiency in the system that implements the partial configuration of the DAB has been verified. In Chapter 4, second-life lithium-ion batteries (SLBs) discarded from vehicular applications and their application in the DC fast charge (DCFC) has been presented. Through a zero-order circuit model and a heuristic aging model, the main aging effects

(loss in capacity and power) of lithium-ion SLBs for a given time horizon have been presented. Calendar aging has been the predominant aging mechanism in this application. Several metrics based on the evolution of the SoC have been defined and correlated to the SLBs' degradation and replacement rate. A high correlation has been shown between the replacement rate and the SLBs' daily minimum SoC. Finally, the comparison between SLBs and SMHBs for the application of DCFC has been presented. In particular, it has been evaluated how the aging phenomena for SMHBs cause a delay in the dynamics of the battery, due to the increase in internal resistance, without reducing the storage capacity. More analysis on the aging effects of SMHB will need to be done, but current research shows that more and more applications are exploiting its use.

Publications

- M. Boi, D. Battaglia, A. Salimbeni and A. Damiano, "A Non-Linear Electrical Model for Iron Doped Sodium Metal Halides Batteries," 2018 IEEE Energy Conversion Congress and Exposition (ECCE), 2018, pp. 2039-2046, doi: 10.1109/ECCE.2018.8557585
- M. Boi, D. Battaglia, A. Salimbeni and A. Damiano, "A Novel Electrical Model for Iron Doped-Sodium Metal Halide Batteries," in IEEE Transactions on Industry Applications, vol. 55, no. 6, pp. 6247-6255, Nov.-Dec. 2019, doi: 10.1109/TIA.2019.2938479
- M. Boi, D. Battaglia, A. Salimbeni and A. Damiano, "Energy Storage Systems Based on Sodium Metal Halides Batteries," 2019 IEEE Energy Conversion Congress and Exposition (ECCE), 2019, pp. 2452-2459, doi: 10.1109/ECCE.2019.8913257
- Battaglia, D., D'Arpino, M., Ganesh, S., and Carlson, J., "Impact of Power Profile on the Estimation of Second Life Batteries Remaining Useful Life," SAE Technical Paper 2021-01-0767, 2021, <https://doi.org/10.4271/2021-01-0767>

Bibliography

- [1] R.A. Huggins. *Energy storage: Fundamentals, materials and applications, second edition*. Jan. 2015, pp. 1–509. DOI: [10.1007/978-3-319-21239-5](https://doi.org/10.1007/978-3-319-21239-5).
- [2] Behnam Zakeri and Sanna Syri. “Electrical energy storage systems: A comparative life cycle cost analysis.” In: *Renewable and Sustainable Energy Reviews* 42 (Nov. 2014). DOI: [10.1016/j.rser.2014.10.011](https://doi.org/10.1016/j.rser.2014.10.011).
- [3] Changsong Chen et al. “Optimal Allocation and Economic Analysis of Energy Storage System in Microgrids.” In: *IEEE Transactions on Power Electronics* 26.10 (2011), pp. 2762–2773. DOI: [10.1109/TPEL.2011.2116808](https://doi.org/10.1109/TPEL.2011.2116808).
- [4] Antonio Scala et al. “Distributed Generation and Resilience in Power Grids.” In: vol. 7722. Aug. 2012. DOI: [10.1007/978-3-642-41485-5_7](https://doi.org/10.1007/978-3-642-41485-5_7).
- [5] Alfonso Damiano et al. “Electric Vehicle Energy Storage Management for Renewable Energy Sources Exploitation.” In: Mar. 2012, pp. 1–8. ISBN: 978-1-4673-1562-3. DOI: [10.1109/IEVC.2012.6183274](https://doi.org/10.1109/IEVC.2012.6183274).
- [6] Henok Behabtu et al. “A Review of Energy Storage Technologies’ Application Potentials in Renewable Energy Sources Grid Integration.” In: *Sustainability* 12 (Dec. 2020), p. 10511. DOI: [10.3390/su122410511](https://doi.org/10.3390/su122410511).
- [7] David Connolly. *A Review of Energy Storage Technologies: For the integration of fluctuating renewable energy*. 2010.
- [8] A.F.Zobaa. *Energy storage technologies and applications*. Croazia: InTechOpen, 2013.
- [9] T.B. Reddy D. Linden. *Linden’s Handbook of batteries*. 2011.
- [10] Steven Eckroad. “EPRI-DOE Handbook of Energy Storage for Transmission and Distribution Applications.” In: (Jan. 2003).
- [11] P.F. Ribeiro et al. “Energy storage systems for advanced power applications.” In: *Proceedings of the IEEE* 89.12 (2001), pp. 1744–1756. DOI: [10.1109/5.975900](https://doi.org/10.1109/5.975900).
- [12] Valentin A. Boicea. “Energy Storage Technologies: The Past and the Present.” In: *Proceedings of the IEEE* 102.11 (2014), pp. 1777–1794. DOI: [10.1109/JPROC.2014.2359545](https://doi.org/10.1109/JPROC.2014.2359545).
- [13] F. Alessandrini G. B. Appetecchi M. Conte. “Studio di fattibilità tecnica sull’applicabilità delle batterie al litio nelle reti elettriche.” In: *ENEA Report Rds* (2010).
- [14] Sergio Vazquez et al. “Energy Storage Systems for Transport and Grid Applications.” In: *IEEE Transactions on Industrial Electronics* 57.12 (2010), pp. 3881–3895. DOI: [10.1109/TIE.2010.2076414](https://doi.org/10.1109/TIE.2010.2076414).

- [15] Heide Budde-Meiwes et al. "A review of current automotive battery technology and future prospects." In: *Proceedings of the Institution of Mechanical Engineers, Part D: Journal of Automobile Engineering* 227 (May 2013), pp. 761–776. DOI: [10.1177/0954407013485567](https://doi.org/10.1177/0954407013485567).
- [16] S. Mohammad Mousavi G. and M. Nikdel. "Various battery models for various simulation studies and applications." In: *Renewable and Sustainable Energy Reviews* 32 (Apr. 2014), 477–485. DOI: [10.1016/j.rser.2014.01.048](https://doi.org/10.1016/j.rser.2014.01.048).
- [17] Marc Doyle, Thomas F. Fuller, and John Newman. "Modeling of Galvanostatic Charge and Discharge of the Lithium/Polymer/Insertion Cell." In: 140.6 (1993), pp. 1526–1533. DOI: [10.1149/1.2221597](https://doi.org/10.1149/1.2221597). URL: <https://doi.org/10.1149/1.2221597>.
- [18] John Newman. *Fortran programs for the simulation of electrochemical systems*. URL: <http://www.cchem.berkeley.edu/jsngrp/fortran.html>.
- [19] C. M. Shepherd. "Design of Primary and Secondary Cells." In: 112.7 (1965), p. 657. DOI: [10.1149/1.2423659](https://doi.org/10.1149/1.2423659). URL: <https://doi.org/10.1149/1.2423659>.
- [20] Aicha Degla et al. "Comparison study and parameter identification of three battery models for an off-grid photovoltaic system." In: *International Journal of Green Energy* 16 (Jan. 2019). DOI: [10.1080/15435075.2019.1566134](https://doi.org/10.1080/15435075.2019.1566134).
- [21] Hian Chan and Darmawan Sutanto. "A new battery model for use with battery energy storage systems and electric vehicles power systems." In: vol. 1. Feb. 2000, 470–475 vol.1. ISBN: 0-7803-5935-6. DOI: [10.1109/PESW.2000.850009](https://doi.org/10.1109/PESW.2000.850009).
- [22] S. Buller et al. "Impedance-Based Simulation Models of Supercapacitors and Li-Ion Batteries for Power Electronic Applications." In: *Industry Applications, IEEE Transactions on* 41 (June 2005), pp. 742–747. DOI: [10.1109/TIA.2005.847280](https://doi.org/10.1109/TIA.2005.847280).
- [23] Paul Denholm et al. "The Role of Energy Storage with Renewable Electricity Generation." In: (Jan. 2010). DOI: [10.2172/972169](https://doi.org/10.2172/972169).
- [24] A. De Los Ríos et al. "Economic analysis of vehicle-to-grid (V2G)-enabled fleets participating in the regulation service market." In: *2012 IEEE PES Innovative Smart Grid Technologies (ISGT)*. 2012, pp. 1–8. DOI: [10.1109/ISGT.2012.6175658](https://doi.org/10.1109/ISGT.2012.6175658).
- [25] J. Eyer and G. Corey. "Energy storage for the electricity grid: Benefits and market potential assessment guide." In: (Jan. 2011), pp. 1–232.
- [26] Guido Carpinelli et al. "Load Leveling with Electrical Storage Systems: a Two-Step Optimization Procedure." In: *International Review of Electrical Engineering-iree* 8 (2013), pp. 729–736.

- [27] A. Even, J. Neyens, and A. Demousselle. "Peak shaving with batteries." In: *12th International Conference on Electricity Distribution, 1993. CIRED*. Vol. 5. 1993, 5.17/1–5.17/6 vol.5.
- [28] Salman Habib et al. "A Comprehensive Study of Implemented International Standards, Technical Challenges, Impacts and Prospects for Electric Vehicles." In: *IEEE Access* 6 (2018), pp. 13866–13890. DOI: [10.1109/ACCESS.2018.2812303](https://doi.org/10.1109/ACCESS.2018.2812303).
- [29] Egoitz Martinez-Laserna et al. "Technical Viability of Battery Second Life: A Study From the Ageing Perspective." In: *IEEE Transactions on Industry Applications* 54.3 (2018), pp. 2703–2713. DOI: [10.1109/TIA.2018.2801262](https://doi.org/10.1109/TIA.2018.2801262).
- [30] Kandler A. Smith et al. "Comparison of Plug-In Hybrid Electric Vehicle Battery Life Across Geographies and Drive Cycles." In: 2012.
- [31] Umberto Abronzini et al. "Cost Minimization Energy Control Including Battery Aging for Multi-Source EV Charging Station." In: *Electronics* 8 (2019). DOI: [10.3390/electronics8010031](https://doi.org/10.3390/electronics8010031).
- [32] R. Benato et al. "Sodium nickel chloride battery technology for large-scale stationary storage in the high voltage network." In: *Journal of Power Sources* 293 (Oct. 2015). DOI: [10.1016/j.jpowsour.2015.05.037](https://doi.org/10.1016/j.jpowsour.2015.05.037).
- [33] J.L Sudworth. "The sodium/nickel chloride (ZEBRA) battery." In: *Journal of Power Sources* 100 (Nov. 2001), pp. 149–163. DOI: [10.1016/S0378-7753\(01\)00891-6](https://doi.org/10.1016/S0378-7753(01)00891-6).
- [34] Cord-H Dustmann. "Advances in ZEBRA batteries." In: *Journal of Power Sources - J POWER SOURCES* 127 (Mar. 2004), pp. 85–92. DOI: [10.1016/j.jpowsour.2003.09.039](https://doi.org/10.1016/j.jpowsour.2003.09.039).
- [35] Silvio Restello, Giuseppe Lodi, and Emiliano Paolin. "Sodium-Nickel batteries for telecom applications: Design, performance and field operational overview." In: (Oct. 2011), pp. 1–6. DOI: [10.1109/INTLEC.2011.6099784](https://doi.org/10.1109/INTLEC.2011.6099784).
- [36] Jianwei Li et al. "A new parameter estimation algorithm for an electrical analogue battery model." In: *Conference Proceedings - IEEE Applied Power Electronics Conference and Exposition - APEC* (Feb. 2012). DOI: [10.1109/APEC.2012.6165855](https://doi.org/10.1109/APEC.2012.6165855).
- [37] Martin Coleman, William Hurley, and Chin Lee. "An Improved Battery Characterization Method Using a Two-Pulse Load Test." In: *Energy Conversion, IEEE Transactions on* 23 (July 2008), pp. 708–713. DOI: [10.1109/TEC.2007.914329](https://doi.org/10.1109/TEC.2007.914329).
- [38] T.M. O'Sullivan, Chris Bingham, and R.E. Clark. "Zebra battery technologies for all electric smart car." In: vol. 2006. June 2006, p. 243. DOI: [10.1109/SPEEDAM.2006.1649778](https://doi.org/10.1109/SPEEDAM.2006.1649778).

- [39] Sebastian Dambone Sessa et al. "Sodium nickel chloride battery steady-state regime model for stationary electrical energy storage." In: *Journal of Energy Storage* 6 (May 2016), pp. 105–115. DOI: [10.1016/j.est.2016.03.005](https://doi.org/10.1016/j.est.2016.03.005).
- [40] Maura Musio and Alfonso Damiano. "A non-linear dynamic electrical model of Sodium-Nickel Chloride Batteries." In: *2015 International Conference on Renewable Energy Research and Applications (ICRERA)*. 2015, pp. 872–878. DOI: [10.1109/ICRERA.2015.7418535](https://doi.org/10.1109/ICRERA.2015.7418535).
- [41] Mauro Boi, Andrea Salimbeni, and Alfonso Damiano. "A Thévenin circuit modelling approach for sodium metal halides batteries." In: *IECON 2017 - 43rd Annual Conference of the IEEE Industrial Electronics Society*. 2017, pp. 7611–7616. DOI: [10.1109/IECON.2017.8217334](https://doi.org/10.1109/IECON.2017.8217334).
- [42] Roy C Galloway and Steven Haslam. "The ZEBRA electric vehicle battery: power and energy improvements." In: *Journal of Power Sources* 80.1 (1999), pp. 164–170. ISSN: 0378-7753. DOI: [https://doi.org/10.1016/S0378-7753\(98\)00259-6](https://doi.org/10.1016/S0378-7753(98)00259-6). URL: <https://www.sciencedirect.com/science/article/pii/S0378775398002596>.
- [43] Alfonso Damiano, Claudia Musio, and Ignazio Marongiu. "Experimental validation of a dynamic energy model of a battery electric vehicle." In: *2015 International Conference on Renewable Energy Research and Applications (ICRERA)*. 2015, pp. 803–808. DOI: [10.1109/ICRERA.2015.7418523](https://doi.org/10.1109/ICRERA.2015.7418523).
- [44] Yu Fang et al. "Study on bidirectional-charger for electric vehicle applied to power dispatching in smart grid." In: *2016 IEEE 8th International Power Electronics and Motion Control Conference (IPEMC-ECCE Asia)*. 2016, pp. 2709–2713. DOI: [10.1109/IPEMC.2016.7512726](https://doi.org/10.1109/IPEMC.2016.7512726).
- [45] Michael Evzelman et al. "Active Balancing System for Electric Vehicles With Incorporated Low-Voltage Bus." In: *IEEE Transactions on Power Electronics* 31.11 (2016), pp. 7887–7895. DOI: [10.1109/TPEL.2015.2513432](https://doi.org/10.1109/TPEL.2015.2513432).
- [46] Lingxiao Xue et al. "Dual Active Bridge-Based Battery Charger for Plug-in Hybrid Electric Vehicle With Charging Current Containing Low Frequency Ripple." In: *IEEE Transactions on Power Electronics* 30.12 (2015), pp. 7299–7307. DOI: [10.1109/TPEL.2015.2413815](https://doi.org/10.1109/TPEL.2015.2413815).
- [47] Amr Amin et al. "A transformerless dual active half-bridge DC-DC converter for point-of-load power supplies." In: *2015 IEEE Energy Conversion Congress and Exposition (ECCE)*. 2015, pp. 133–140. DOI: [10.1109/ECCE.2015.7309680](https://doi.org/10.1109/ECCE.2015.7309680).
- [48] Shigenori Inoue and Hirofumi Akagi. "A Bi-Directional DC/DC Converter for an Energy Storage System." In: *APEC 07 - Twenty-Second Annual IEEE Applied Power Electronics Conference and Exposition*. 2007, pp. 761–767. DOI: [10.1109/APEX.2007.357601](https://doi.org/10.1109/APEX.2007.357601).

- [49] Chris Mi et al. "Operation, design and control of dual H-bridge-based isolated bidirectional DC-DC converter." In: *Power Electronics, IET* 1 (Jan. 2009), pp. 507–517. DOI: [10.1049/iet-pel:20080004](https://doi.org/10.1049/iet-pel:20080004).
- [50] Jun Huang et al. "Unified Triple-Phase-Shift Control to Minimize Current Stress and Achieve Full Soft-Switching of Isolated Bidirectional DC–DC Converter." In: *IEEE Transactions on Industrial Electronics* 63.7 (2016), pp. 4169–4179. DOI: [10.1109/TIE.2016.2543182](https://doi.org/10.1109/TIE.2016.2543182).
- [51] M.N. Kheraluwala et al. "Performance characterization of a high-power dual active bridge DC-to-DC converter." In: *IEEE Transactions on Industry Applications* 28.6 (1992), pp. 1294–1301. DOI: [10.1109/28.175280](https://doi.org/10.1109/28.175280).
- [52] Germán G. Oggier and Martin Ordonez. "High-Efficiency DAB Converter Using Switching Sequences and Burst Mode." In: *IEEE Transactions on Power Electronics* 31.3 (2016), pp. 2069–2082. DOI: [10.1109/TPEL.2015.2440753](https://doi.org/10.1109/TPEL.2015.2440753).
- [53] Georgios E. Sfakianakis et al. "Comparative Evaluation of Bidirectional Dual Active Bridge DC-DC Converter Variants." In: *2016 IEEE Vehicle Power and Propulsion Conference (VPPC)*. 2016, pp. 1–6. DOI: [10.1109/VPPC.2016.7791631](https://doi.org/10.1109/VPPC.2016.7791631).
- [54] Mohammad Faisal et al. "Review of Energy Storage System Technologies in Microgrid Applications: Issues and Challenges." In: *IEEE Access* PP (May 2018), pp. 1–1. DOI: [10.1109/ACCESS.2018.2841407](https://doi.org/10.1109/ACCESS.2018.2841407).
- [55] Björn Nykvist and Måns Nilsson. "Rapidly falling costs of battery packs for electric vehicles." In: *Nature Climate Change* 5 (Mar. 2015), pp. 329–332. DOI: [10.1038/nclimate2564](https://doi.org/10.1038/nclimate2564).
- [56] Eklas Hossain et al. "A Comprehensive Review on Second-Life Batteries: Current State, Manufacturing Considerations, Applications, Impacts, Barriers and Potential Solutions, Business Strategies, and Policies." In: *IEEE Access* 7 (2019), pp. 73215–73252. DOI: [10.1109/ACCESS.2019.2917859](https://doi.org/10.1109/ACCESS.2019.2917859).
- [57] Eddy Coron et al. "Impact of Lithium-Ion Cell Condition on Its Second Life Viability." In: *Journal of the Electrochemical Society* 167 (July 2020). DOI: [10.1149/1945-7111/aba703](https://doi.org/10.1149/1945-7111/aba703).
- [58] Jeremy Neubauer and Ahmad Pesaran. "The ability of battery second use strategies to impact plug-in electric vehicle prices and serve utility energy storage applications." In: *Lancet* 196 (Dec. 2011), pp. 10351–10358. DOI: [10.1016/j.jpowsour.2011.06.053](https://doi.org/10.1016/j.jpowsour.2011.06.053).
- [59] U. Abronzini et al. "Optimal energy control for smart charging infrastructures with ESS and REG." In: *2016 International Conference on Electrical Systems for Aircraft, Railway, Ship Propulsion and Road Vehicles International Transportation Electrification Conference (ESARS-ITEC)*. 2016, pp. 1–6. DOI: [10.1109/ESARS-ITEC.2016.7841427](https://doi.org/10.1109/ESARS-ITEC.2016.7841427).

- [60] Matilde D'Arpino and Massimo Cancian. "Lifetime Optimization for a Grid-Friendly DC Fast Charge Station With Second Life Batteries." In: *ASME Letters in Dynamic Systems and Control* 1 (Mar. 2020), pp. 1–6. DOI: [10.1115/1.4046579](https://doi.org/10.1115/1.4046579).
- [61] *Ford Focus EV*. Sept. 2018. URL: <https://avt.inl.gov/vehicle-button/2013-ford-focus>.
- [62] A. Genovese et al. "Realizzazione e sperimentazione di una stazione di ricarica rapida in CC nel CR Casaccia." In: *ENEA Report Rds* (2013).
- [63] G. Celli et al. "Aggregated electric vehicles load profiles with fast charging stations." In: *2014 Power Systems Computation Conference*. 2014, pp. 1–7. DOI: [10.1109/PSCC.2014.7038402](https://doi.org/10.1109/PSCC.2014.7038402).
- [64] Matilde D'Arpino and Massimo Cancian. "Design of a Grid-Friendly DC Fast Charge Station with Second Life Batteries." In: *SAE Technical Paper Series* (2019).
- [65] PJM. *Ancillary Services*. Mar. 2019. URL: www.pjm.com/markets-and-operations/ancillary-services.aspx,.
- [66] David Rosewater and Summer Ferreira. "Development of a frequency regulation duty-cycle for standardized energy storage performance testing." In: *Journal of Energy Storage* 7 (May 2016). DOI: [10.1016/j.est.2016.04.004](https://doi.org/10.1016/j.est.2016.04.004).
- [67] Raymond H. Byrne, Ricky J. Concepcion, and César A. Silva-Monroy. "Estimating potential revenue from electrical energy storage in PJM." In: *2016 IEEE Power and Energy Society General Meeting (PESGM)*. 2016, pp. 1–5. DOI: [10.1109/PESGM.2016.7741915](https://doi.org/10.1109/PESGM.2016.7741915).
- [68] Nicholas Dembski, Yann G. Guezennec, and Ahmed Soliman. "Analysis and Experimental Refinement of Real-World Driving Cycles." In: 2002.
- [69] Yaping Cai et al. "A generalized equivalent circuit model for large-scale battery packs with cell-to-cell variation." In: *2019 IEEE National Aerospace and Electronics Conference (NAECON)*. 2019, pp. 24–30. DOI: [10.1109/NAECON46414.2019.9057803](https://doi.org/10.1109/NAECON46414.2019.9057803).
- [70] Daniel Freudiger, Matilde D'Arpino, and Marcello Canova. "A Generalized Equivalent Circuit Model for Design Exploration of Li-Ion Battery Packs Using Data Analytics." In: *IFAC-PapersOnLine* 52 (Jan. 2019), pp. 568–573. DOI: [10.1016/j.ifacol.2019.09.090](https://doi.org/10.1016/j.ifacol.2019.09.090).
- [71] I. Baghdadi et al. "Lithium Battery Aging Model Based on Chemical Rate Approach." In: *2016 IEEE Vehicle Power and Propulsion Conference (VPPC)*. 2016, pp. 1–6. DOI: [10.1109/VPPC.2016.7791720](https://doi.org/10.1109/VPPC.2016.7791720).
- [72] Kendall Mongird et al. "Energy Storage Technology and Cost Characterization Report." In: (). DOI: [10.2172/1573487](https://doi.org/10.2172/1573487). URL: <https://www.osti.gov/biblio/1573487>.

- [73] J.L. Sudworth and R.C. Galloway. "SECONDARY BATTERIES – HIGH TEMPERATURE SYSTEMS | Sodium–Nickel Chloride." In: Jan. 2009, pp. 312–323. ISBN: 9780444527455. DOI: [10.1016/B978-044452745-5.00180-5](https://doi.org/10.1016/B978-044452745-5.00180-5).
- [74] Guosheng Li et al. "Cell degradation of a Na–NiCl₂ (ZEBRA) battery." In: *J. Mater. Chem. A* 1 (Nov. 2013). DOI: [10.1039/C3TA13644B](https://doi.org/10.1039/C3TA13644B).
- [75] Guosheng Li et al. "Advanced intermediate temperature sodium–nickel chloride batteries with ultra-high energy density." In: *Nature Communications* 7 (Feb. 2016), p. 10683. DOI: [10.1038/ncomms10683](https://doi.org/10.1038/ncomms10683).
- [76] Nimat Shamim et al. "Evaluating ZEBRA Battery Module under the Peak-Shaving Duty Cycles." In: *Materials* 14 (Apr. 2021), p. 2280. DOI: [10.3390/ma14092280](https://doi.org/10.3390/ma14092280).